Final Technical Report
GTRI Project No. 3244

TECHNOLOGY FOR SATELLITE POWER CONVERSION

Prepared by

M.A. Gouker
D.P. Campbell
J.J. Gallagher

Prepared for

NATIONAL AERONAUTICS AND SPACE ADMINISTRATION
Lewis Research Center
21000 Brookpark Road
Cleveland, Ohio 44135

NASA Technical Officer: W.M. Krawczonek

Under

June 30, 1987

GEORGIA INSTITUTE OF TECHNOLOGY
A Unit of the University System of Georgia
Atlanta, Georgia 30332

GTRI
GEORGIA TECH RESEARCH INSTITUTE

1987

Final Technical Report
on
Technology for Satellite Power Conversion

NASA Research Grant No. NAG3-282
Georgia Tech Research Institute
Project No. A-3244

NASA Technical Officer: W. M. Krawczonek

Prepared for
National Aeronautics and Space Administration
Lewis Research Center
21000 Brookpark Road
Cleveland, Ohio 44135

Prepared by
M. A. Gouker
D. P. Campbell
J. J. Gallagher

Georgia Tech Research Institute
Georgia Institute of Technology
Atlanta, Georgia 30332

June 30, 1987

TABLE OF CONTENTS

LIST OF FIGURES

LIST OF FIGURES (Continued)

LIST OF TABLES

1. INTRODUCTION

High frequency rectennas for capturing the earth's radiant energy or for narrow beam, point-to-point energy transfer are potentially important power sources for small airborne vehicles and space craft. This technology is an extension of the rectenna concepts developed for the Satellite Solar Power Station (SSPS) energy beaming system.[1-3] In the SSPS work, energy transfer at 2.45 GHz was demonstrated to be as high as 88% efficient.[4] These early low frequency rectennas consisted of rectifying circuits with discrete Schottky barrier diodes connected to the terminals of half-wave dipole antennas.

Several problems are encountered when the rectenna is scaled for higher frequency operation. The size of the half-wave resonant dipole decreases, necessitating thin film integrated circuit fabrication techniques. This means that the antenna will be on a substrate that is a significant portion of a wavelength at millimeter wave frequencies and many wavelengths thick in the mid-infrared. The directivity and efficiency of such substrate mounted antennas is not fully understood.

Presently, the semiconductor Schottky barrier diodes used in the low frequency rectennas will not operate above several hundred gigahertz. For rectenna devices to operate in the infrared region, metal-insulator-metal (quantum tunneling) diodes will have to be used. The barrier region is typically an oxide layer formed on one of the metal surfaces. The oxide layer must be extremely thin, less than 100 Å, in order for the quantum tunneling to occur. This thin layer, however, makes the metal-oxide-metal (MOM) diode extremely vulnerable to static discharge. In all, there are many problems to overcome before the high frequency rectenna is a reliable power transfer device.

We report, here, on our efforts to address these problems. At the outset of the program, the approach was to construct rectennas first for 1 millimeter wavelength operation, and then we intended to scale these results for device operation in the infrared region. The target was 10 μm wavelengths: this is the

region where the spectrum of the earth's radiant energy peaks.

More effort than expected was spent in studying the antennas at millimeter wave frequencies. The original antenna design had to be modified in order to measure the radiation pattern of the dipole antenna. The small size of the antenna, 390 μm long for 230 GHz operation, made alignment and positioning difficult. Scattering from other metal structures on the substrate was a major problem; however, it should be understood if arrays of dipoles and their interconnections are going to be used to collect the incident radiation.

These measurement efforts, however, now seem more useful than just an intermediate step to developing rectennas for 10 μm operation. Recent thoughts for narrow beam width, point-to-point energy transfer make the millimeter wave rectenna a goal in itself in addition to being a scale model for the infrared rectennas. The millimeter wave rectennas for the energy beaming application would more appropriately be studied at a frequency below 100 GHz and should be based on the more efficient semiconductor rectifying diode.

The half wave resonant dipole was studied separately in order to determine the directivity and efficiency of the substrate mounted antenna. Bismuth microbolometers were used to measure the power received by the antenna. A low pass filter was incorporated into the antenna layout in order to prevent stray pick-up in the leads which connect the antenna to the external instrumentation. A paper titled "Measurement Techniques at the Conference on Millimeter Wave/Microwave Measurements and Standards for Miniaturized Systems, 6-7 November 1986 in Huntsville, Alabama is included in Appendix III.

Nickel - nickel oxide - nickel and nickel - nickel oxide - bismuth diodes were fabricated. Reasonably stable diodes with nonlinear current-voltage curves were obtained. In both cases, however, the curves were symmetric about the origin. We have not yet attempted to integrate the diode and the antenna into a rectenna configuration.

First, we report the results of a calculation of the power

density from the earth's radiant energy available to a satellite in earth's orbit. Next, the measurement of the substrate mounted antennas is presented. Included here is an explanation of the operation of the bismuth microbolometers and a description of the table-top antenna range used in the measurements. This is followed by a discussion of the potential use and results of efforts to produce a rectifying MOM diode. We concluded with some recommendations for future work in this area.

2. IR RADIATION FROM EARTH

The conversion of earth radiation at geosynchronous or low earth orbits requires very sensitive rectifying devices. The much lower spectral radiance from earth compared to the sun is shown in Figure 1. In the spectral region from approximately 7 μm to 20 μm, the radiation from earth and its atmosphere is a maximum. Contributions also exist from the reflected solar radiation, shown in Figure 1 for an earth reflectivity of ~0.1. A comparison with the maximum spectral radiance of the sun shows that the spectral radiance of the earth is over six orders of magnitude weaker than the spectral radiance of the sun. It should also be noted that, at 10 μm, the spectral radiance of the sun is still approximately three orders of magnitude greater than the spectral radiance of the earth. It is conceivable, then, that a power conversion system at 10 μm could employ solar radiation at 10 μm as an alternate to the earth or CO_2 laser as a source. A use of the sun radiation at 10 μm results in a reduction of four orders of magnitude relative to the solar maximum spectral radiance but does provide an alternate source which will be usable with the same converter developed for laser/earth applications.

2.1 Power Density from the Earth

In order to estimate the power available from earth at the satellite orbit, use has been made of various curves and data, given in "The Infrared Handbook".[5] For emission from earth's

3
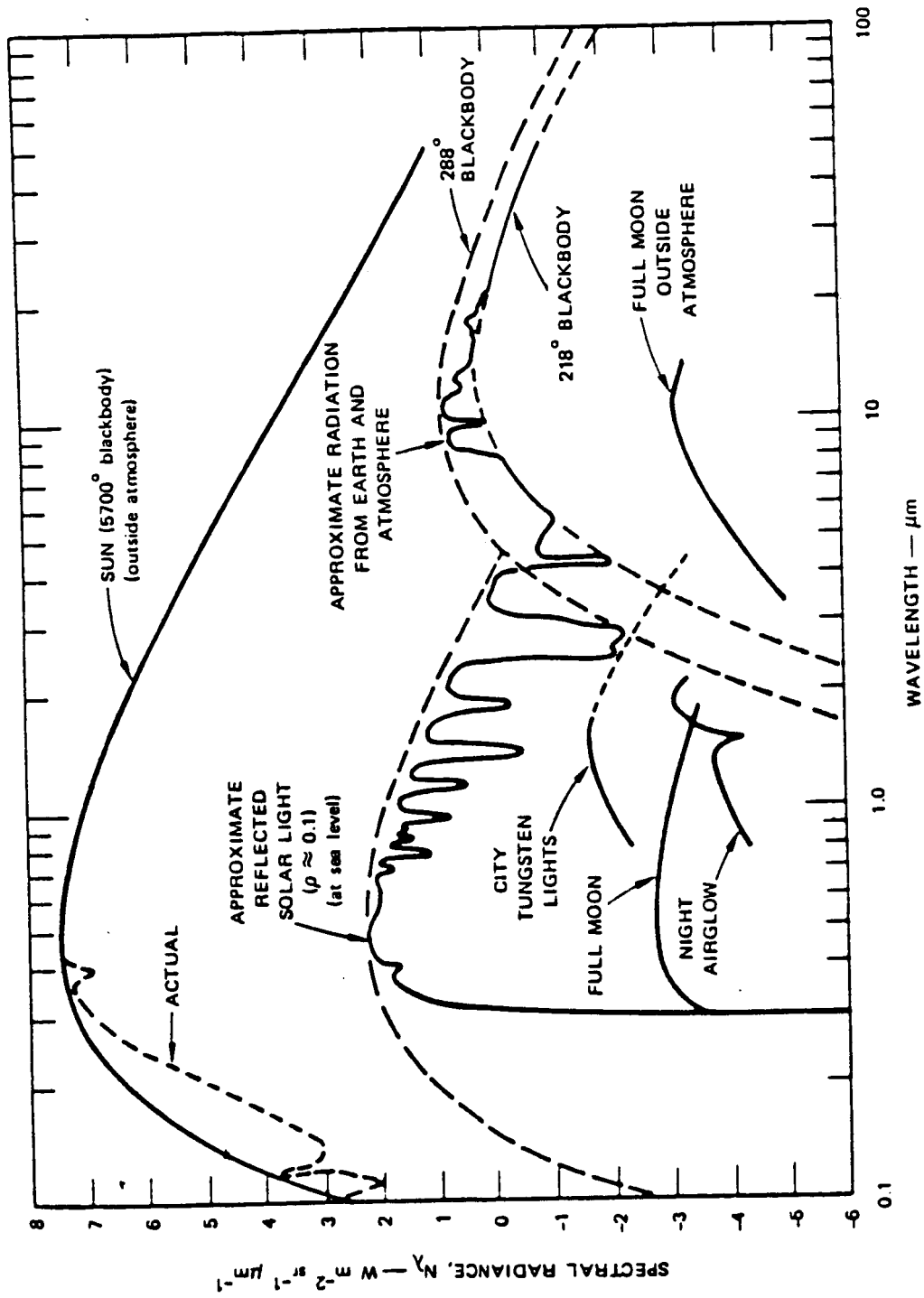
Figure 1. Spectral Radiance of Sun and Earth.

4

surface, several measured spectra have been recorded. All spectra have strong intensities in the spectral region 7-15 μm. Some of these spectral radiance curves are shown in Figures 2 through 10. Figure 2 shows day and night radiances of the same grass-covered field, whereas, Figures 3 through 10 show calculated spectral radiances to be expected by an exoatmospheric system over various portions of North America for different seasons of the year.[5] The prominent absorption band between 9 and 10 μm is due to ozone, and the strong absorption in the 14-16 μm region is due to CO_2 in the atmosphere. The seasonal variations as functions of latitude and sunlight provide large differences in the expected values of spectral radiance ranging from approximately 350 to 1100 $Wcm^{-2}sr^{-1}m^{-1}$ at peak value. The angle γ' given in the calculated spectral radiance figures is the angle given in Figure 11.

Diurnal variation is shown in Figure 12 for the 10 μm radiance of selected backgrounds on the plains as measured from the top of Pike's Peak. One can expect similar variations when observing earth from an exoatmospheric position.

Figures 13 and 14 show data from the Nimbus satellite flights with LOWTRAN 2 calculations and blackbody curves for comparison. The effects of intervening atmospheric molecular species are shown. The conversion of earth radiation is strongly influenced by the radiation exchange between the earth, its atmosphere, the sun and space. The radiance arriving at the exoatmospheric receiver can be distorted by emission and scattering from clouds. However, average radiances can be employed to obtain an idea of the radiation from earth available at the satellite. In order to provide an accurate estimate of cloud effects, a more detailed investigation must be performed than the one provided here.

For earth-atmosphere temperatures, the peak of the Planck blackbody curve lies in the 10 to 15 μm range. The earth (land and water) radiates essentially as a gray body of high emissivity ($\sim$0.9). The atmosphere is a mixture of clear (non-absorbing, non-emitting) gases, gases which have absorption bands and
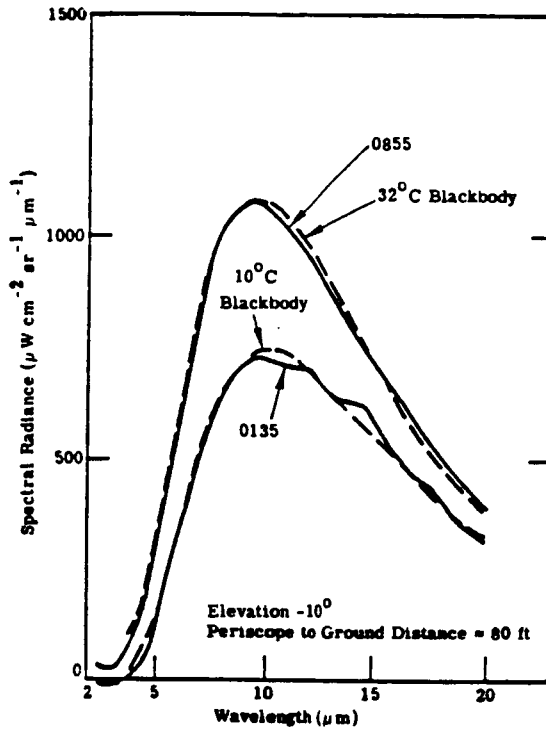
Figure 2. Day and Night Radiances of Grass-covered Field
(Peterson Field, Colorado).
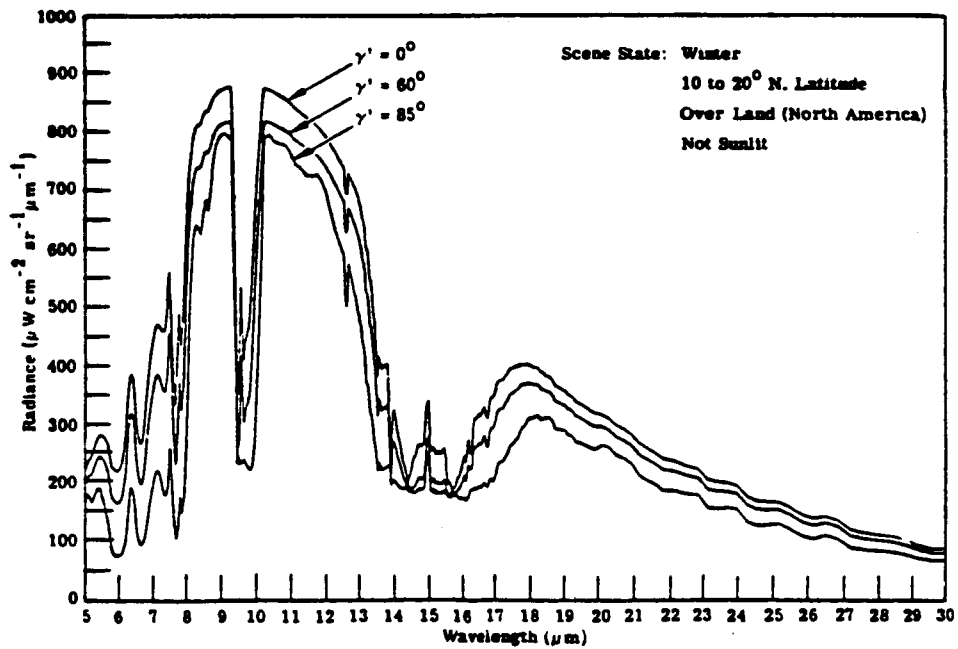
Figure 3. The expected value of spectral radiance for three γ' angles.

6
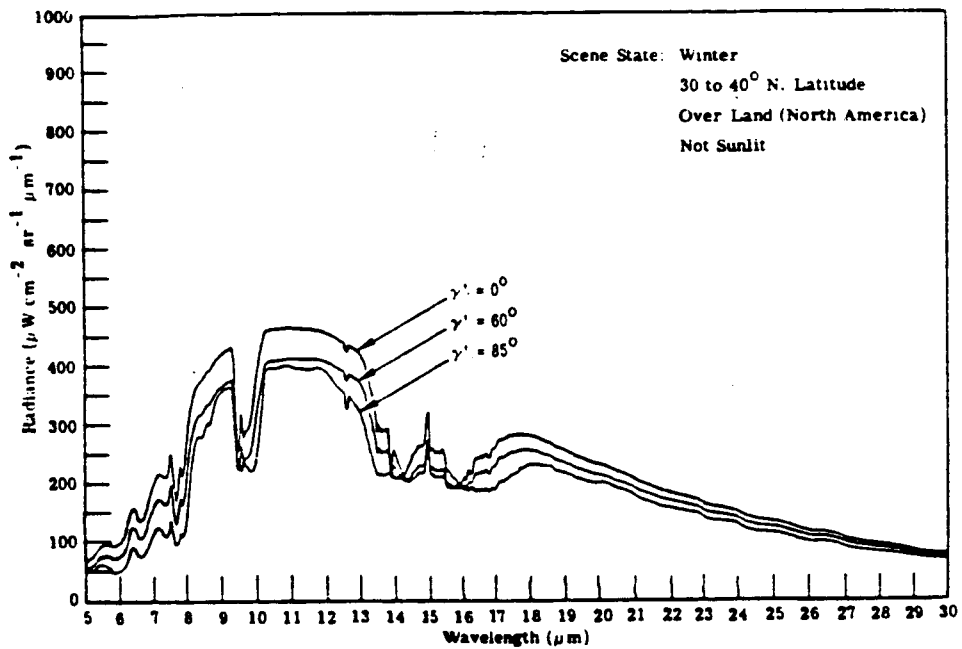
Figure 4 . The expected value of spectral radiance for three γ' angles.
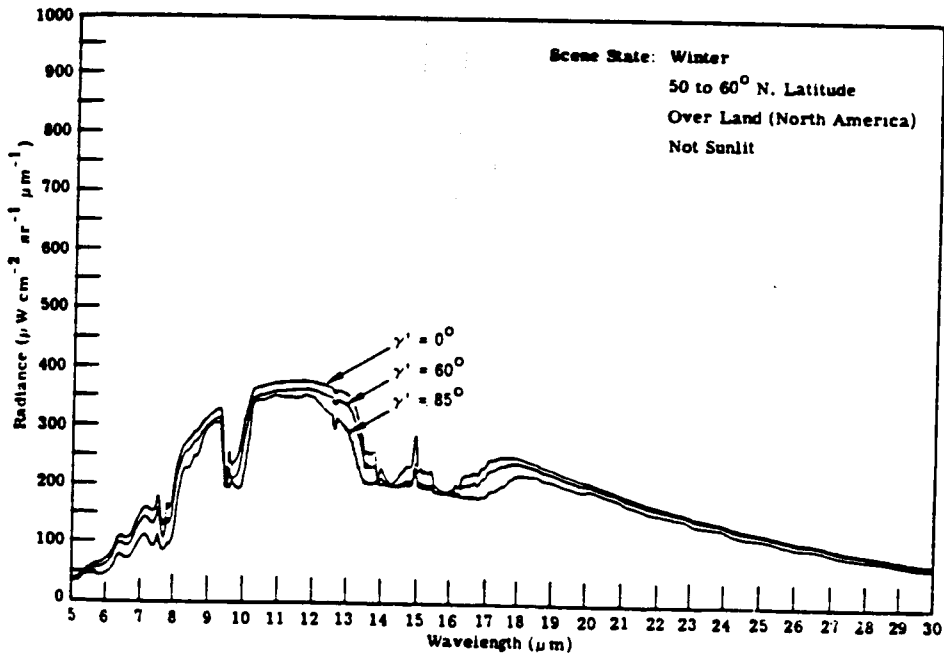
Figure 5. The expected value of spectral radiance for three γ' angles.

7
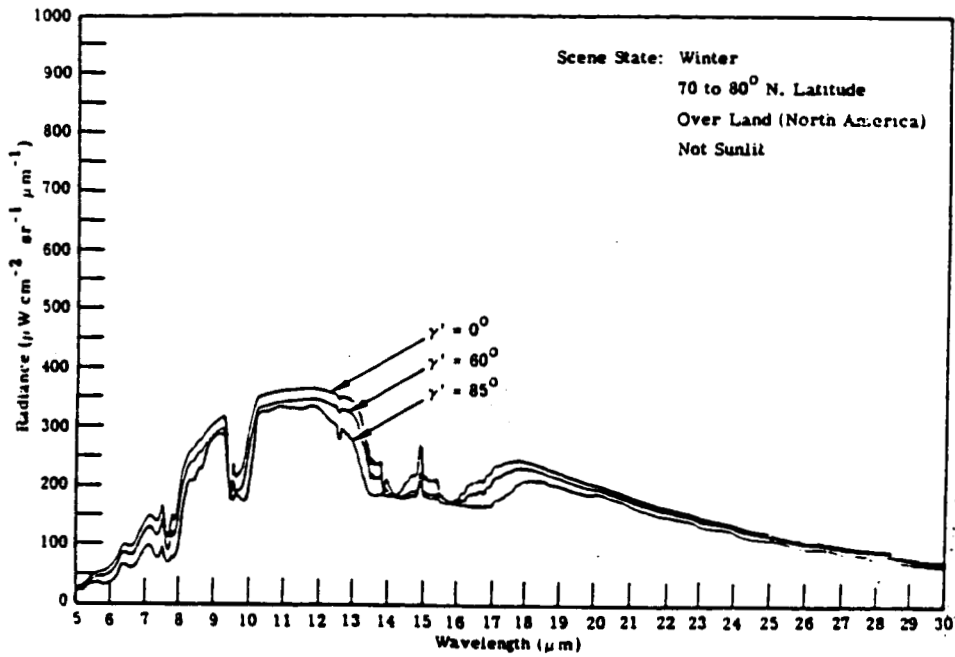
Figure 6. The expected value of spectral radiance for three y' angles.
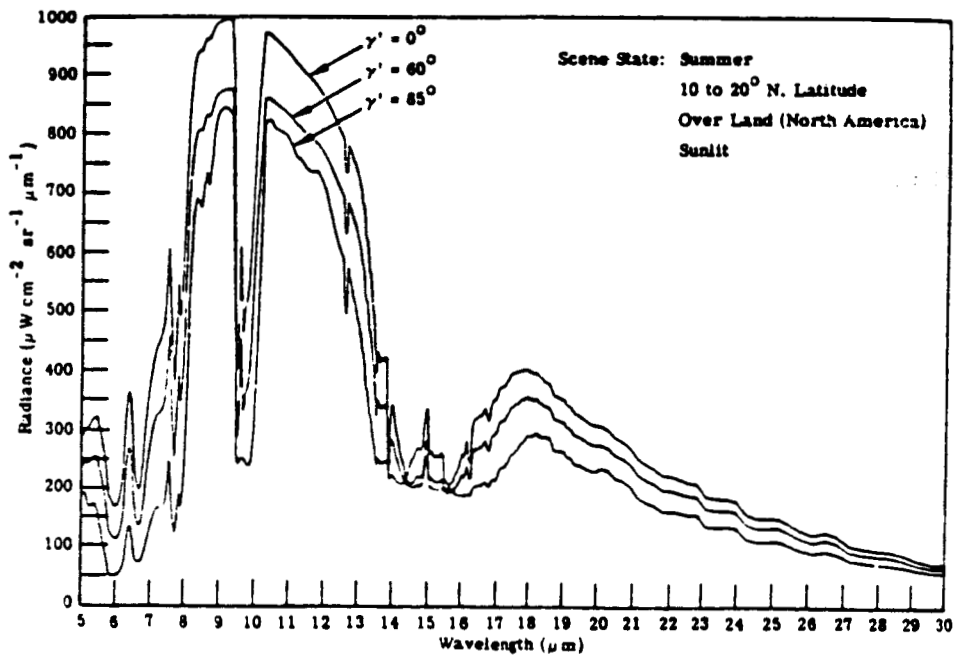
Figure 7. The expected value of spectral radiance for three y' angles.

8
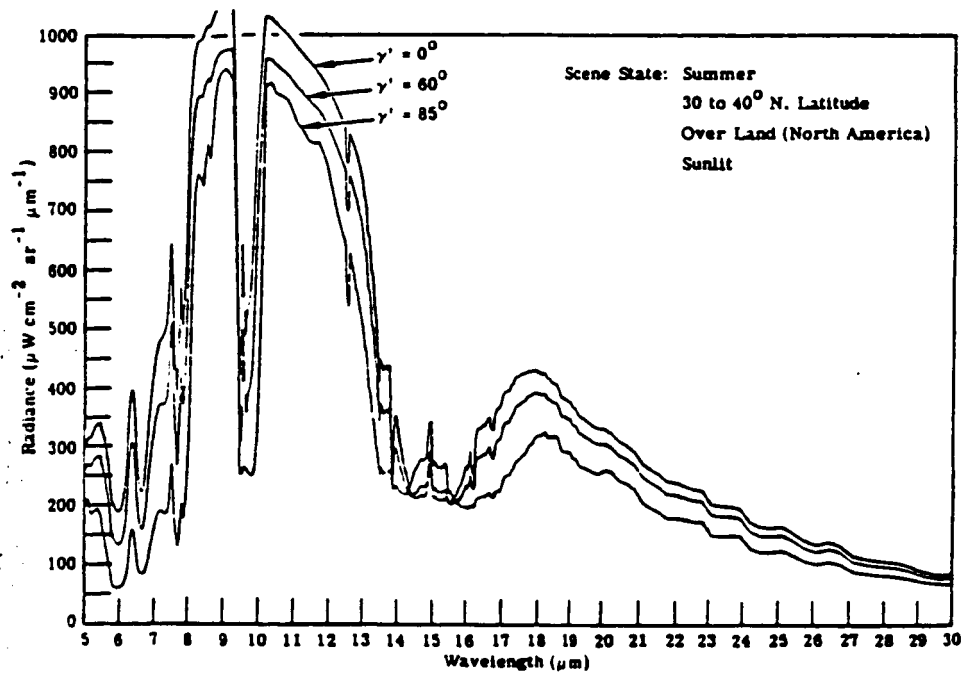
Figure 8. The expected value of spectral radiance for three γ' angles.
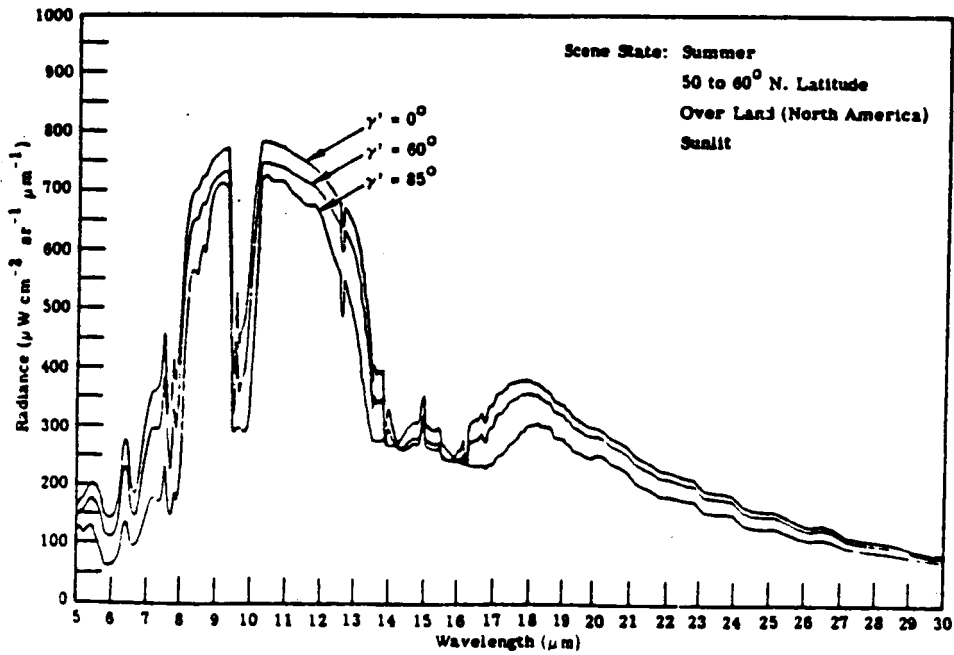
Figure 9. The expected value of spectral radiance for three γ' angles.

9
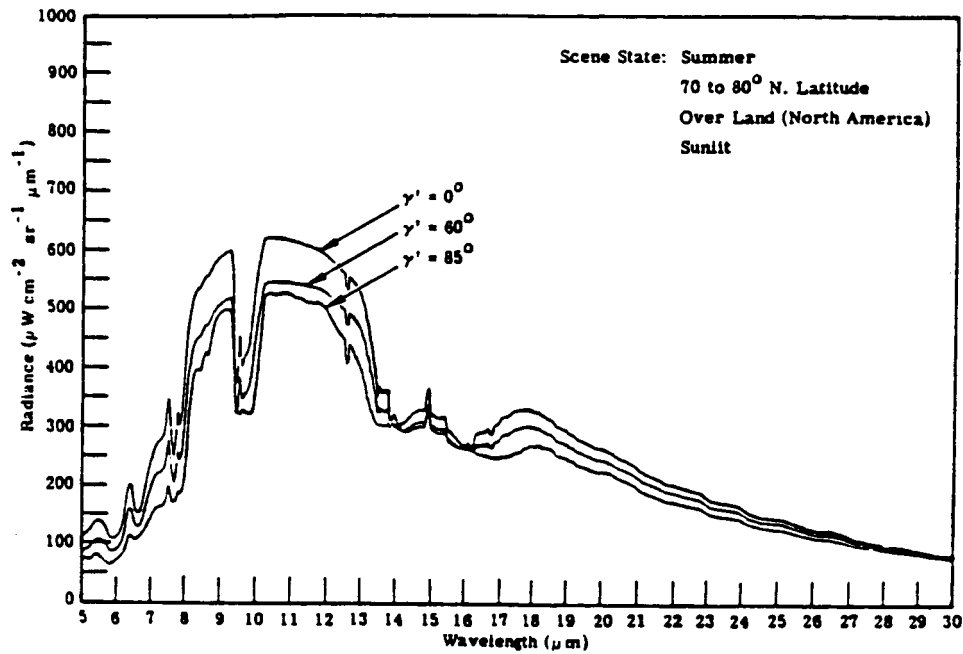
Figure 10 . The expected value of spectral radiance for three γ' angles.
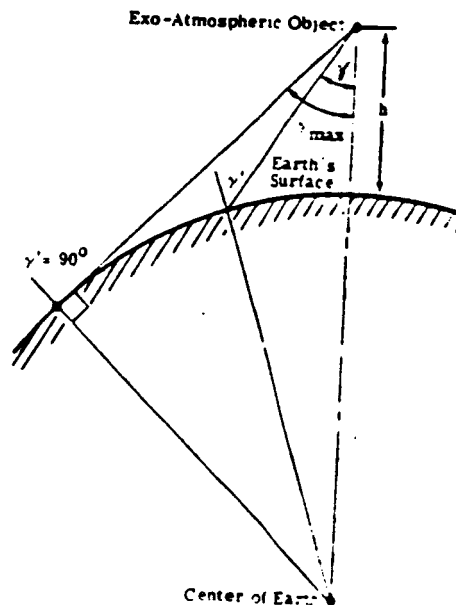
Figure 11. Cross-section view of the geometry pertaining to the calculation
of the thermal radiance field at an exoatmospheric object.

10
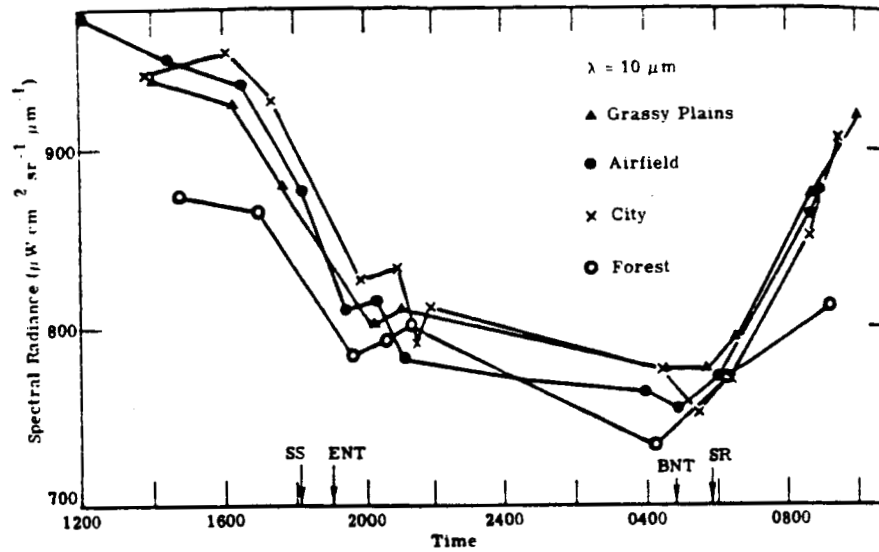
Figure 12. Diurnal variation in the 10 μm Radiance of selected backgrounds. SS = sunset; SR = sunrise; ENT = end of nautical twilight; BNT = beginning of nautical twilight.
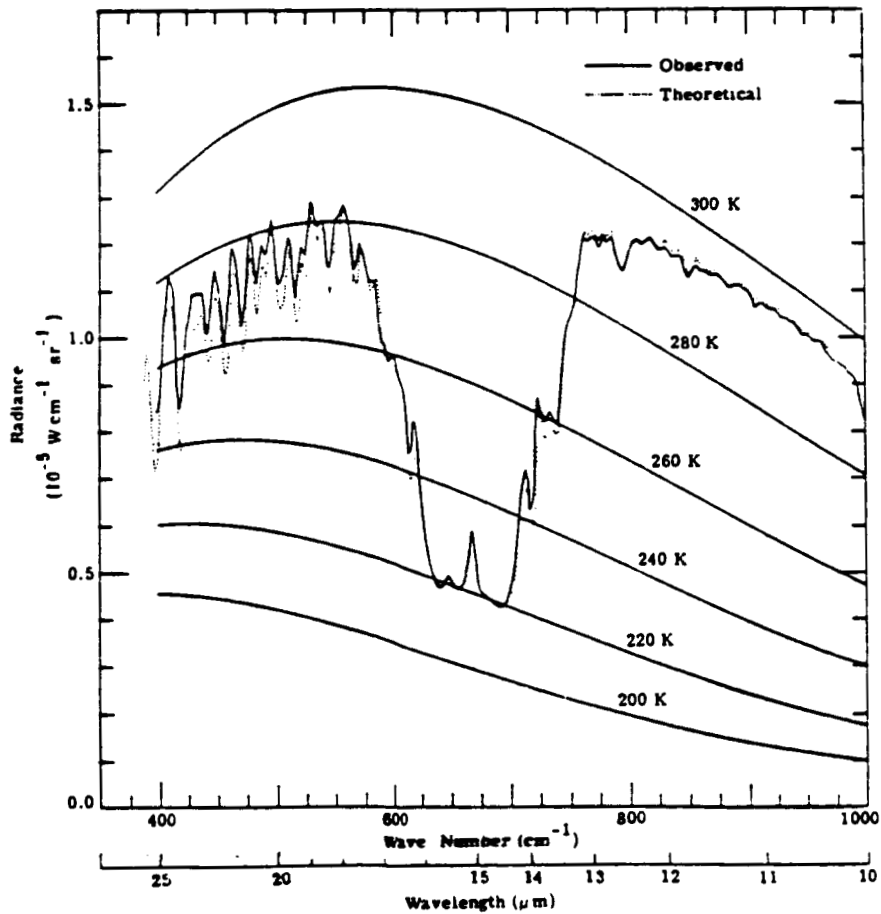
Figure 13. 400 to 1000 cm^{-1} portion of the Nimbus spectrum. The dashed curve is calculated with line-by-line method.

11
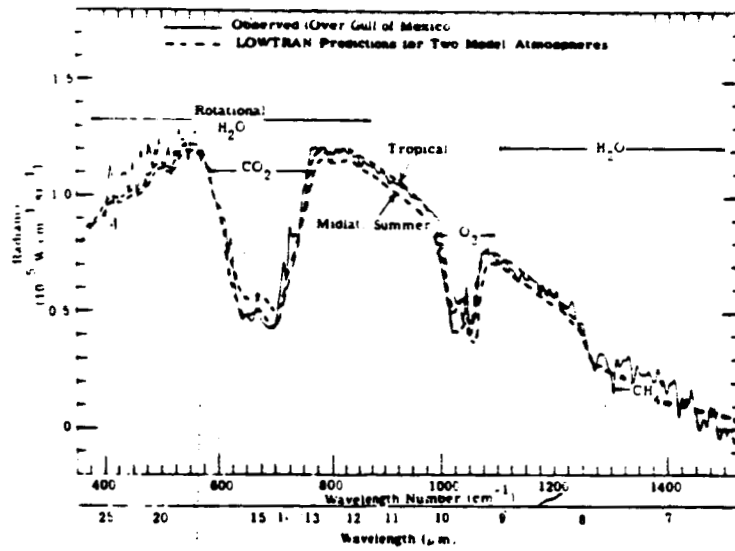
Figure 14. Comparison of LOWTRAN 2 calculation with Nimbus data.
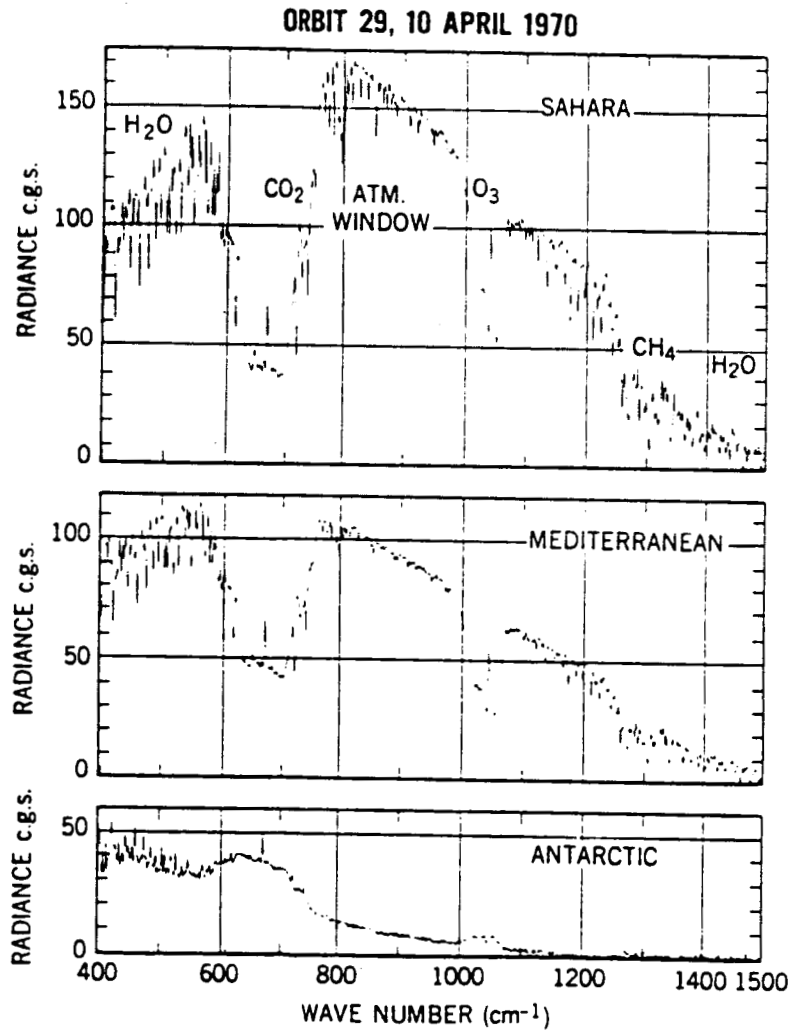
Figure 15. Thermal Emission Spectra of the Earth from IRIS D Experiment on NIMBUS IV.

aerosols (clouds, haze, dust, etc.) which scatter, emit and absorb. Figure 15 shows these effects, described by Yates,[6] in the following manner.

The spectral range is 25 to 6.5 μm and three geographical areas are represented under clear, cloudless conditions -- the Sahara Desert, the Mediterranean Sea nearby, and finally the Antarctic continent. The Sahara appears as a 40 to 50°C blackbody peaking between 14 and 11 μm viewed through the atmosphere. H_2O vapor, CO_2, O_3 and CH_4 (as well as some minor constituents) have absorption bands in this region and show as such. If the atmosphere were at the same temperature as the desert below, these bands would disappear and a smooth blackbody curve would be seen. The atmosphere, however, is neither isothermal nor homogeneous but has a temperature structure typically like that shown in Figure 15.

Two features of particular interest are the CO_2 band between 17 and 13 μm and the O_3 band between 10 and 9 μm. The CO_2 absorption band has three branches, labeled P, Q and R, respectively, as identifiable regions. A very narrow central Q-branch of extremely high absorbing (and hence emitting) power is bracketed by two broad branches, the P and R, of lower, but still fairly high absorbing power. The O_3 band, on the other hand, consists of two broad branches separated by a narrow region of fairly low absorptivity. In the P, Q and R branches of the CO_2 band, the atmosphere is essentially opaque and one sees only radiation from the gas integrated over a path which reaches deeper into the atmosphere as the absorptivity of the gas decreases. One sees deeper in the P and R branches than in the Q-branch. The bulk of the radiation for the P and R branches arises in the upper troposphere and lower stratosphere, the region of lowest temperature in the atmosphere. The Q-branch sees mainly the middle stratosphere where the temperature is higher and hence it appears as a warm spike between the P and R branches. Note that there is relatively little difference between the absolute levels in the CO_2 band for all three curves.

Over the Mediterranean, the upper troposphere is actually a little warmer than over the Sahara though, of course, the water is much cooler than the desert. The Antarctic continent is colder than the upper troposphere about it and the P and R branches both appear reversed from the other two situations.

The O_3 band behaves in a similar fashion with one notable exception. The central spike over the Sahara and Mediterranean appears warm because one sees the lower troposphere and the surface. Over the Antarctic, where the surface is colder, not warmer than the air, this central spike is reversed. Further differences, which contribute to the larger variations in absolute level for the O_3 band, are that CO_2 is uniformly distributed throughout the atmosphere whereas O_3 has a concentration peaked in the lower stratosphere and that the O_3 layer is not entirely opaque so that the surface of the earth is always contributing.

For an estimate of the power density from the sunlit earth considered equivalent to a blackbody temperature of $288^{\circ}K$, we consider this earth radiation as the highest value that will normally be encountered when a satellite views the surface of the earth. The power density P_B at the satellite receiver is

$$P_B = \frac{B_R \ A_V \Delta\lambda}{R^2}$$

B_R = spectral radiance in FOV
$$(Wm^{-2}) \ \mu m^{-1} \ sr^{-1}$$

A_V = area of radiating body in FOV, m^2

$\Delta\lambda$ = optical bandwidth

We assume that the terrestrial surface is a Lambertian reflector, reflection coefficient $\approx$ 0.1. The spectral radiance, taken as an approximate value from some of the figures given above, is

$$B_R = 10 \text{ W/m}^2 \mu m^{-1} sr^{-1}$$

If we assume this value to be an average for an optical bandwidth $\Delta\lambda = 4 \mu m$, then

$$P_B = \frac{40 A_V}{R^2}$$

For observation of the entire earth by the antenna,

$$P_B = 3.76 \text{ W/m}^2$$

The antenna size required to receive the total earth radiation when the fill factor of the earth in the antenna aperture is one can be calculated by setting the quantity $R\theta$ equal to the earth's diameter (1.28×10^7 meters). Here θ is the antenna angle and R is the geosynchronous satellite distance from earth (3.7×10^7 meters). Then, $\theta = 0.3459$ radians, and the effective antenna diameter, $D = 1.22 \lambda/\theta$ is equal to 37.5 μm. On the other hand, the effective area of a half-dipole antenna is A $= 1.64\lambda^2/4\pi$ so that, for $\lambda = 10.6 \mu m$, the effective diameter is D $= 4.32 \mu m$ and $\theta = 2.994$ radians. This beam would more than fill the earth.

For a more accurate estimate of the power density at the satellite receiver, the results of Appendices I and II are employed to give results as a function of satellite altitude and antenna field-of-view. In Appendix I, the dependence of power received at the satellite is calculated as a function of the geometry of the satellite relative to earth. The resulting expression for power density involves what we have called the power collection factor, a function of satellite altitude and field-of-view of the receiving antenna. The expression can be employed with any spectral radiance which would vary with season, weather conditions, and geographical location of satellite. The radiation relations are given as Appendix II with spectral radiance and the radiance for two spectral bandwidths (8-13 μm

and 6-16 μm) given for the conditions presented in Figures 10-17 of this section. The power density at the satellite is given by the relation of Appendix I:

$$\frac{P}{A_s} = B_I \, F(\theta, h) \, ,$$

where B_I is the radiance integrated over the optical bandwidth of the system (see Appendix II) and $F(\theta, h)$ is the power collection factor (Appendix I).

2.2 Collection Factor

Calculations of the dependence of the collection factor on the satellite's field-of-view are shown in Figure 16 for satellites at heights, h, ranging from 200 to 22,990 miles, the latter being the position of geosynchronous orbit. For each value of h, the factor increases rapidly as the field-of-view is increased up to the value θ_m which corresponds to the angle at which all of the earth's surface is visible. For angles less than θ_m, the collection factor is shown to be independent of the height. This occurs because for constant θ, the area viewed by the satellite increases as h^2, whereas the power density of the earth's emittance decreases as $1/h^2$. Thus, these two terms cancel, resulting in the collection factor being independent of height in this regime. For $\theta > \theta_m$, the satellite views the earth against a cold background. Thus, the collection factor remains constant.

The dependence of this fill factor on height for $\theta \geq \theta_m$ is shown in Figure 17 and demonstrates that, for satellites orbiting within 1500 miles of the earth's surface, the loss in energy collection due to geometrical factors is less than 50% of the maximum possible factor.

From the results presented in Appendix II and these calculations, the terrestrial radiant power available for power conversion can be calculated as a function of the spectral bandwidth of the receivers, the satellite's height above the earth and field-of-view angle. If it is assumed that power is

16
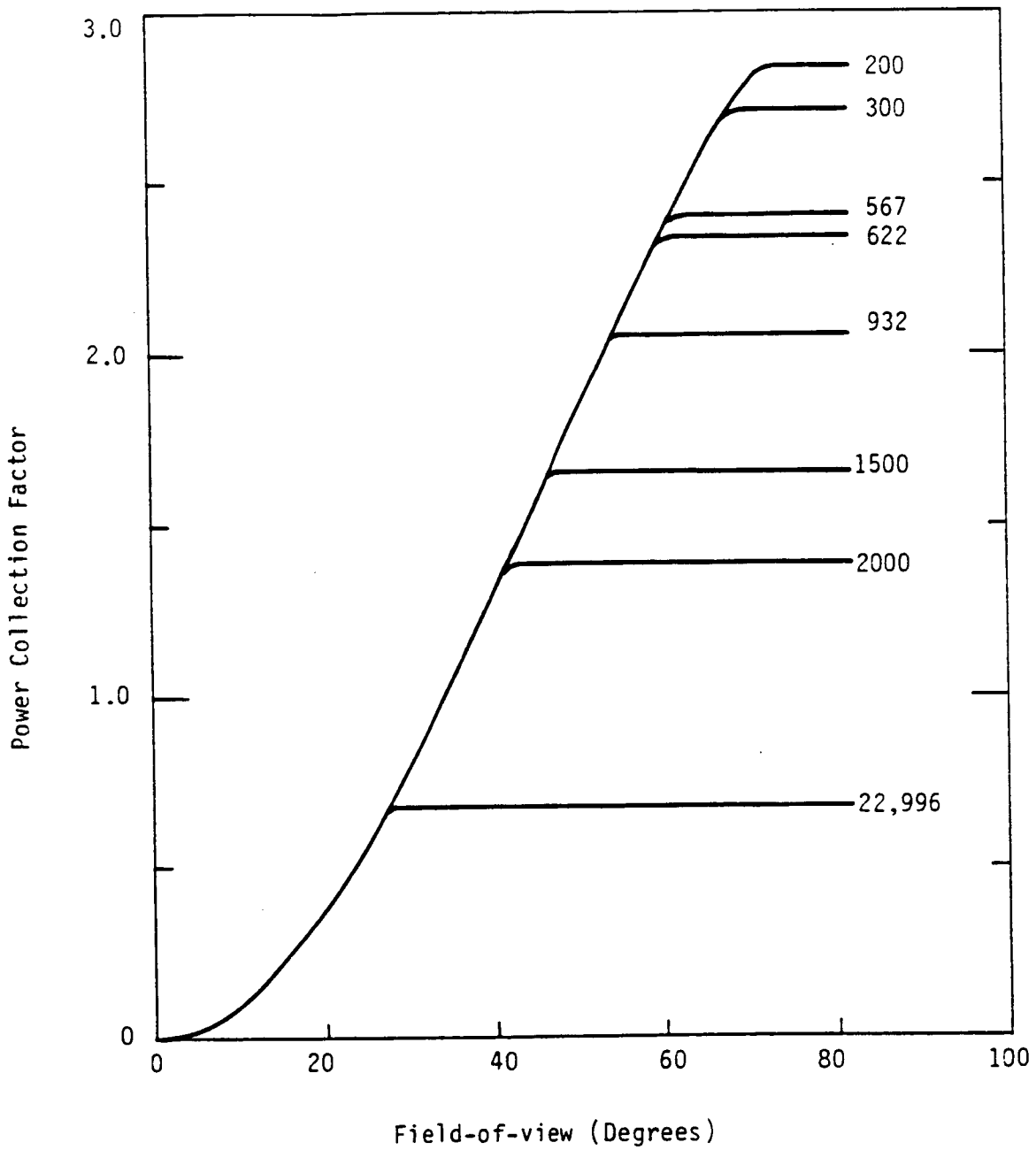
Figure 16. Power collection factor as a function of FOV.
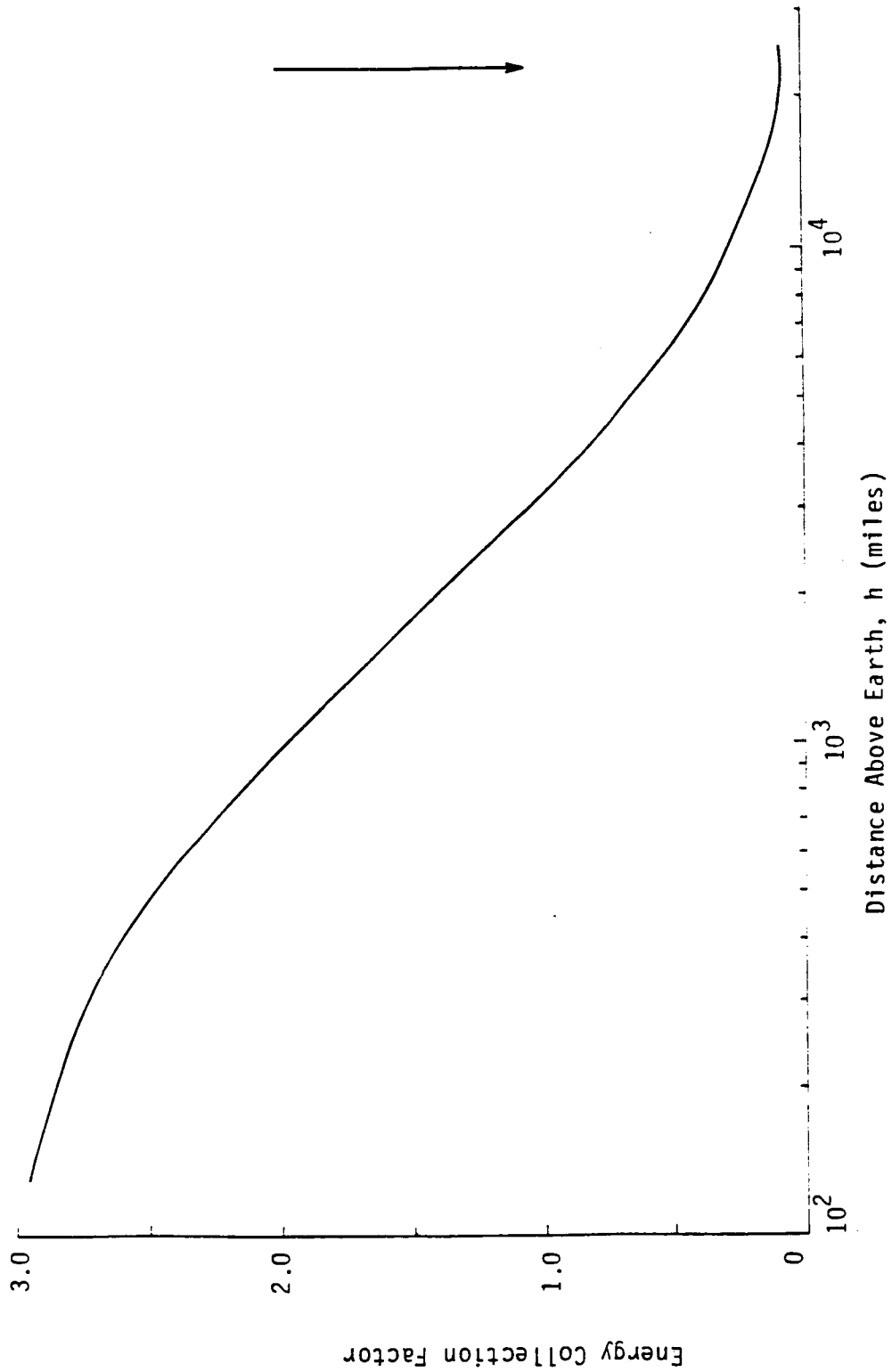
Figure 17. Power collection factor dependence on height for $\theta \geq \theta_m$. Arrow indicates position of geo-synchronous orbit.

only available in the 8-13 μm wavelength band, then the power densities for satellite heights of 200, 300, 622, 932, 1500, 2000 and 22,996 miles are given in Table 1. Included in the table are $F(\theta, h)$, the maximum FOV, θ_m and the power density for the extreme cases given in Figures 6 and 8. If the capability of the rectifier elements is extended to cover the 6-16 μm band, the power densities for the two cases given in Table 1 would be increased by a factor of approximately 1.4. Table 2 gives the power produced by 10% efficient rectenna arrays ($10^3 m^2$ and $10^2 m^2$) with the power densities listed in Table 1.

The power levels indicated in the tables can meet the power requirements of several satellite systems so that the concept of power conversion of earth radiation has considerable merit. It is also anticipated that development of the rectennas will result in efficiencies in excess of 10%.

It should be noted that besides calculating the energy available for power conversion, these equations also specify the angles required to optimize the antenna's collection efficiency. The dependence of θ_m and h, plotted in Figure 18, shows that θ_m decreases as h increases. However, for orbitals at heights less than 100 miles, the dependence of θ on h is small and large collection angles are required to collect all the radiation. For h above 100 miles, θ becomes less than 70° and therefore does not present a problem. Because of the large angles required at low h, it is possible that there may be a considerable mismatch between the cone available to collect radiation and the antenna patterns. This mismatch problem decreases with increasing height.

Thus, as may be expected from a qualitative study of the problem, Figure 17 demonstrates that the fill factor is a maximum for orbital satellites (~ 200 miles from the earth's surface) but requires a large field-of-view (> 70°) to capture all of the energy emitted by the earth. If this field-of-view can be realized, then the loss of energy with increasing height is less than expected for orbitals up to 2000 miles from earth.

Table 1

Power Densities as Function of
Altitude for Wavelength Band 8-13μm

Altitude (h)	$F(\theta,h)$	θ_m	P/A_s (W/m^2) Figure 15	P/A_s (W/m^2) Figure 13
200 miles	2.84	72°	134.13	45.27
300	2.70	68	127.52	43.04
622	2.33	59	110.05	37.14
932	2.05	54	96.82	32.68
1500	1.64	46	77.46	26.14
2000	1.375	42	64.94	21.92
22,996	0.66	26.8	31.17	10.52

Table 2

Power Produced by 10% Rectenna Arrays
with Power Densities Given in Table 1.
Wavelength Bandwidth = 8-13μm

Altitude (h)	1000 m^2		100 m^2	
	Figure 13	Figure 15	Figure 13	Figure 15
200 miles	13.413 kW	4.527 kW	1.341 kW	453 W
300	12.752	4.304	1.275	430
622	11.005	3.714	1.100	371
932	9.682	3.268	0.968	327
1500	7.746	2.614	0.775	261
2000	6.494	2.192	0.649	219
22,996	3.117	1.052	0.312	105
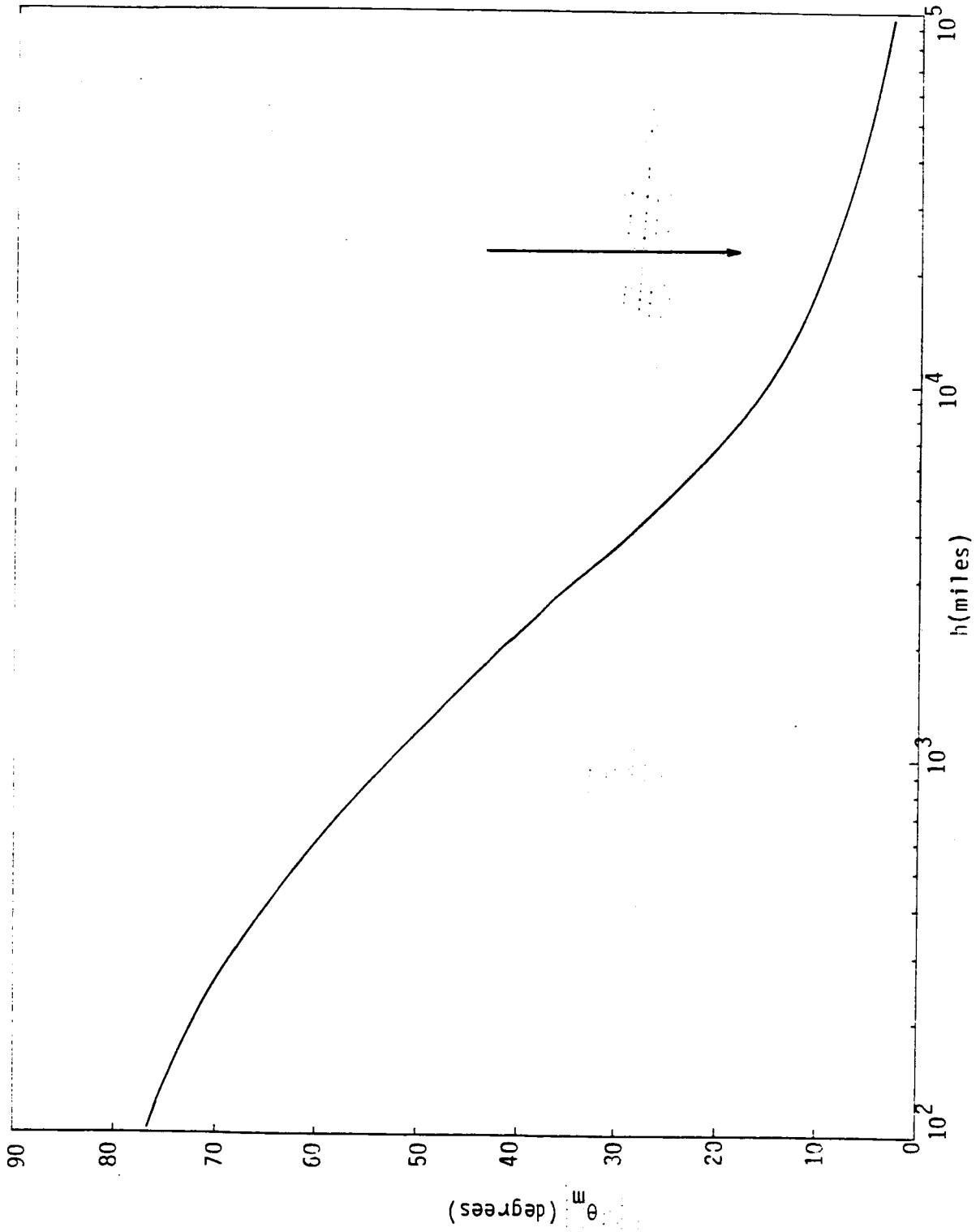
Figure 18. Dependence of θ_m on altitude, h. Arrow indicates geo-synchronous orbit.

22

3. SUBSTRATE MOUNTED ANTENNA MEASUREMENTS

It is necessary to study the antenna by itself before integrating it with the rectifying circuit for two important reasons. First, the power delivered to the rectifying circuit must be known in order to choose a diode with the appropriate barrier height. Recent work by Boyakhchyan, et al.[7] and Ashok[8] has shown how the parameters of Schottky diode rectifiers should be adjusted for different input power levels. The results of numeric calculations in this work show that choosing the proper parameters makes a significant difference in conversion efficiency. It is assumed that the parameters of the MOM diode should also be suitably chosen according to the input power level. Second, the power captured by the antenna must be measured if the efficiency of the rectenna is to be divided into antenna efficiency and rectification efficiency. The properties of substrate mounted antennas are not well understood, and in order to make the best possible rectenna device, the efficiency of the antenna must be optimized (at least to first order) before adding the rectifying circuit.

A table top range with appropriately placed absorber is generally used to measure the field patterns of the substrate mounted antennas at the higher millimeter wave frequencies. The basic measurement scheme consists of a millimeter wave source with power meter and standard gain horn, a chopper to modulate the radiation, an antenna positioner, and the antenna under test which has some type of integrated detector. Quasi optical components can be used to collimate the incident radiation or adjust the polarization of the beam.

Three types of integrated detectors are used: these are Schottky barrier diodes, thermocouples and bolometers. Beam lead diodes bonded into the circuit and monolithic diodes fabricated with the antenna are known. The diode can be operated as a square law detector or with a local oscillator for heterodyne detection.[9-12] The local oscillator can be fed to the mixer diode via transmission lines on the substrate[10] or quasi

23

optically by irradiating the antenna with both the RF and the LO.[11,12] A bismuth-antimony thermocouple has been reported.[13] This detector has the advantage of bias-free operation. The third detector type is the microbolometer.[14] Typically, bismuth is used because of its high resistivity.

We have used bismuth microbolometers in this work. This detector is the easiest of the three to fabricate and is sensitive enough to make the required measurements. The microbolometer functions by thermal heating from the induced millimeter wave frequency currents in the antenna. The increased temperature of the device changes its resistance which can be measured by an outside detection circuit. It is possible to calibrate the responsivity and NEP of these detectors electronically.[13-15] A known RF signal, usually in the MHz range, is placed across the detector to simulate the millimeter wave operation. From this, the responsivity and NEP can be measured.

3.1 Bismuth Microbolometers

The responsivity (volts/watt) of the bolometer is of primary interest because it gives the ratio of detector voltage output to VHF or millimeter wave (MMW) power absorbed under a given bias current. The responsivity of the bolometer can be determined from a series of dc measurements. Experiments carried out at 10-90 MHz showed that this method of determining the responsivity accurately measures the applied power to within roughly 10%.

For small applied power, the resistance of the bolometer can be modeled by

$$R = R_o + \beta P,$$

where R_o is a cold resistance term and P is the power dissipated in the bolometer. By taking the derivative of the resistance with respect to power, we get β which is the measure of how the resistance changes with applied power. When operating as a power detector, a constant current is supplied to the bolometer so that

the change in resistance due to an applied VHF or MMW signal can be measured by observing the change in voltage across the detector. The responsivity is given by

$$R = I_{bias} \text{ (volts/watt)},$$

and the detected power is given by

$$P = V_{detector}/R.$$

Since the detector is biased with a constant current, the VHF or MMW signal must be modulated in order to measure the change in bolometer resistance. $V_{detector}$ is equal to the difference between the bias voltage and the voltage across the bolometer when the power is applied. Most often, $V_{detector}$ is measured with a lock-in amplifier.

3.1.1 dc Responsivity Measurement

The procedure to determine the responsivity starts by measuring the resistance versus bias power of the bolometer. The voltage across a 1k ohm precision metal film resistor in the current biasing circuit is measured to determine the bias current. The voltage measurements across both the metal film resistor and the bolometer are made with 5-1/2 digit multimeters. The circuit used to make the resistance versus bias power measurements is shown in Figure 19, and a typical resistance versus bias power plot is shown in Figure 20. In the figure, two lines are plotted which represent measurements taken several hours apart. It is seen that, even though the absolute resistance has changed over time, the slope of the line (and thus the responsivity) has not changed.

The responsivity is calculated by taking the slope of the line at the desired bias power. Since the responsivity is directly proportional to the bias current, a larger bias current is desirable, although the bias power plus the detected power should not be too large to cause the bolometer to be unstable.
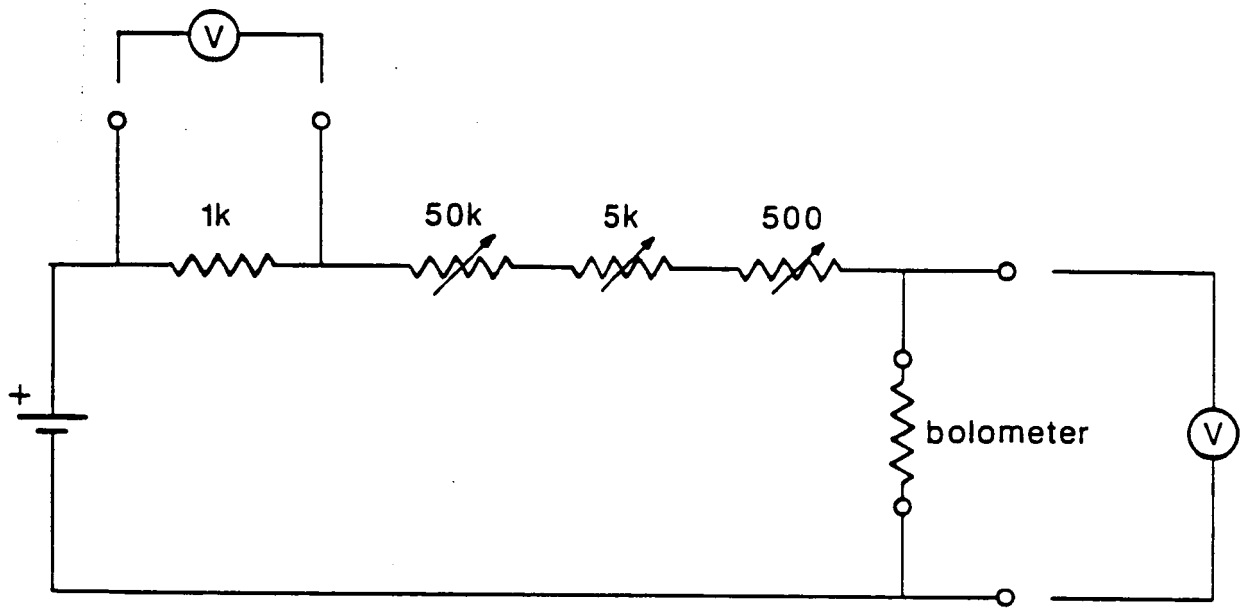
Figure 19.   Bias Power Versus Bolometer Resistance Measurement
               Circuit.

BIAS POWER VS RESISTANCE
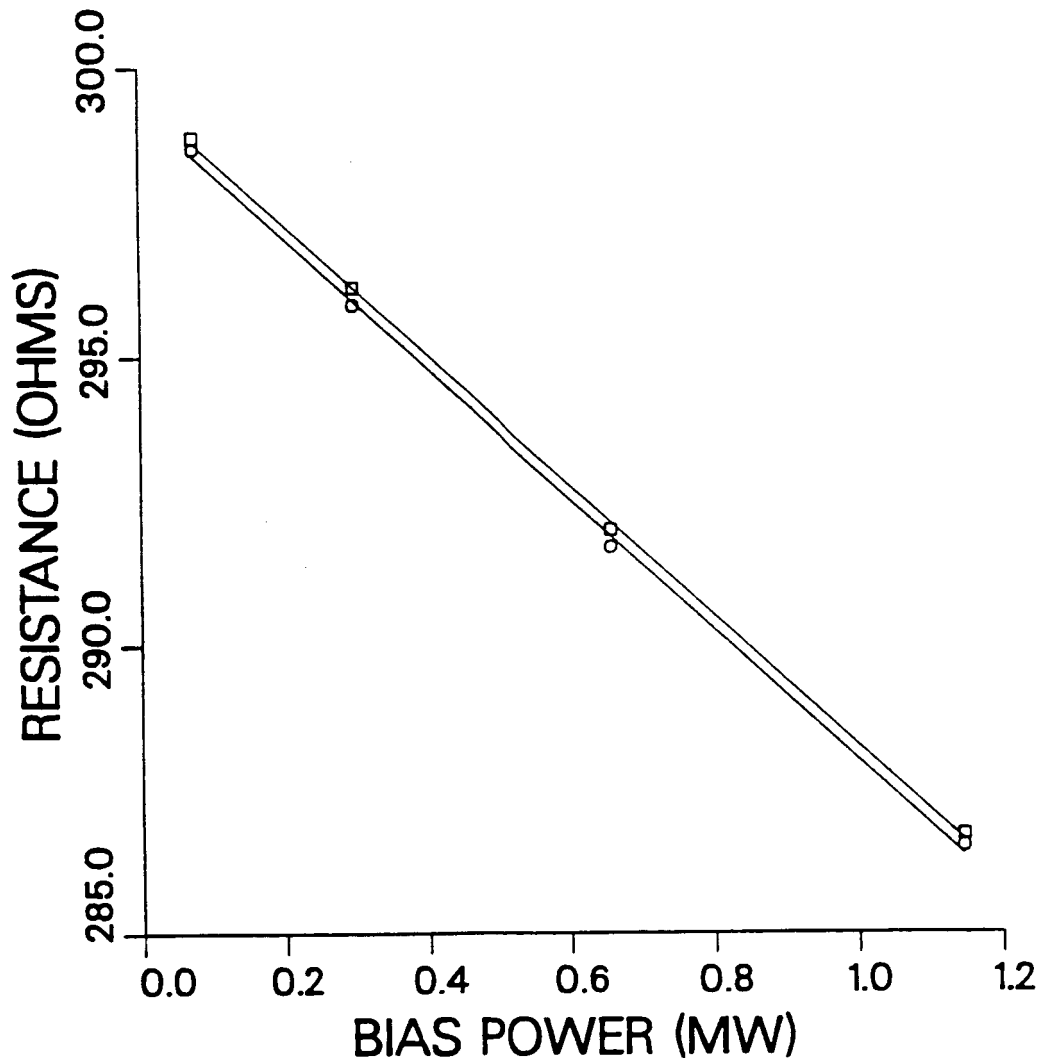
Figure 20. Sample Plot of Bias Power Versus Bolometer Resistance

The responsivities for 10 different bismuth bolometers are given in Table 3. All of the bolometers were 10 μm wide and 1500 Å thick. The lengths of 80, 40 and 20 μm were chosen because the horseshoe shaped bolometer used in the antennas is a parallel combination of one 40 μm bolometer and two 20 μm bolometers. An additional 10 μm Bi-Au contact region is added to each end of the bolometer so that the bolometer can be connected to the test circuit via large gold pads.

3.1.2 VHF Simulation

A VHF test circuit was assembled to test the accuracy of the dc measured responsivity. The idea was to calculate the detector responsivity by the dc measurement technique, and then apply a known VHF signal to the bolometer and compare the detector measured power with the actual power applied. The thermal time constant of the bolometer is too long to track the VHF signal, so the detector will measure the rms power. There is no difference between the operation of the bolometer at VHF and at MMW frequencies since both signals are faster than the time constant of the bolometer. Therefore, this is a meaningful way to test if the responsivity calculated from the dc bias power versus bolometer resistance plot will be accurate at millimeter wave frequencies.

The VHF test circuit is shown in Figure 21. The VHF signal is turned on and off at a given modulation frequency (10-500 Hz) for the operation of the lock-in amplifier. A high pass filter is placed after the VHF generator to ensure that no remnant of the modulation signal is introduced into the circuit. The 3-stage low pass filters between the bolometer and the bias circuit and between the bolometer and the lock-in amplifier have over 80 dB attenuation at 10 MHz. The low pass filter to the bias circuit is necessary to isolate the VHF generator and the bias supply. The low pass filter to the lock-in amplifier is needed to prevent demodulation of the VHF signal on the nonlinear elements of the preamp. Such demodulation yields erroneously large detector voltage measurement. Blocking capacitors are used

	BOLOMETER LENGTH (microns)		
	80	40	20
Responsivity (volts/watt)	4.8	7.0	2.8
	11.7	9.0	9.8
	5.4	16.1	6.7
			2.7

Table 3.   dc Responsivities for the Different Length Bolometers.
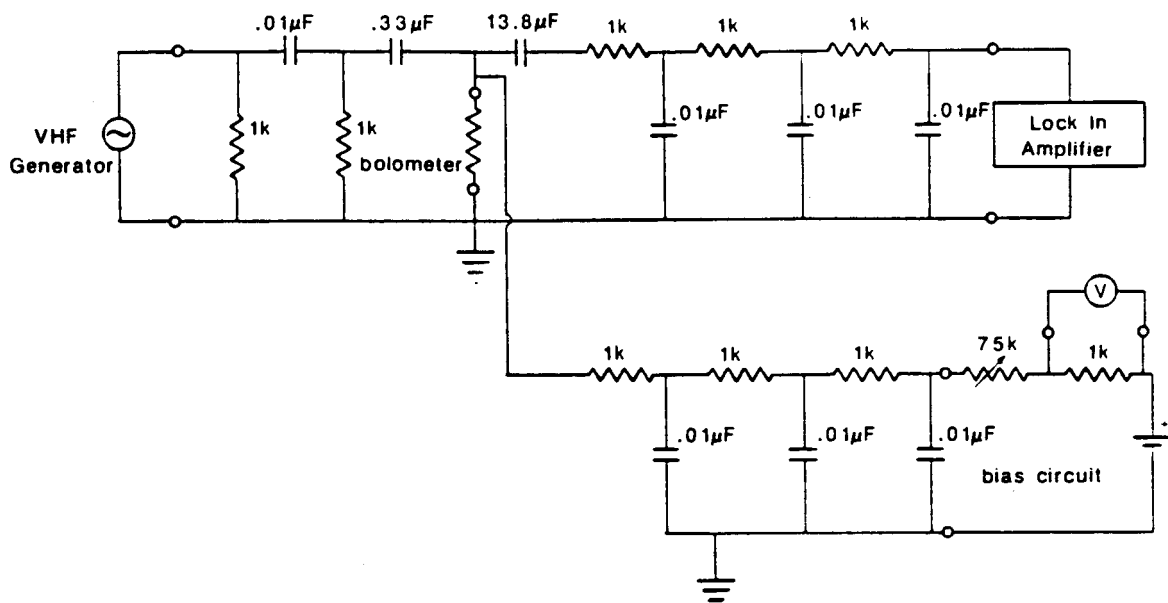
Figure 21. The VHF Test Circuit

to prevent the dc bias current from entering the VHF generator or the lock-in amplifier.

The first measurement performed on the VHF test circuit was to compare the change in bolometer resistance with dc power and VHF power. This was done by first selecting a bias point for the bolometer. Then additional dc power was added to the bolometer, and the change in resistance was noted. The bolometer was set back to the bias point and an equivalent rms VHF power was applied. The change in resistance was measured by a lock-in amplifier. The VHF signal was turned on and off at a 10 Hz rate, and the voltage measured on the lock-in amplifier was equal to the rms value of the bias current multiplied by the change in resistance. The results are shown in Table 4. In eight of the ten bolometers shown, the agreement was 5% or better.

In the second measurement, the VHF power measured by the bolometer was compared to the actual power applied to the detector. First, the dc responsivity of the detector was measured, and the bolometer was biased with an appropriate current (1-2 mA). A modulated VHF signal with known power (approximately 40% of the dc bias power) was applied to the bolometer. The detector voltage, measured with a lock-in amplifier, was divided by the dc responsivity to yield the measured power. The percent difference between the measured power and the actual power is shown in Table 5 for the different length bolometers. In general, the bolometer measured power was about 10% less than the actual power.

The dc resistance measurements of the 20 μm bolometers were the largest source of error in the responsivity calculations of these elements. These measurements were often at or just below the specified accuracy of the 5-1/2 digit multimeter used in the experiment. The data for these bolometers is included for completeness. The difficulties in measuring the small changes in resistance will not be a problem for the antenna measurements since the 80 μm bolometer's resistances are four times greater than the 20 μm bolometers.

The VHF signal was increased from 10 MHz to 90 MHz with no

	BOLOMETER LENGTH (microns)		
	80	40	20
% difference in resistance	3.5	10.9	3.5
	4.3	2.9	1.67
	16.9	5.1	5.0
			2.6

Table 4.   Percent Difference Between the Change in Resistance of
the Bolometers for Equivalent dc and VHF Power.

	BOLOMETER LENGTH (microns)		
	80	40	20
% difference in measured and actual VHF Power	9.8	10.8	8.8
	10.7	19.4	2.1
		6.8	15.8
			24.9

Table 5.   Percent Difference Between the Measured and Actual VHF Power Applied to the Bolometers.

change in measured power. 90 MHz was the upper limit because of the bandwidth of the oscilloscope used to measure the actual VHF power.

3.1.3 Thermal Time Constant

The effect of the modulation frequency of the VHF or millimeter wave signal has also been explored in the experiment. The thermal time constant of the bolometer is a measure of how quickly the detector responds to changes in temperature. The detector voltage signal for a 20 μm long bolometer and the VHF signal modulated at 100 Hz are recreated in Figure 22. (The frequency of the VHF signal is not depicted accurately for clarity.) The exponential rise and fall in the detector voltage is caused by the exponential increase and decrease in the bolometer resistance and hence the exponential increase and decrease in the bolometer temperature. Clearly, the modulation frequency should not be set so that the detector voltage does not reach it's steady state value. If the detector voltage is large, it can be read on an oscilloscope as the difference between the two steady state values (as in Figure 22). Using a lock-in amplifier to measure the detector voltage places further restriction on the modulation frequency. Typically, the lock-in amplifier measures the rms value of the detector signal. If the detector signal is a square wave, then the detector voltage is twice the reading of the lock-in amplifier. If, however, the exponential rise and fall is appreciable in the detector signal, the lock-in amplifier reading will be less than half of the detector voltage. This last situation must either be taken into account when calculating the detector voltage or avoided altogether.

Figure 23 shows the rolloff of the normalized detector voltage measured by a lock-in amplifier for several different length bolometers. From the plot, the longer bolometers exhibit a faster rolloff. The thermal decay time constant for a thermal detector can be calculated from
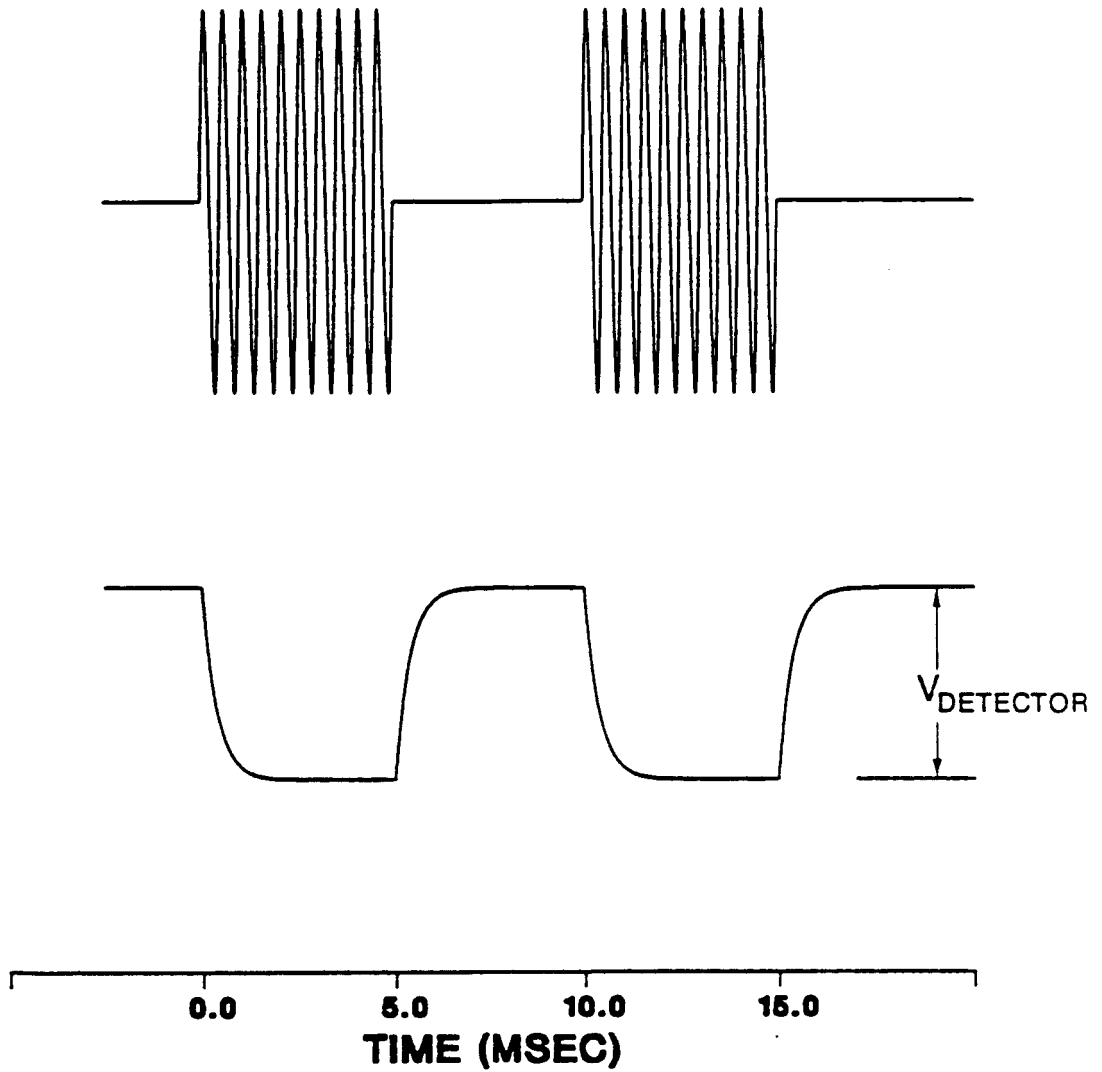
Figure 22. Detector Voltage for a 20 Micron Bolometer with 100 Hz
Modulation Frequency.

35

RESPONSIVITY VS MODULATION FREQUENCY
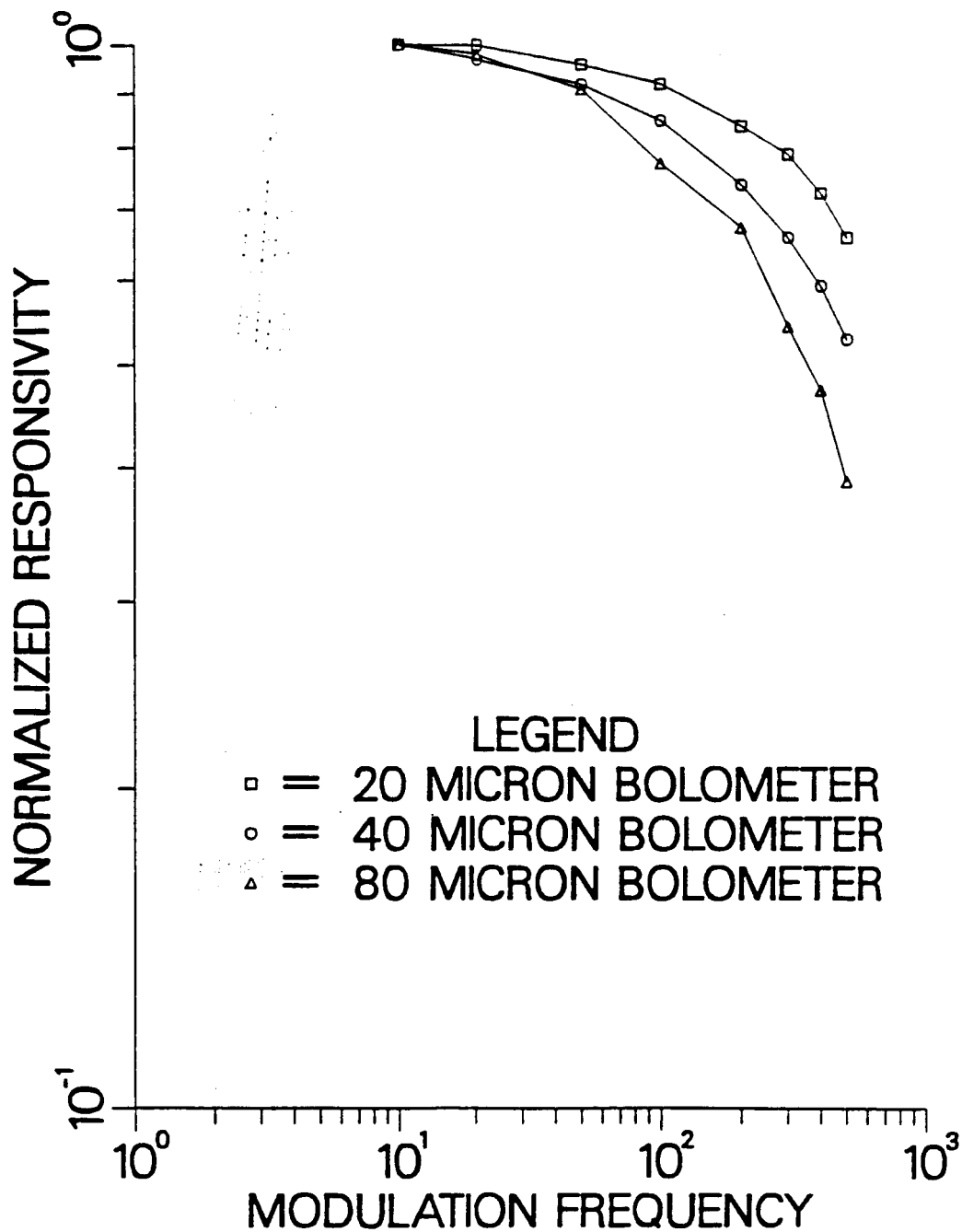
Figure 23. Roll-off of the Normalized Responsivity for the Different Length Bolometers.

$$\tau = \frac{1}{2\pi f^*}$$

where f^* is the frequency where the detector voltage rolls off to $2^{-1/2}$ of its dc value[5]. The thermal decay time constants for the various length bolometers have been calculated and are compiled in Table 6. The shorter bolometers have the smaller time constants because they have smaller thermal mass.

3.1.4 Noise Equivalent Power

The noise equivalent power (NEP) of the bolometers was calculated with the expression

$$NEP = V_{noise}/R \; ;$$

the noise voltage, V_{noise}, was measured with a PAR model 124 with model 116 preamp in the direct mode. The bolometer was biased at its operating point and the noise voltage was read with the chopping frequency set at 20 Hz. The 10% noise equivalent bandwidth filter was used in the measurement. The average value of the NEP was 5×10^{-9} watts $(Hz)^{-1/2}$.

3.2 Table Top Antenna Range

A table top antenna range was used for the antenna measurements. The basic arrangement of the measurement scheme is shown in Figure 24. A Varian 230 GHz extended interaction oscillator (EIO) was the source of the millimeter wave signal. The waveguide components included a dual arm directional coupler so that the power and frequency of the source could be monitored throughout the measurement. A phase lock loop circuit was built by Georgia Tech to frequency stabilize the EIO. The 28th harmonic of the local oscillator at 8.225 GHz was mixed with the source signal. A phase detection circuit provided the correction voltage to the body of the EIO.

One advantage of working at 230 GHz was that the far field

Bolometer Length (microns)	Thermal decay Time Constant (msec)
20	0.38
40	0.72
80	1.12

Table 6.   Thermal Decay Time Constants of the Different Length Bolometers.
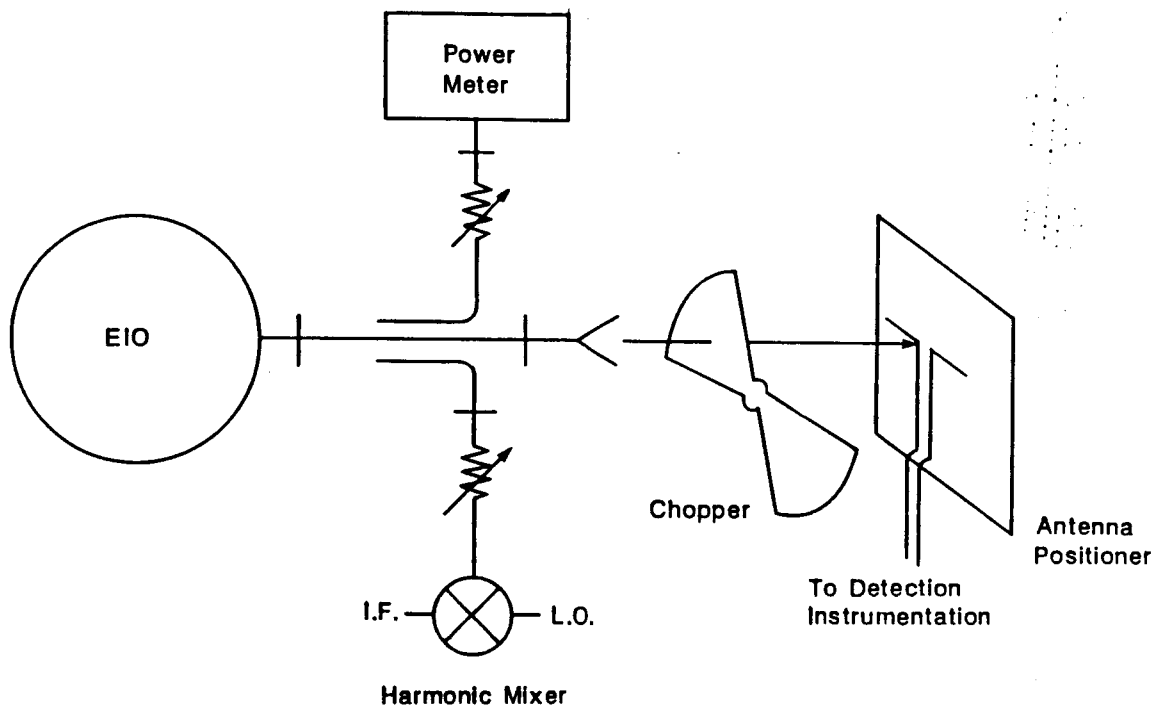
Figure 24. Layout of the Table Top Antenna Range.

of the source horn antenna was only 7 cm. This permitted all of the measurement apparatus to be placed on a single table top. An optics table was used so that all of the positioning equipment and waveguide components could be secured.

Two new pieces of apparatus to facilitate the antenna measurements were designed and built. One was a positioning instrument which allowed the rotation of the substrate in both the theta and phi directions (spherical coordinate system) without displacement of the antenna, as shown in Figure 25. The other instrument was a mount for the EIO which allowed changing the distance between the source and the antenna positioner without losing alignment of the incident field. Figures 26 and 27 are photographs of the antenna positioner. The first photo shows the three micrometer screws (1/4 - 40) used to place the antenna under test onto the axis of rotation of the theta positioner. The second photo shows the two translation stages used to move the desired antenna to the axis of rotation of the phi positioner. In the figures, the theta and phi rotation mounts have a black anodized coating. The phi rotation mount was set on a z-y translation stage to permit movement of the antenna and micropositioner with respect to the incident field.

The cylindrical mount for the EIO is shown in Figure 28. A square rail was used to keep the waveguide from the EIO in alignment with the antenna positioner as the distance between the source and substrate was adjusted. Both pieces of apparatus were mounted securely to the optics table.

The complete set-up is shown in Figure 29. The chopper does not touch the optics table so that vibrations are minimal. Note the absorber which is placed around the substrate to prevent reflections of the incident field.

The alignment of the antenna in the micropositioner was made with a spotting scope containing cross hairs which was set up approximately ten feet from the substrate. The micrometers and translation stages were adjusted until the antenna remained centered on the cross hairs under theta and phi rotations of the substrate.
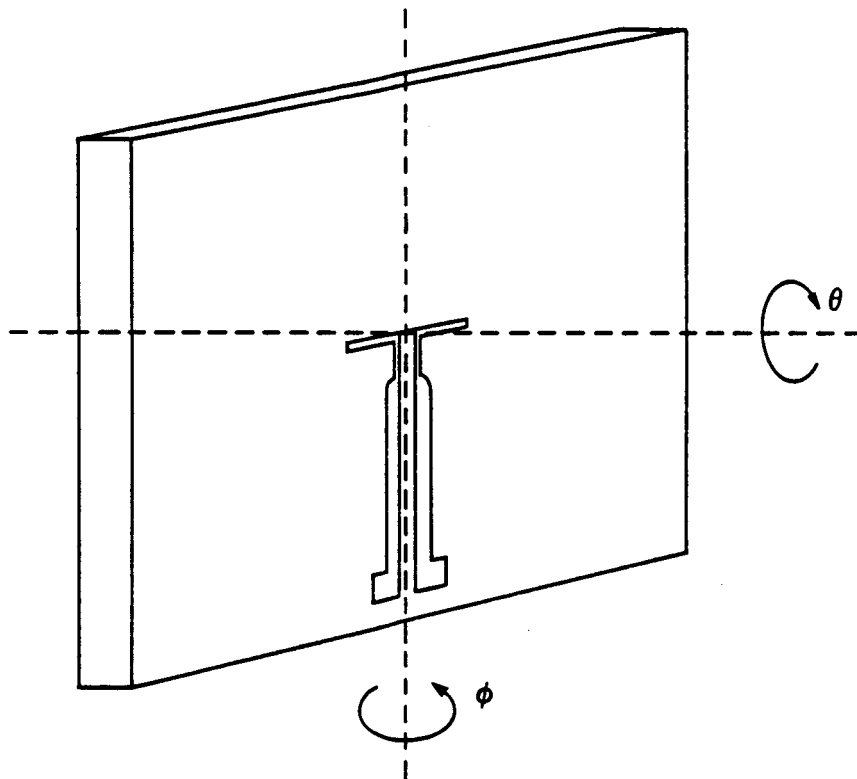
Figure 25. Illustration of the Theta and Phi Rotation Angles for the Antenna Measurements.

41
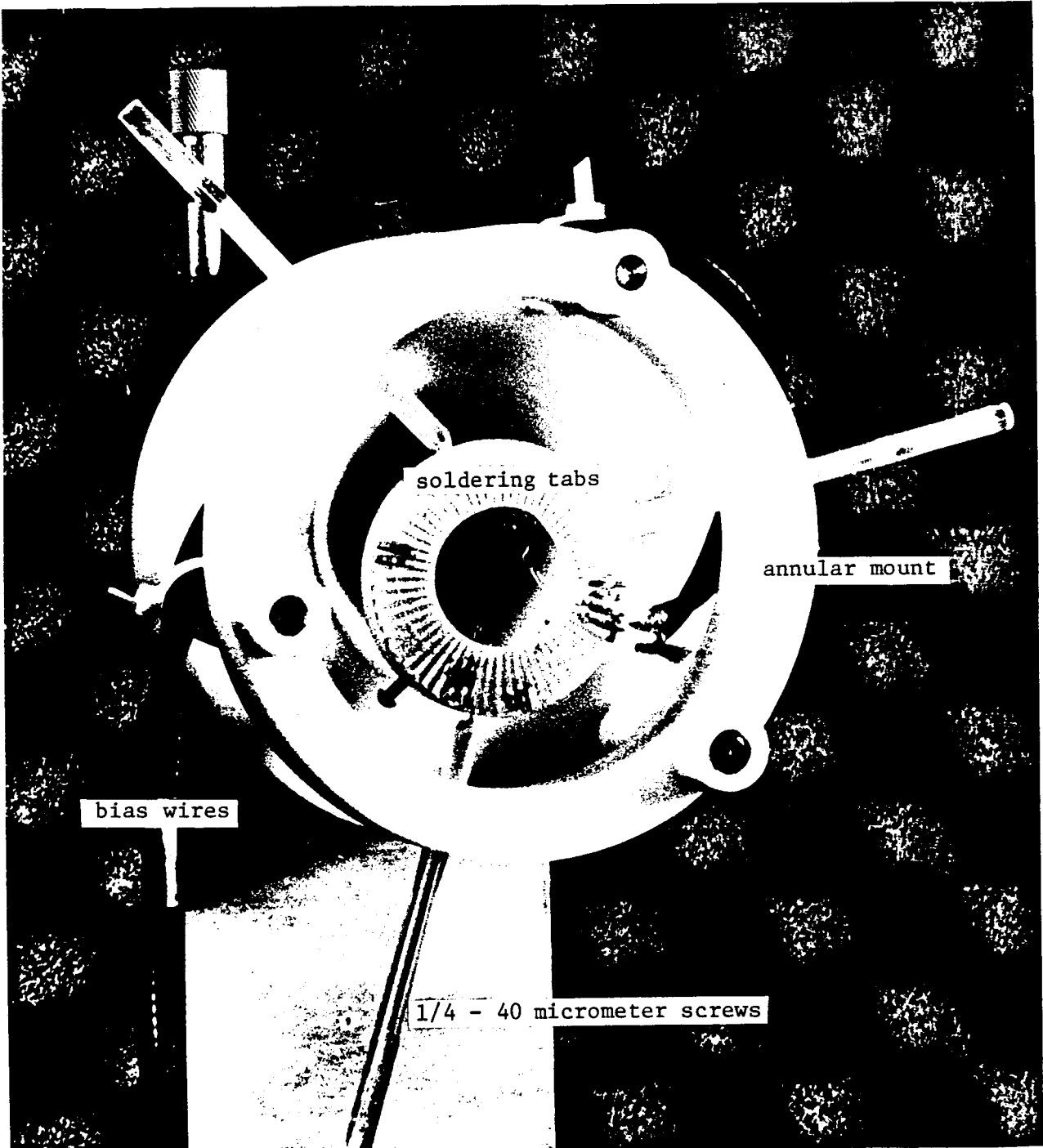
Figure 26. Photograph of positioner for the theta rotation alignment. The theta rotation device is the black mount in the rear.

theta positioner

annular mount

translation stages

phi positioner

Z-Y translation stage
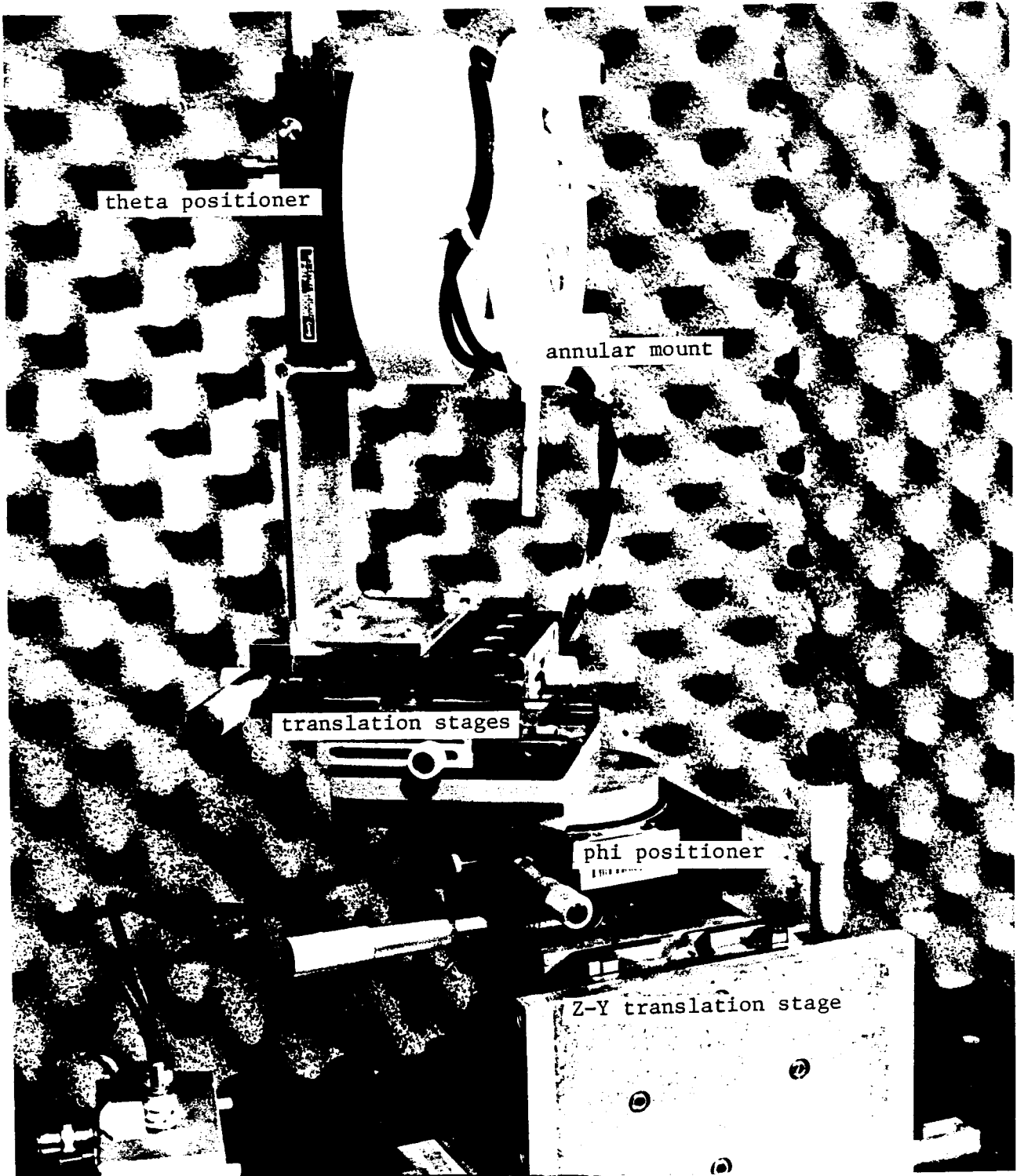
Figure 27. photograph of translation stages for phi rotation alignment. Again the black mount towards the bottom is the rotation device.
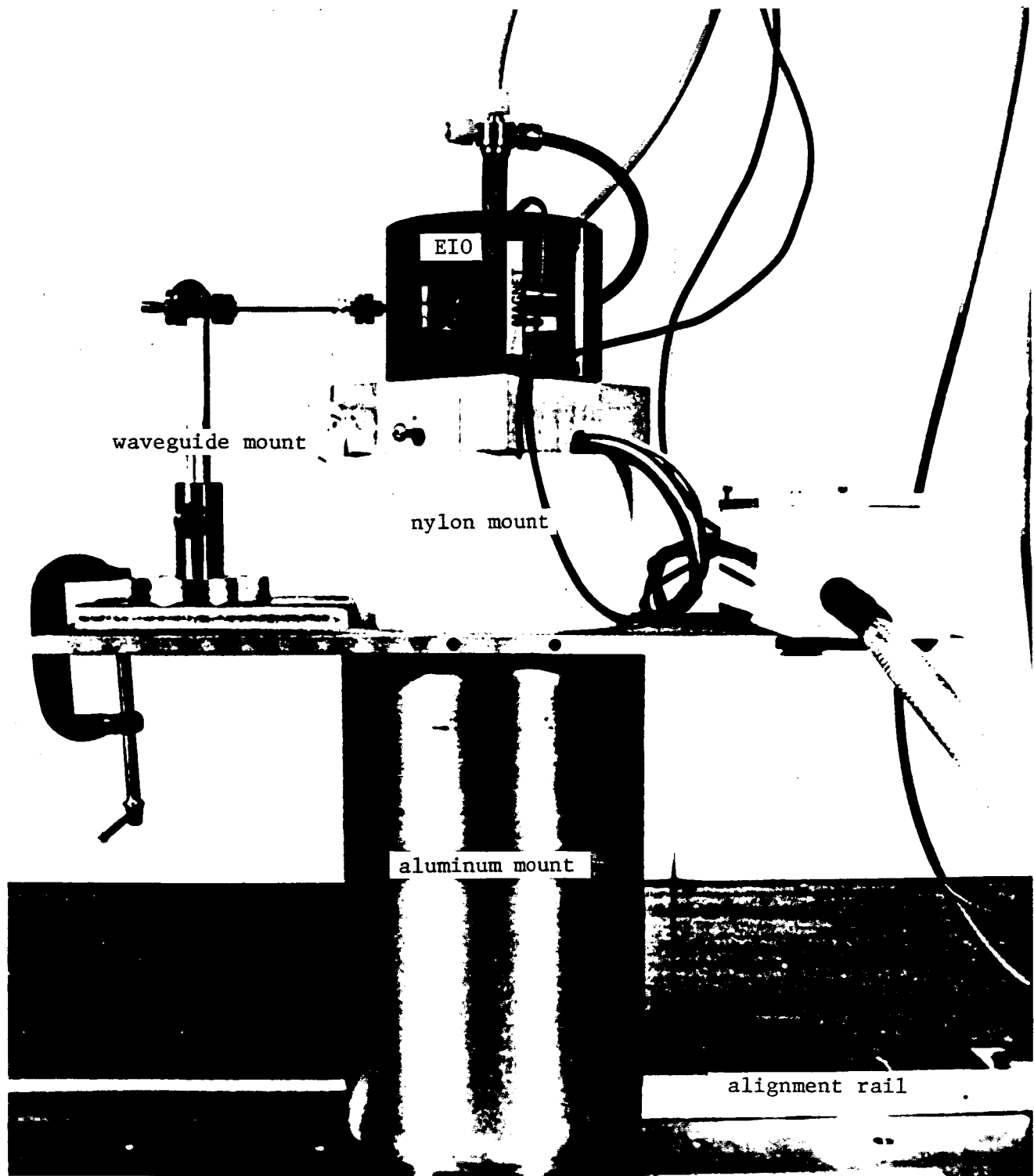
Figure 28. Photograph of cylindrical mount on a square rail for adjusting the distance between the source and substrate.
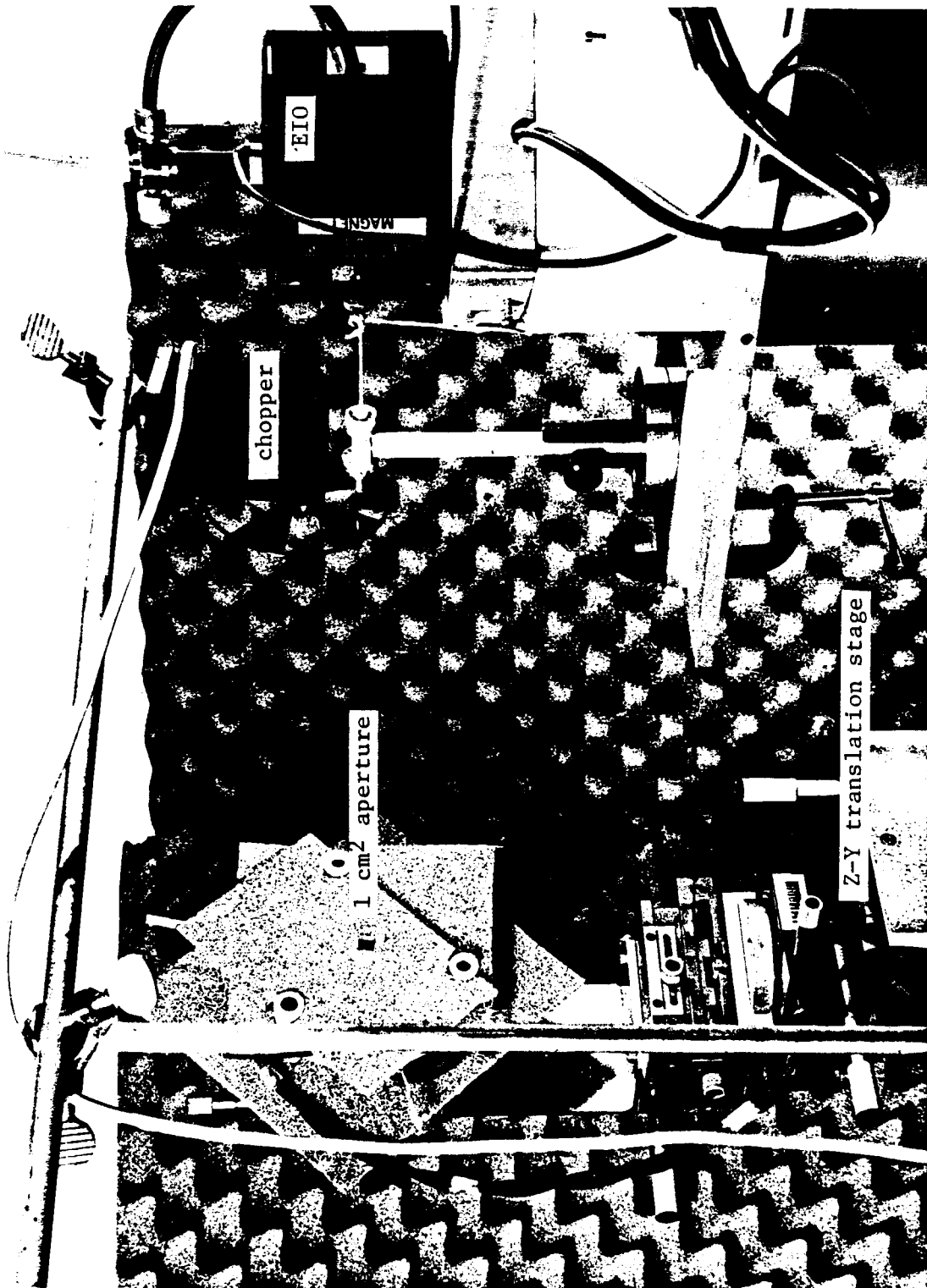
Figure 29. Photograph of complete set-up. Note the absorber around the substrate.

45

The electrical connections, bias circuit and detection scheme were the same as discussed in Section 3.1 (see Figure 19 - only the voltmeter across the bolometer was replaced by a lock-in amplifier). The bias circuit contained a mercury battery and precision resistors. Enough internal resistance was used in the biasing circuit to assure that a constant current was delivered to the bolometer while the antenna was under test. The biasing circuit and cables were shielded to prevent unwanted noise in the detection scheme.

The incoming radiation was mechanically chopped at 10 Hz. A lock-in amplifier (PAR 124 with model 116 preamp) was used to measure the detector voltage across the bolometer from the current induced in the antenna. This change in voltage was caused by a change in resistance brought about by I^2R heat dissipation of the induced currents in the antenna. The results from measurement of the antennas are given in Section 3.4.

3.3 Antenna Design

The antenna structure consisted of a half wave dipole antenna, a bolometer detector, a low pass filter, and low frequency leads to connect the detector to an external amplifier. A schematic of the structure is shown in Figure 30, and a photograph of one of the devices is shown in Figure 31. The dipole antenna, interdigitated capacitor, and low frequency leads were made from a 2000 Å film of chromium and gold. A thin adhesion layer of chromium, 200 Å, was deposited on the substrate first. The remainder of the film was gold. The horseshoe shaped bolometer, located at the terminals of the antenna, was made from a 2000-3000 Å film of bismuth.

3.3.1 Antenna Parameters

The antenna design parameters are from a recent publication of Kominami, et al.[16] The ratio of width to length of the antenna is assumed to be 0.02 and the antenna is taken to lie on a dielectric half-space, i.e. an infinitely thick substrate. The issue of substrates with finite thicknesses greater than several
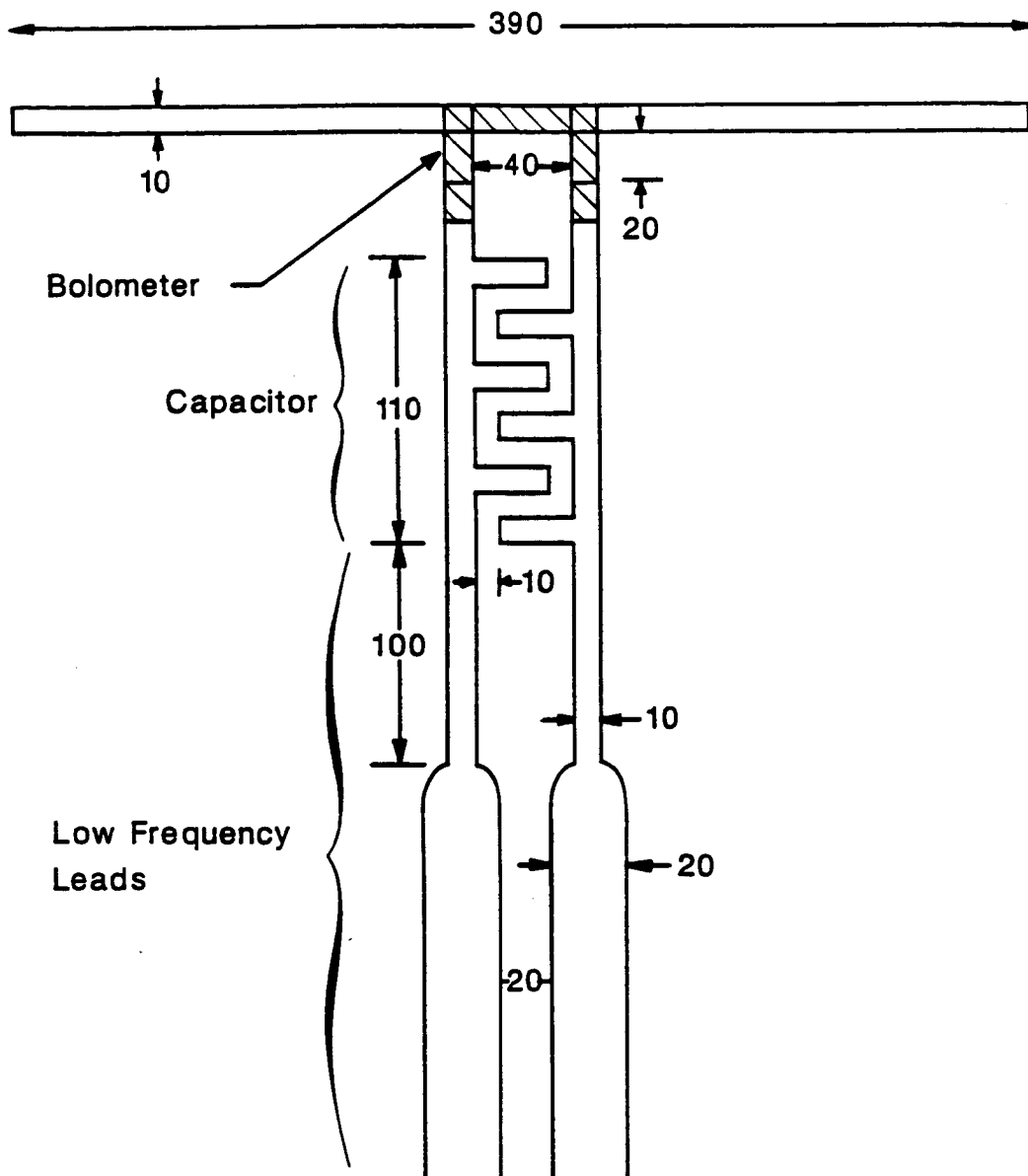
Figure 30. Dimensioned Layout of the Antenna Design.

47
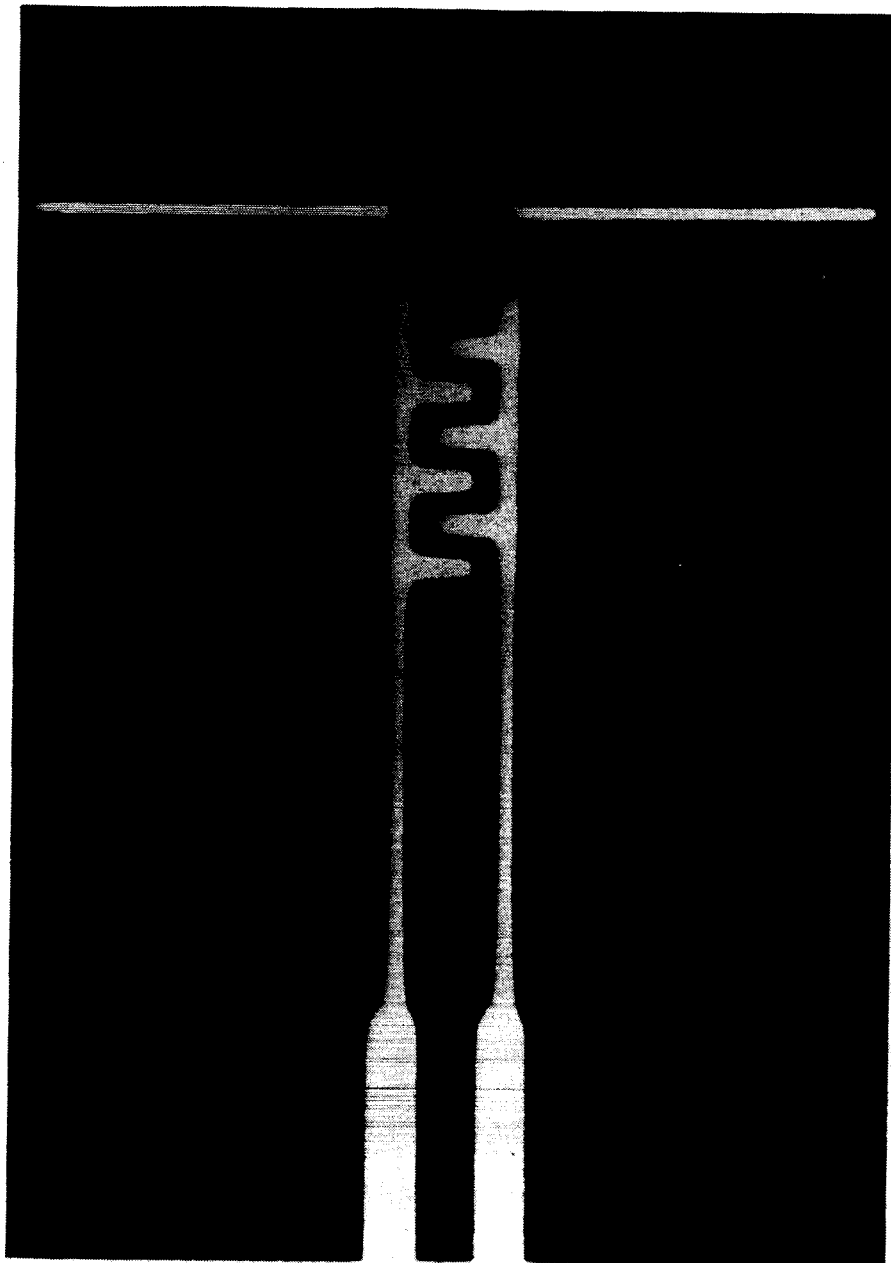
Figure 31. Photograph of the Antenna Structure.

wavelengths has not been addressed in this or other work in the literature. The design parameters in reference 16 were used for the finite substrate without modification.

A resonant length of an antenna is, by definition, any given length which makes the radiation resistance of the dipole purely real and finite. For an antenna on a substrate, both the resonant length and corresponding resonant resistance are a function of the dielectric constant. The values for an antenna on a dielectric half-space are between the values for a free space antenna and those for a dipole embedded in the dielectric. The resonant length is given to a good approximation by

$$\frac{L}{\lambda_0} = \frac{1}{\sqrt{\epsilon_e}} \; 0.48 \frac{1}{1 + W/L}$$

where $\epsilon_e = (1 + \epsilon_r)/2$ and W/L is the width-to-length ratio of the dipole. The corresponding resonant resistance is found from plots given in reference 16. For a relative dielectric constant of 4, the resonant length is 0.3 λ_0 (390 μm for λ_0 = 1.3mm) and the resonant resistance is 55Ω.

3.3.2 Transmission Line and Bolometer

The impedance of the antenna and that of the load (either the bolometer or the rectifying diode) must be matched in order for the antenna to deliver all received power to the load. If the resistance of the bolometer is taken to be purely real, i.e. no parasitic capacitance in the Au-Bi junction is assumed, a transmission line to match the antenna and the load is not required. A bolometer with resistance equal to the resonant resistance of the antenna is placed at the terminals of the antenna for maximum power transfer. If, however, the load is a rectifying diode, there is limited freedom associated with the impedance of the device. A matching transmission line must then be used to optimize the rectified current.

49

3.3.3 Low Pass Filter

Introduction of a low pass filter prevents the current induced in the low frequency leads from flowing through the bolometer. As shown in Figure 32a, a capacitor and resistors in the leads can be placed adjacent to the bolometer. This configuration allows the current induced in the leads to flow through the capacitor and the current in the antenna to flow through the bolometer. The value of the resistor between the bolometer and capacitor must be large enough to prevent the current in the antenna from flowing through the capacitor. The addition of the resistors in the low frequency leads, however, unnecessarily complicates the fabrication process.

Another possible low pass filter, shown in Figure 32b, can be made without the blocking resistors by altering the design of the bolometer. The horseshoe-shaped bolometer is actually two bolometers in parallel between the terminals of the antenna. The resistance of each bolometer is twice the resonant resistance so that the parallel combination provides the matched condition. A straightforward calculation shows that the sensitivity of the bolometer for a given current flow in the antenna is the same for either configuration.

For antennas at 230GHz, the resonant resistance is 55Ω. The series resistance of the horseshoe bolometer seen from the end of the low frequency leads is 220Ω. If the reactance of the capacitor is desired to be a factor of ten less than the series resistance of the bolometer, the value of the capacitor should be 0.2 pF, or greater. With this capacitance only one tenth or less of the current induced in the transmission line will pass through the bolometer.

The design parameters for the capacitor are from Alley.[17] The finger widths and spacings are 10 μm and the length of each finger is 30 μm, as shown in Figure 30. The total length of the capacitor is kept small (110 μm) compared with the wavelength so that phase variation along the capacitor is not a problem. Without including the contribution of the ends of the fingers with the opposite lead, the capacitance is calculated to be 0.2

a)

b)
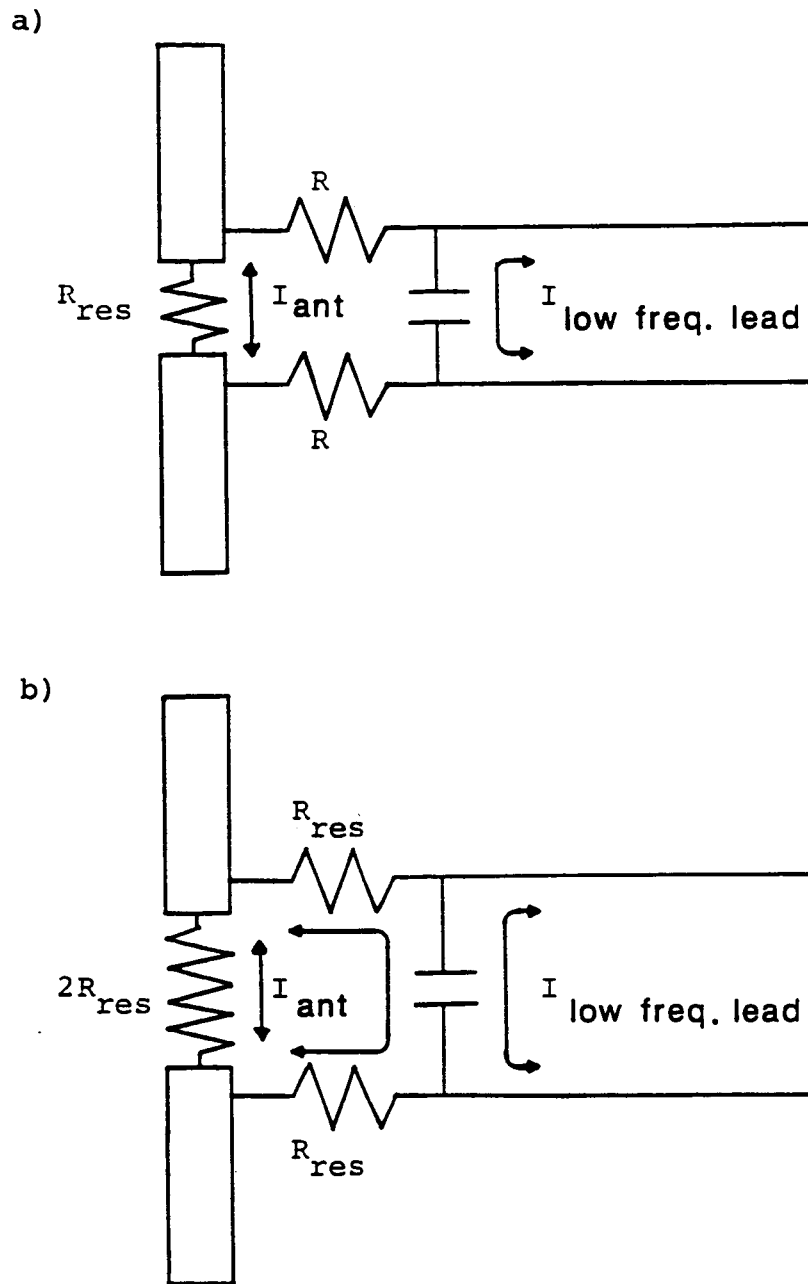
Figure 32. Two possible configurations for the low pass filter. In 32a the values of R and C are chosen so that current induced in the antenna flows through the bolometer and current in the bonding wires flows through the capacitor. In 32b the current in the bonding wires is still shorted through the capacitor, but the current in the antenna flows through two bolometers in parallel.

pF. The low frequency lead is run to the edge of the substrate where bonding wires connect them to the soldering tabs discussed in Section 3.2 (see Figure 26).

3.4 Antenna Patterns

Considerable effort was spent making the field pattern measurements for the substrate mounted antennas. This task was difficult for several reasons. First, the small size of the antenna made the alignment and positioning of the dipole a tedious procedure. Next, the millimeter wave components and instrumentation for these frequencies are sensitive to the connections between the waveguide components, to rough handling and to dust and oils in the environment. In general, much care had to be used while working with this equipment. The greatest experimental difficulty was the stray scattering of the incident field. Reflections from the bonding wires, edges of the substrate and nearby metal structures distorted the field patterns. The last problem was in trying to decide when we had eliminated the experimental difficulties and that we had measured the actual antenna pattern. The difficulties listed above can be repeatable from measurement to measurement. We have found only one other report of measurement of a resonant dipole on a finite thickness substrate.[18] In this work, no conclusive antenna patterns are given; they only report on the problems they encountered in the measurement.

Antennas were measured on two different type substrates. The first type was a circular disc, 1.5 inches in diameter and 0.125 inches thick, made from Corning fused silica. The second type was a Fisher Brand #2 glass cover slip, 25 mm square and 0.15 to 0.25 mm thick. These were chosen to observe the effect of substrate thickness on the antenna pattern.

The bolometer measures the power received by the antenna, so all of the measurements reported in this section will be for antenna power or E^2. We start by calculating the value of E^2 on the incident and transmitted side of a dielectric slab in free space for an incident field at an arbitrary angle from normal to

Incident Side

Transmitted Side

θ

ϵ_{slab}
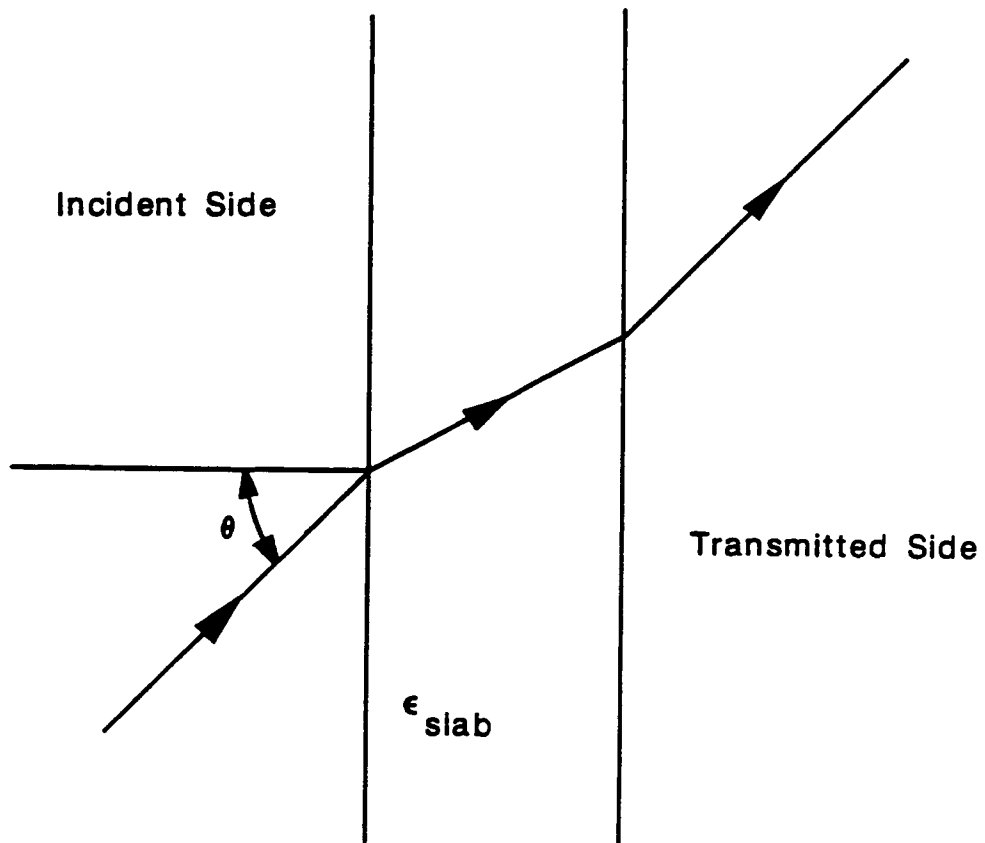
Figure 33. Geometry for Calculating E^2 on the Incident and
Transmitted Side of a Dielectric Slab.

53

the dielectric slab. This is shown more clearly in Figure 33.
The field equations for this problem are worked out in Born and
Wolf.[19] The values of E^2 for our two substrates are given in
Figures 34 and 35. In quadrants 2 and 3 of the polar plots, the
TM case is considered and the TE results are given in quadrants 1
and 4.

Two antenna patterns were measured: these were the
polarization mismatch factor and the great circle arc or E-plane.
This last pattern corresponds to the TM polarization given in the
power plots. The polarization mismatch factor is proportional to
$\cos^2\theta$ and, hence, the power pattern should be a figure 8 shape.
The patterns that we measured, however, were not symmetric.
Either one lobe was larger than the other, as in Figure 36, or
both lobes were pinched to one side, as in Figure 37.

The measured great circle cut was also distorted. Suppose
the dielectric substrate only altered the incident field
presented to the antenna (as in Figures 34 and 35 above) and did
not effect the pick-up of the antenna. We would then expect the
measured antenna plot to be the product of incident field
strength at the surface of substrate and the well known pattern
for a free space half-wave dipole. These plots are given in
Figures 38 and 39. The patterns that we have measured are
shown in Figures 40 and 41. Again, the patterns are distorted in
a non-symmetric fashion which would suggest that there is still
some scattering or nonuniformity in the incident field. Beyond
the non-symmetry, however, there seems to be some effect that may
be due to the substrate. The multi-lobed pattern is seen for
both the thick and thin substrates; however, the general shape of
the plot is consistent with the power plots in Figures 38 and 39.

A similar multi-lobed pattern was observed in the work of
Reference 18 mentioned above. Here, the measurements were
conducted at 10 GHz, and their results are shown in Figure 42.

To sum up the measurement efforts, we feel that the patterns
measured so far are close to the actual antenna patterns. There
are probably still one or two experimental difficulties yet to
find, but it is difficult to tell the strength of the interaction
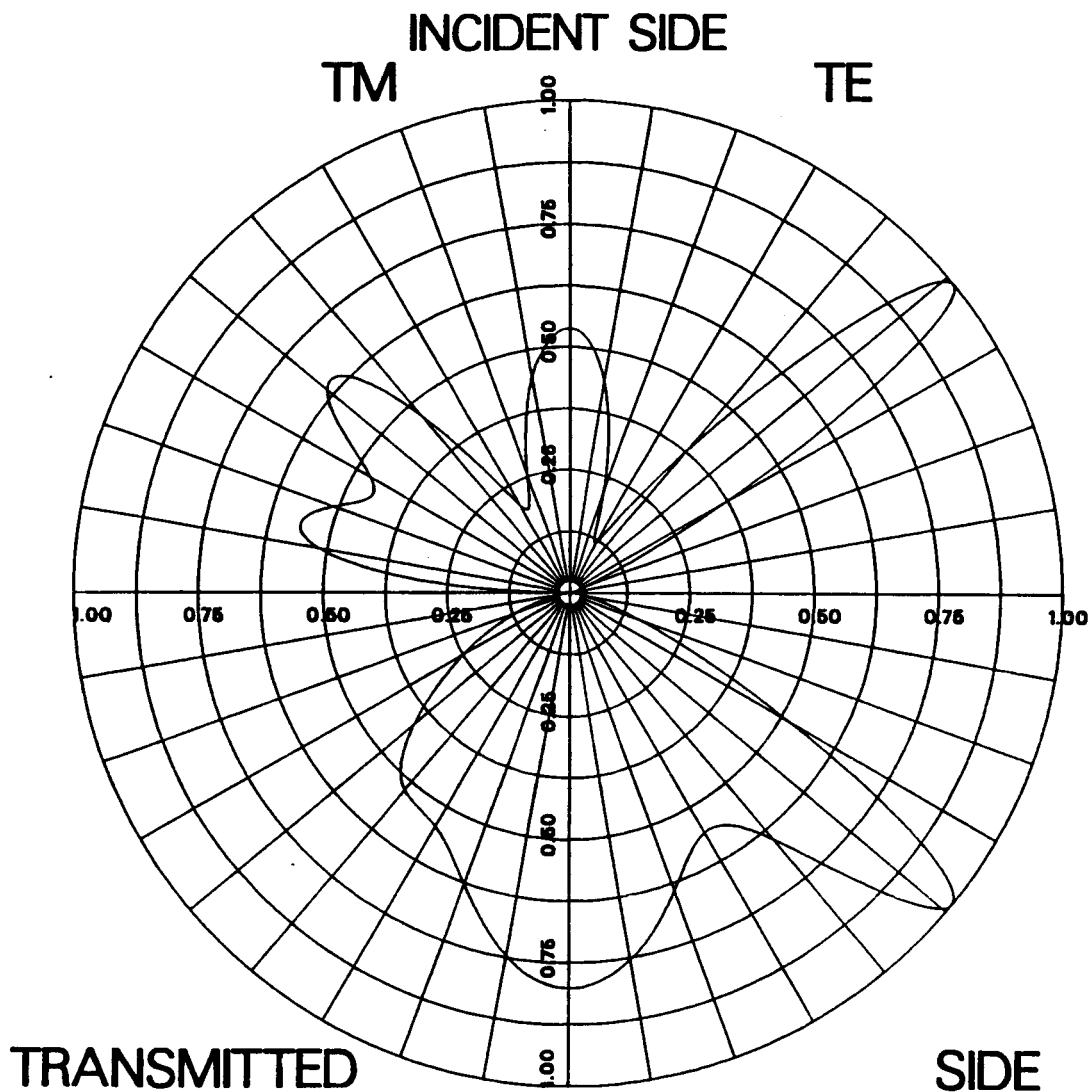
Figure 34. Polar Plot of E^2 on the Incident and Transmitted Sides of a 4.88λ Thick Substrate.
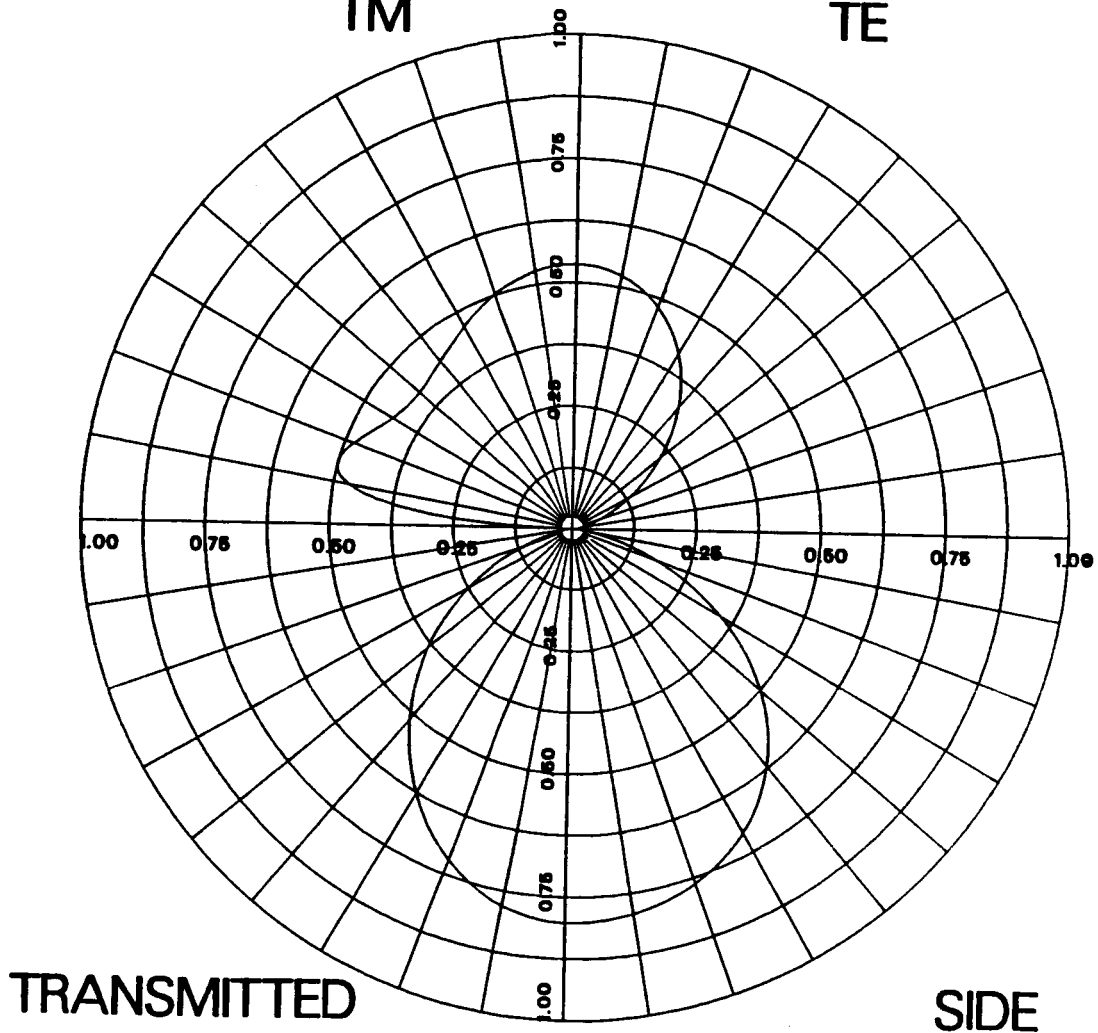
Figure 35.   Polar Plot of E^2 on the Incident and Transmitted
Sides of a 0.38λ Thick Substrate.
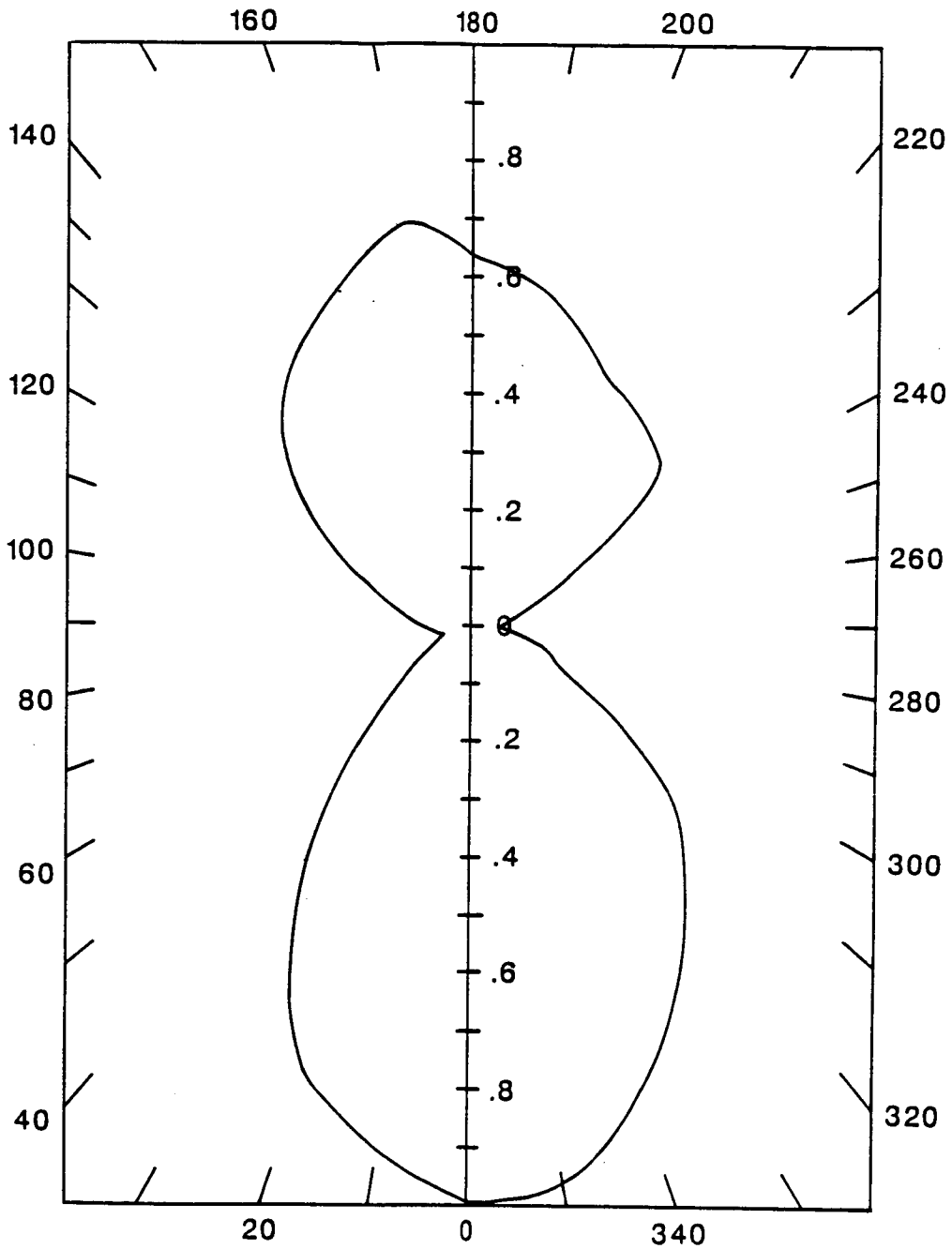
Figure 36. Example I of the Distortion of the Measured
Polarization Mismatch Factor.
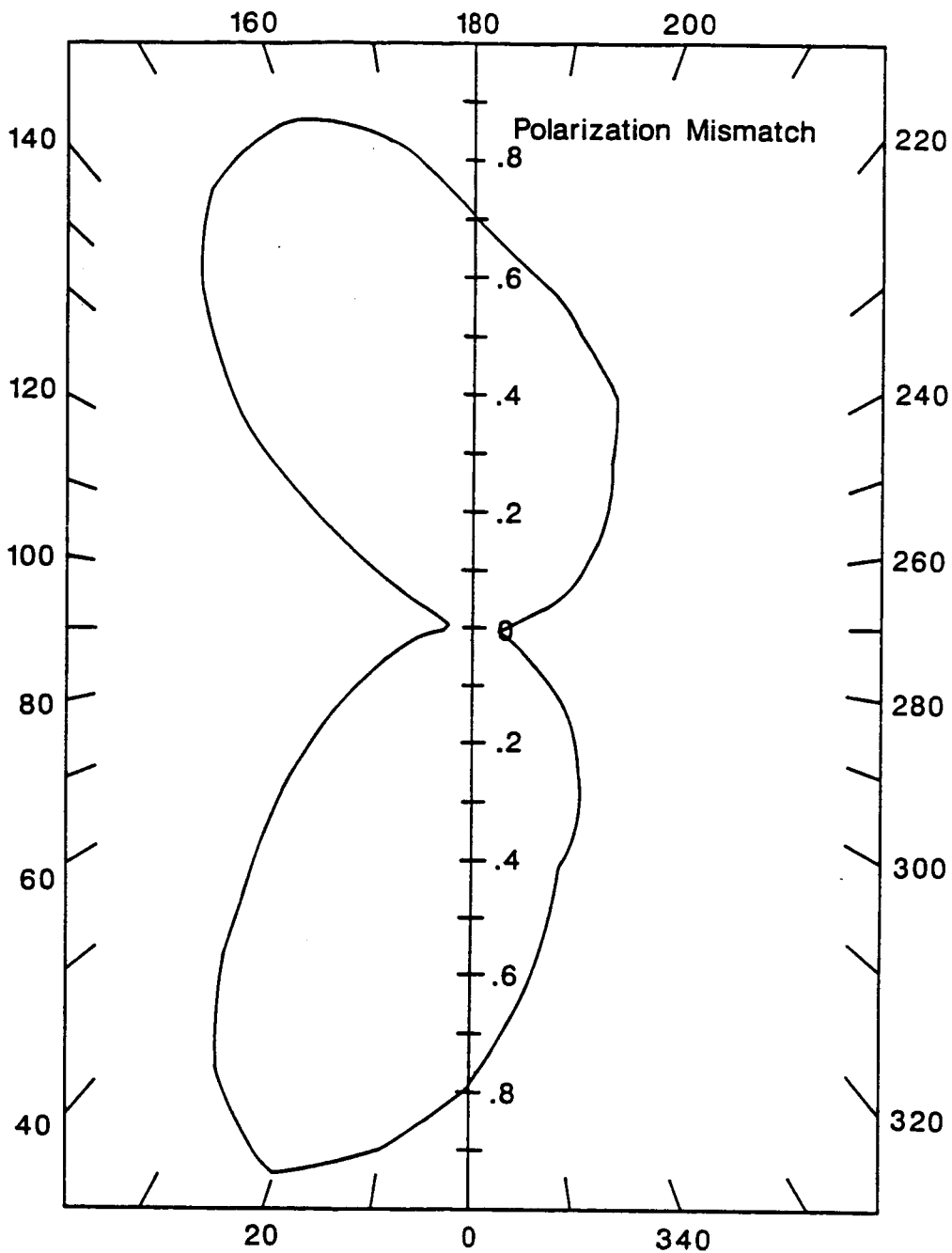
Figure 37.   Example 2 of the Distortion of the Measured
              Polarization Mismatch Factor.

POWER PATTERN FOR A DIPOLE ON A 3.175MM SLAB
INCIDENT SIDE
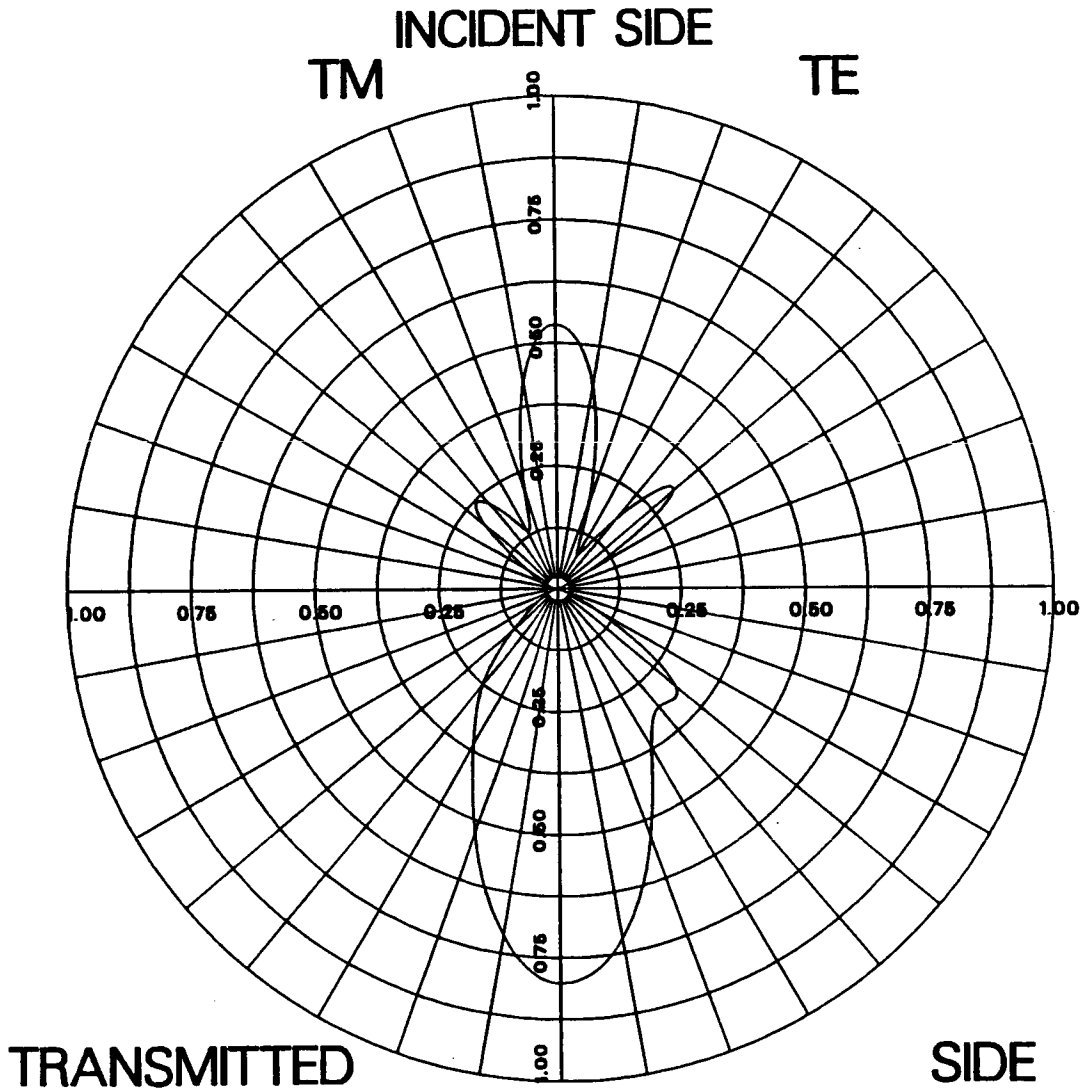
Figure 38.   Power Plot of the Product of E on the Surface of the
Substrate and the Free Space Half-wave Dipole Pattern
for a 4.88λ Thick Substrate.

POWER PATTERN FOR A DIPOLE ON A 0.25MM SLAB

INCIDENT SIDE

TM   TE

TRANSMITTED   SIDE
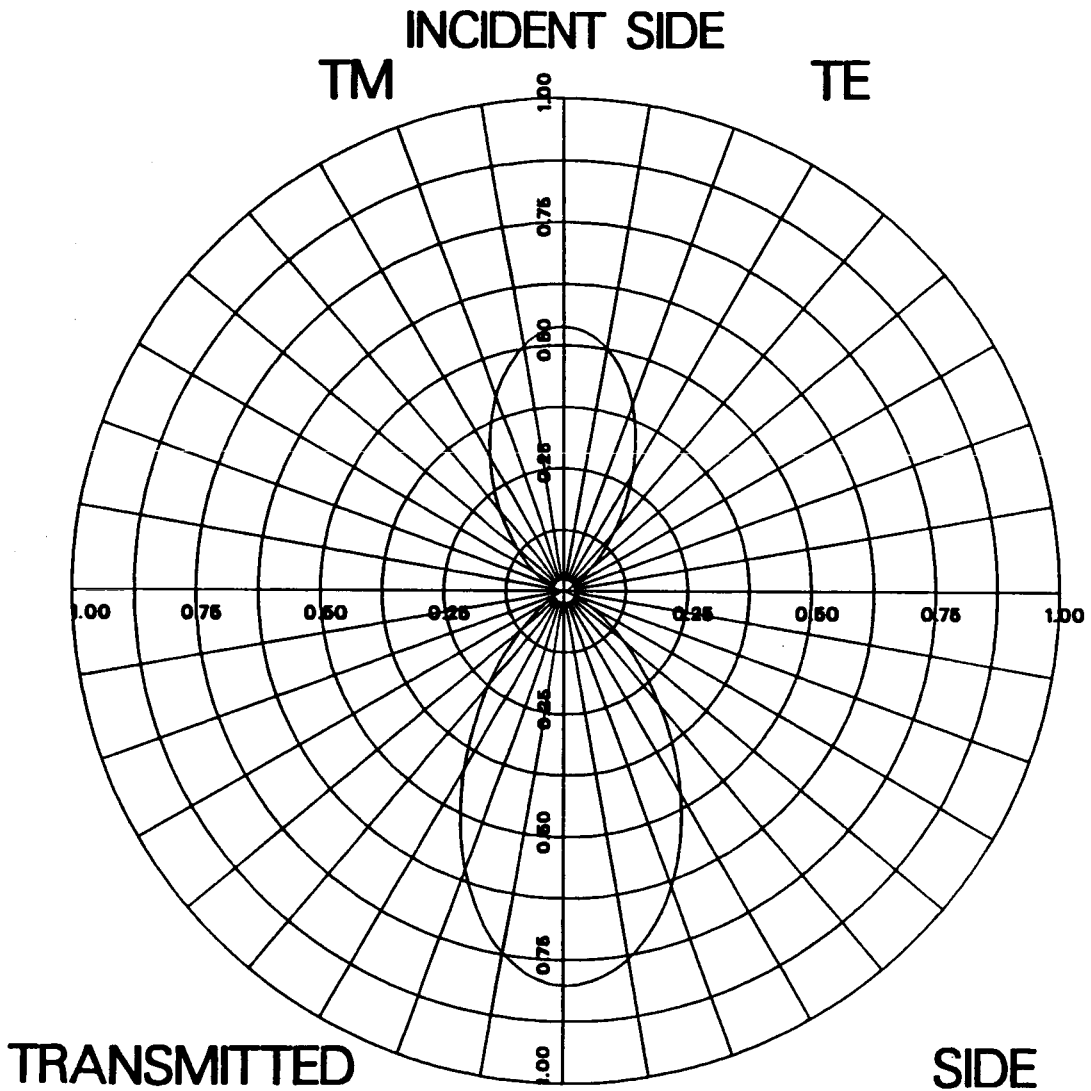
Figure 39.   Power Plot of the Product of E on the Surface of the Substrate and the Free Space Half-wave Dipole Pattern for a 0.38λ Thick Substrate.
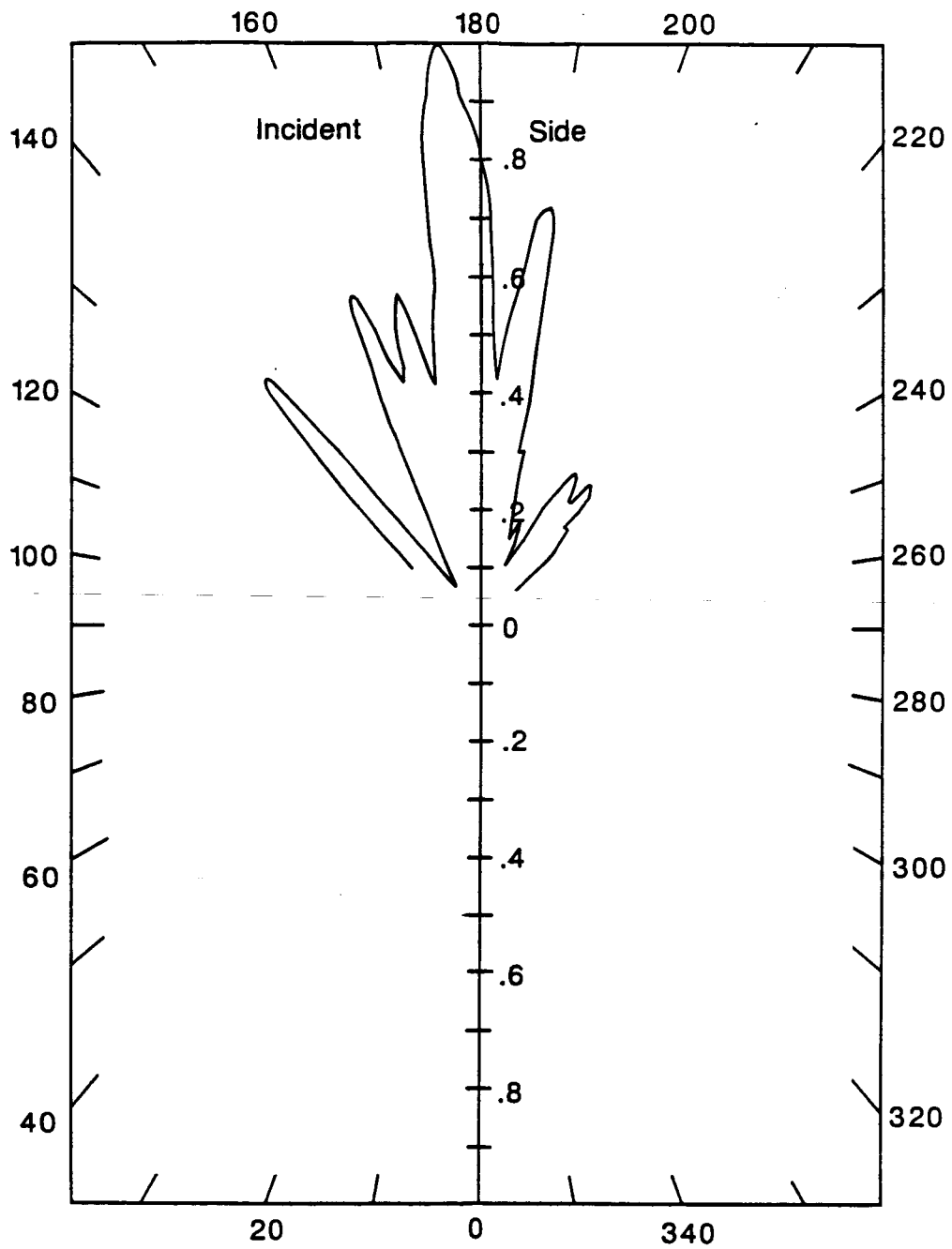
Figure 40. Measured Power Plot for a Half-wave Dipole on a 4.88
λ Thick Substrate.
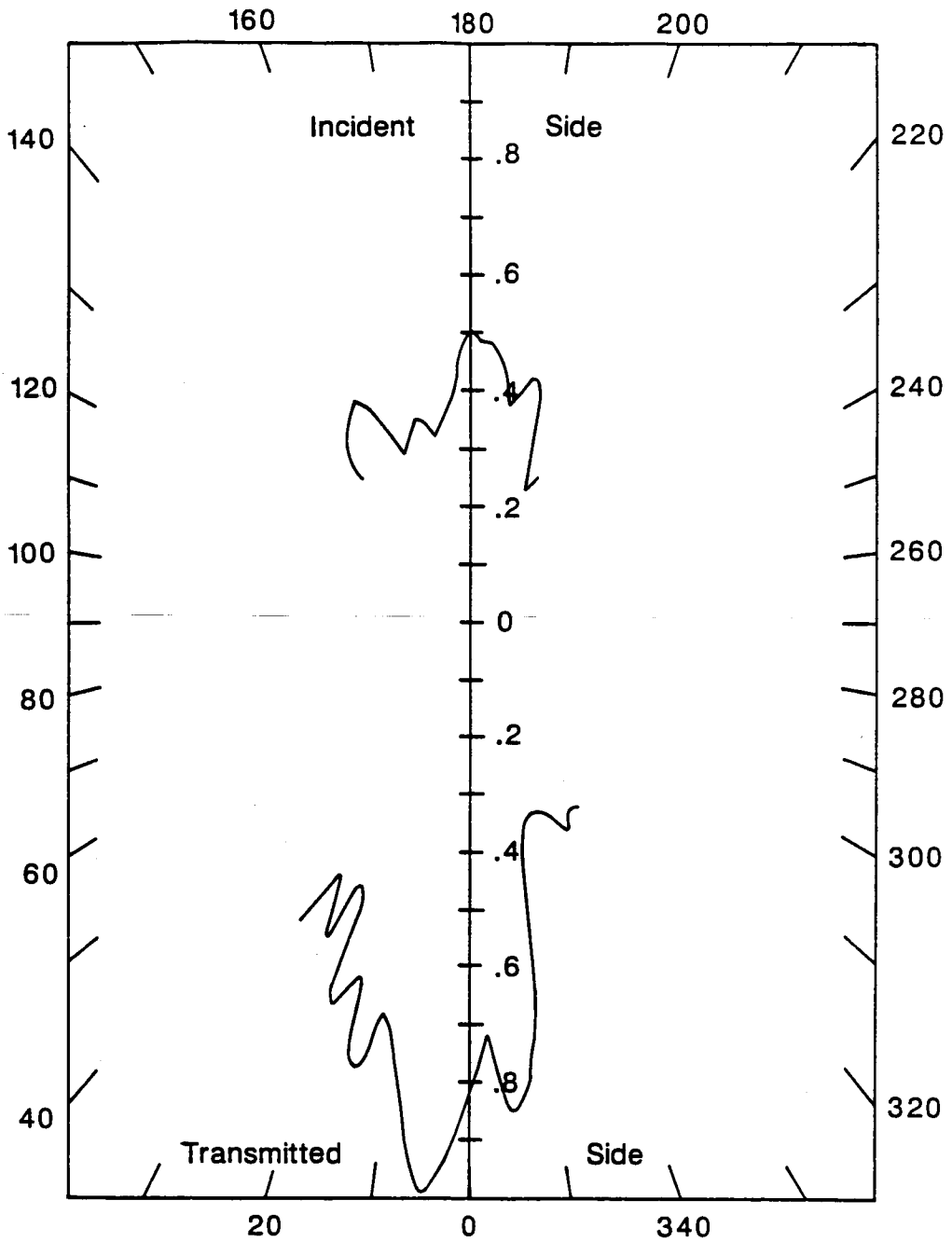
Figure 41. Measured Power Plot for a Half-wave Dipole on a 0.38 λ Thick Substrate.
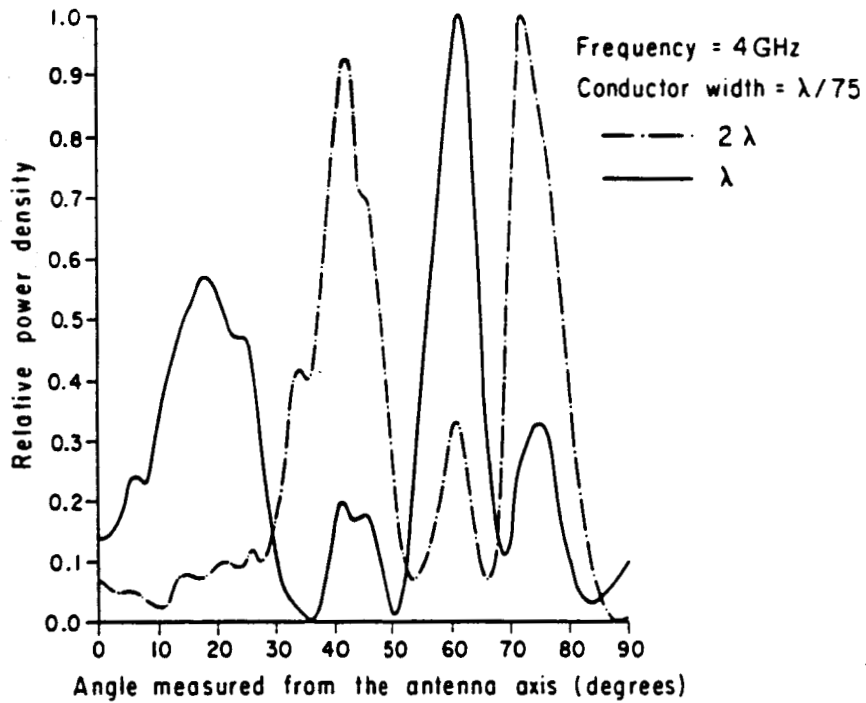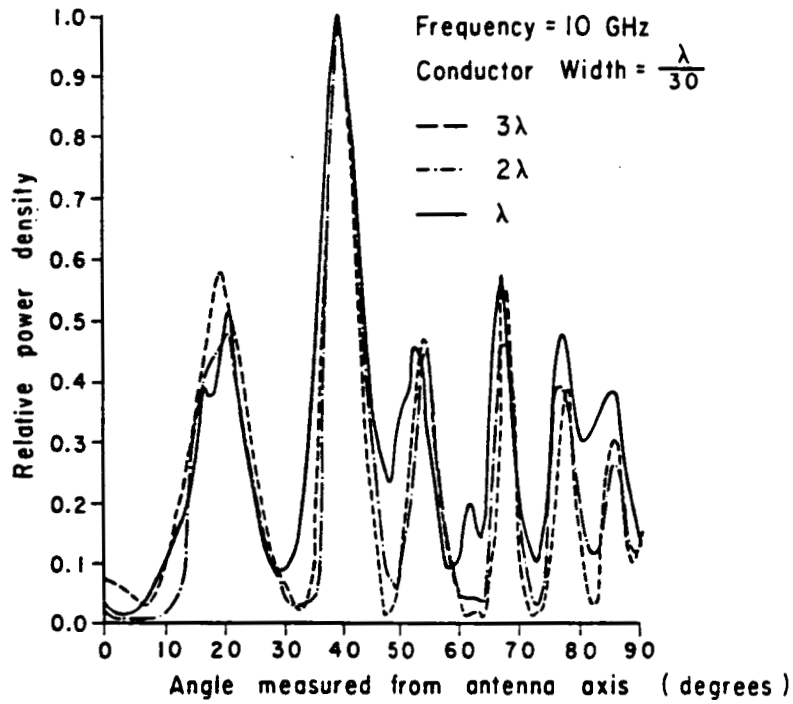
Figure 42. Measured Great Circle Cut for Resonant Dipole Antennas on Finite Thickness Substrates. From Reference 18.

between the antenna and substrate, such as surface waves, that may be distorting the pattern. Adding the low pass filter in the antenna structure was an important step in enabling the antenna measurements. We have checked the performance of the filter by making a structure with the low pass filter and low frequency leads, but without the dipole antenna. This modified configuration did not show any detector voltage (above the noise floor) when it was placed in the incident field. Thus, we feel confident that the patterns that we are seeing are from the dipole and not from pick-up on the low frequency leads.

We have used the results obtained so far to calculate the antenna gain and effective area. It should be made clear that these are preliminary calculations only; the measured gain may change when the antenna measurements are refined. The antenna design was based on a substrate relative dielectric constant of 4, so only the measurement on the fused silica will be given. In our measurements, only a moderate difference - 20 to 30% - in the received power was observed for the antenna on the incident side or the transmitted side of the substrate. Since we do not believe the measured gain to be more accurate than this, only one value of gain will be given. We measure the gain of the antenna to be 2.24 dB, which is about the same as a free space half-wave dipole. This means that the effective area is roughly the same as the free space dipole or ~0.1 λ^2. We are continuing the antenna measurements and the final results, when the experiment is completed, will be published in the open literature.

4. METAL-OXIDE-METAL DIODES

The two principal factors affecting the efficiency of a rectenna system are the power collection by the antenna and its rectification into dc power. In the millimeter region, both of these mechanisms can be separated and optimized independently by the correct choice of antenna design and the fabrication of high-speed semiconductor diodes. The extension of this concept to higher frequencies, corresponding to infrared radiation, requires

very small (micron sized) antennas and sub-micron sized rectifiers, making necessary an integrated structure. In this section, the factors affecting the performance of the rectifier are discussed. Despite the progress made in the development of semiconductor devices, and the recent interest in high-speed devices, the response times of junction-type diodes are still well below the 10^{-13} - 10^{-14}s range required for the rectification of infrared radiation.[20] Several new concepts promise to change this situation in the future, but, at present, the metal-insulator-metal device offers the only effective choice.

4.1 Theoretical Considerations

For efficient power output the response time of the rectifier must equal or exceed the reciprocal of the frequency of the incident radiation, and its impedance must match the antenna to optimize the power transfer between the two devices. Typically, the response time is limited by either the transit time of carriers between the two electrodes of the device, or the RC-product. Both factors are determined by the device geometry, i.e. its thickness and area, and the energy band diagram of the device which determines its current-voltage properties. The I-V characteristics also determine the rectification properties of the diode and the power density that can be conducted through the device.

As shown in Figure 43, the metal-oxide-metal (MOM) tunnel diode is a very thin film device in which electrons from one metal layer can tunnel through the insulator film and be collected by the second metal layer. The transit time of electrons across the insulator is determined by the velocity of the electron wave-packet in the insulator and the thickness of the film. Assuming a typical value of 10^7 cm/s for the electron drive velocity, insulator thicknesses of 10 and 100Å are calculated for transit times of 10^{-14} and 10^{-13}s, respectively. Thus, very thin structures are required for power conversion at wavelengths between 10 and 100 μm. The thickness of the

(a) SYMMETRICAL MOM **(b) ASYMMETRICAL MOM**
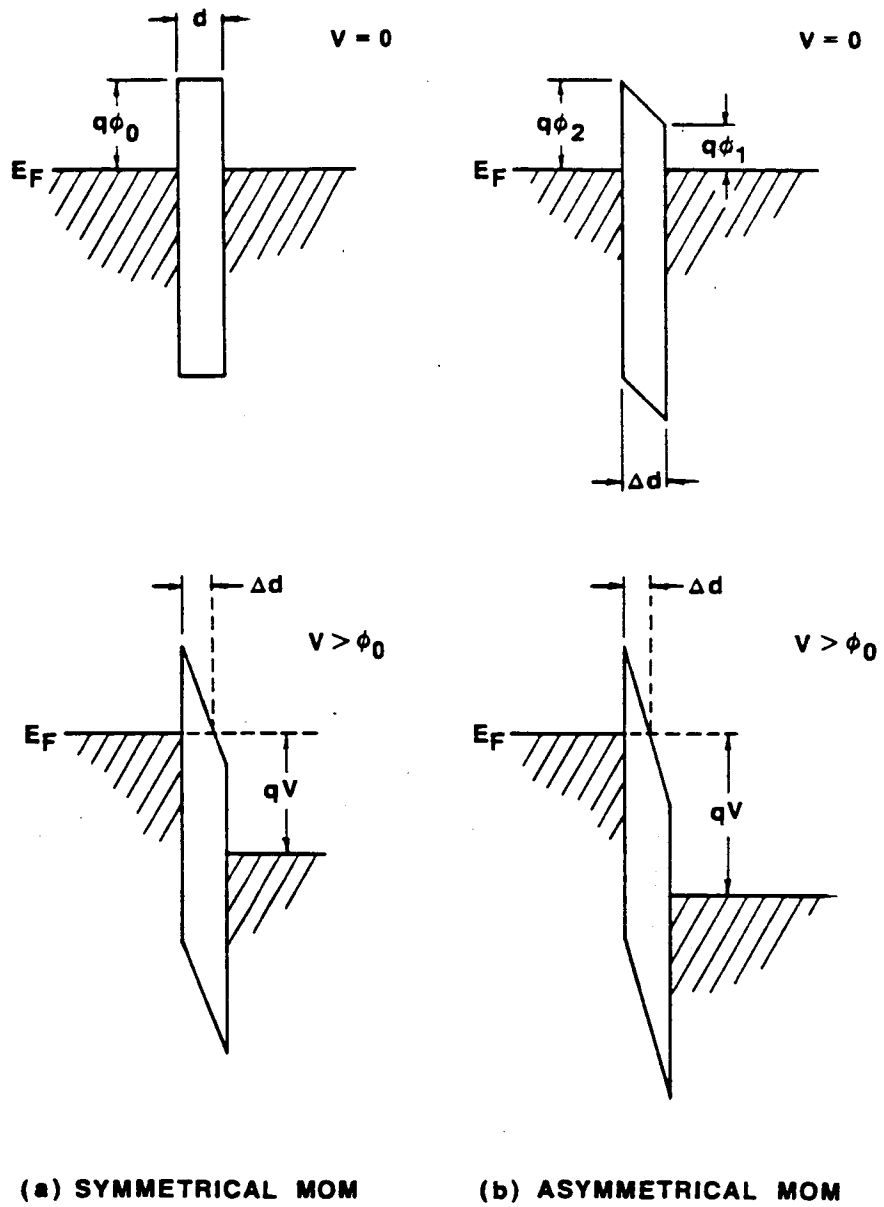
Figure 43. Possible MOM Device Structures.

66

insulator also limits many other properties of the diode, particularly its capacitance and load factor. The diode capacitance, C, for the thinnest structure is thus

$$c = \frac{\epsilon A}{10 \times 10^{-8}} = 2.2 \times 10^{-6} \, F/cm^2$$

where it is assumed that the dielectric constant, ϵ, of the oxide equals 2.5.

An estimate of the impedance of the device can be obtained from its electrical properties. Extensive calculations of the current-voltage characteristics of ideal MIM structures have been performed by Simmons [21] who shows that they are very strongly dependent on the oxide thickness, the built-in potentials, and the applied voltage. As shown by Figures 44 and 45, the resistance-area product of the devices increases very rapidly with oxide thickness, and near zero bias conditions increases orders of magnitude, from 10^2 to $10^{12} \, \Omega - cm^2$ as the oxide thickness is doubled from 20 to 40 Å. For bias voltages greater than the built-in potential, the resistance decreases very rapidly; again, the changes are by many orders of magnitude and are sufficient for the device to become highly conductive in the direction of the applied voltage. Using this information, a calculation of the RC-product shows that, in fact, the response time of an actual MOM structure is very slow. However, because these devices are connected in parallel with the antenna, it can be shown from the equivalent circuit of the structure, that it is the radiation resistance, R_r, of the antenna, which determines the total resistance of the rectenna. For a T-type antenna, R_r = 75 ohm (approximately), and the RC-product equals $1.65 \times 10^{-4}A$ where A is the area of the diode. Thus, to obtain RC-products in the $10^{-14} - 10^{-13}$ sec. range, A must be equal or less than 10^{-10} cm^2. This condition limits the size of the MOM device to approximately a 0.1 micron square. Ignoring, for the moment, the fabrication details of these devices, it is first necessary to determine if this element size can accommodate the power
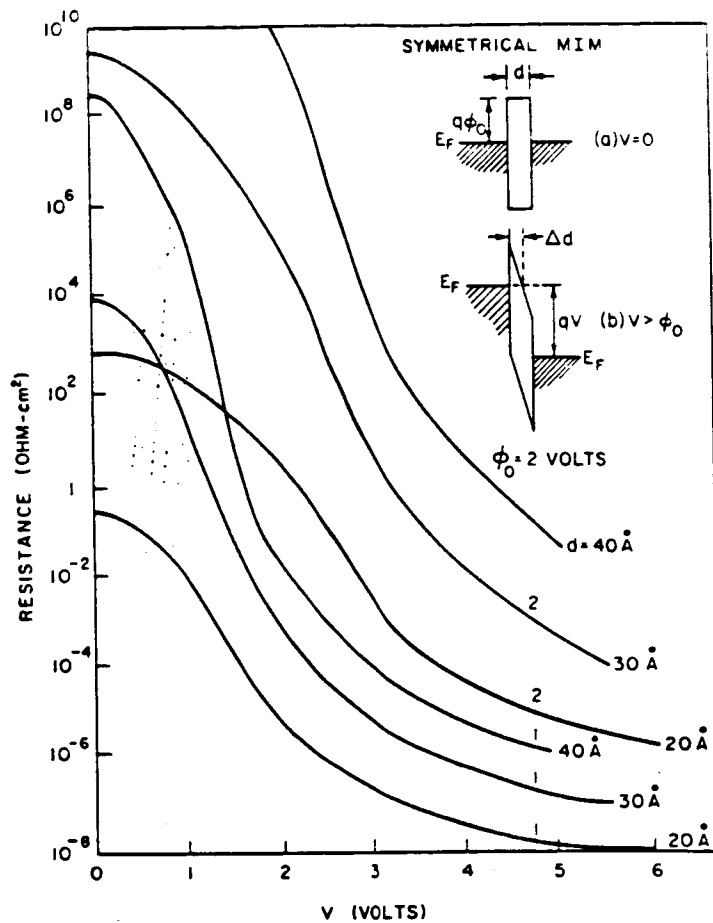
Figure 44. Tunnel resistance of a symmetrical MOM structure. The insert shows band diagrams at V = 0 (zero bias) and $V > \phi_0$. (After Simmons)
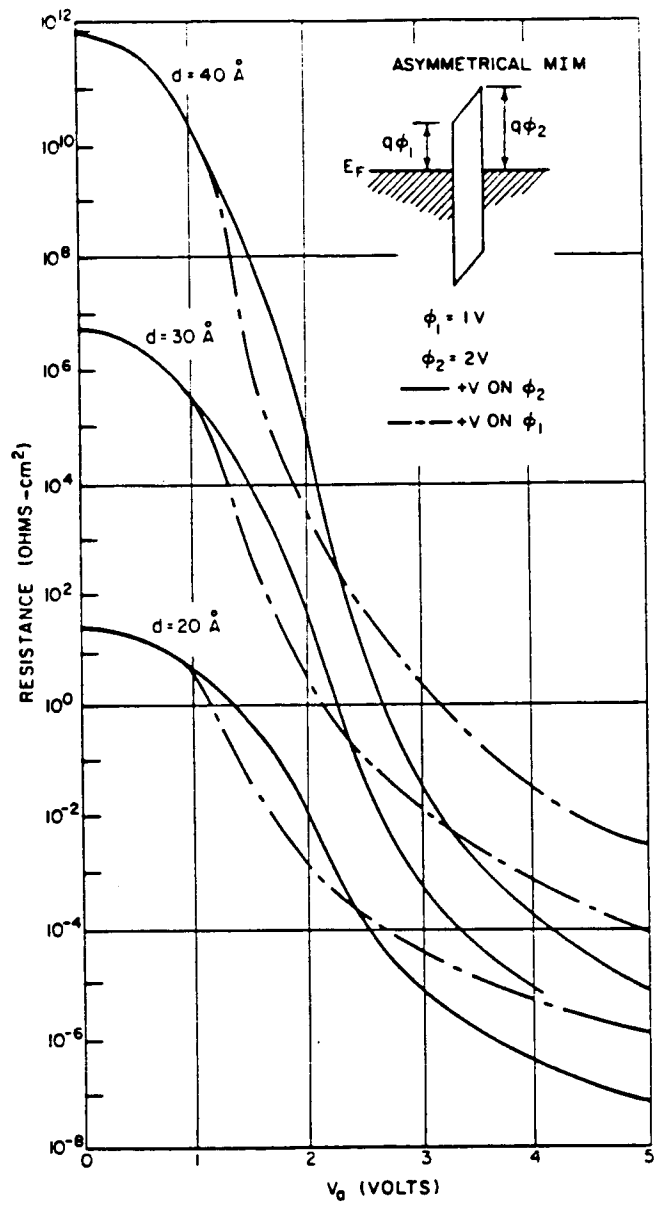
Figure 45.   Tunnel resistance as a function of applied voltage
for an asymmetrical MIM structure. The insert
shows the band diagram at zero bias. (After
Simmons.)

69

transferred from the antenna to the MOM structure. To first order, the power handling capabilities can be deduced by equating the power density in the MOM device to the power density received by the antenna. For a 10 $\overset{\bullet}{\text{A}}$ thick, 0.1 μm square MOM device, capable of handling 10^4 A/cm^2 at 1 volt, (Figure 43), the power load is estimated to be 10^{-6}W. The radiation power density emitted by the earth is approximately 200 W/m^2 at a distance of 100 miles above the earth's surface. For a T-type antenna whose collection area is approximately 0.1 λ^2, where λ is the wavelength of the incident wavelength radiation, the antenna collection area is = 8.8 x 10^{-11} cm^2 for 10.6 μm radiation and it will receive 1.8 x 10^{-8} W from the earth. This value is more than an order of magnitude below the power density that can be conducted through a 0.1 micron square MOM device and confirms that these devices are suitable for this application. In fact, the result suggests that some type of concentrator scheme could be used to focus radiation onto the rectenna elements to achieve higher power densities.

The last factor to consider is the rectification properties of these structures. These are determined by the I-V characteristics, a typical example of which for a MOM structure is shown in Figure 46. If V_1 and V_2 are the turning points in the I-V curves, then for practical applications it is required that the forward bias turning point, $V_1 \approx 0$ volt and the reverse bias turning point V_2, be significantly negative. If V_2 equals V_1, then rectification will occur for both current directions resulting in a cancellation of the dc output. As shown by Figure 45, the R-V curve calculated by Simmons for forward and reverse bias conditions implies that the magnitude of V_1 and V_2 are approximately equal, and thus this structure will not be an efficient rectifier. To obtain large V_2/V_1 ratios will therefore require very asymmetrical diode structures with the potential difference between the two metals exceeding several volts. Detailed calculations to estimate the characteristics of these structures and the effect of highly asymmetrical structures on the carrier transit times are therefore required to assess their
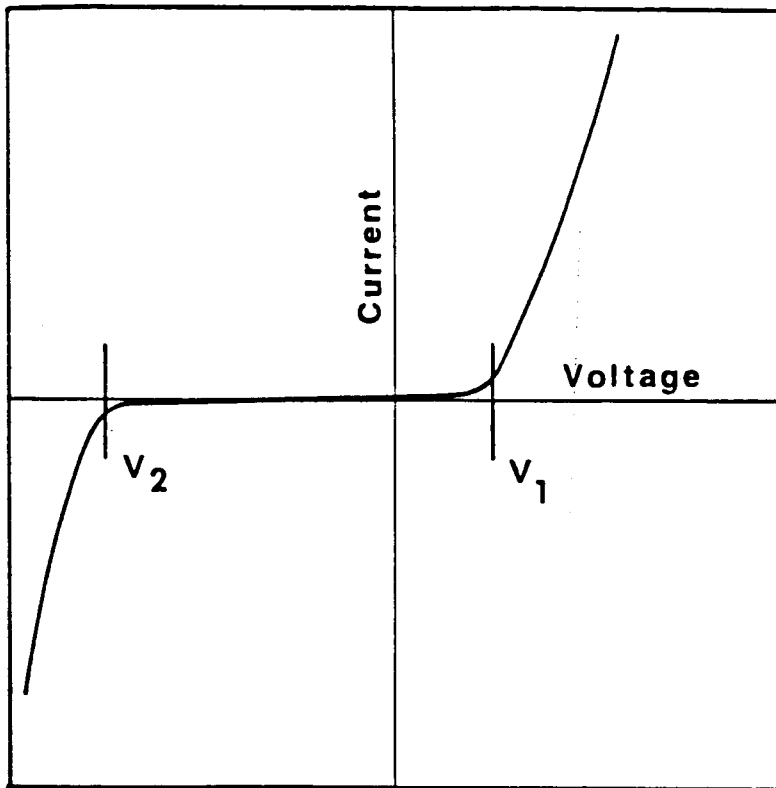
Figure 46 . Current-voltage relationship for MOM device.

full potential for this application.

In conclusion, the above discussion shows that the MOM device is the best candidate for the rectenna at infrared frequencies, but that further studies of these properties are required. Also, for this application, the devices must be very small; approximately 10 $\overset{\bullet}{A}$ thick and 0.1 μm square.

4.2 Fabrication Difficulties and Experimental Results

Historically, these devices have been very difficult to produce, but recently Heiblum, et al.[22] have developed a structure which is stable and reproducible. A schematic of this structure which was fabricated from Ni and its oxide is shown in Figure 47. As shown, the overlap between a 1 μm wide Ni layer and the oxidized edge of another Ni layer, 5 μm wide and 100 $\overset{\bullet}{A}$ thick, is used to make MOM structures with areas of 10^{-10} cm^{-1}. The thickness of the oxide film is approximately 10 $\overset{\bullet}{A}$ and the device has been tested and shown to have frequency independent I-V characteristics up to the near infrared region. However, despite the success achieved by Heiblum, we believe that this approach will be extremely difficult to apply to large arrays. For the fastest devices, the required insulator film thicknesses correspond to three or four atomic layers of oxide and thus a variation of one atomic layer will have a large effect on device performance. To achieve atomic layer precision in the growth of a non-crystalline devices constructed from dissimilar metals will require further efforts concentrated on such oxide growth. Thus, other techniques to produce the insulator region, such as Langmuir-Blogett layer, also warrant consideration. It is still possible, however, to use the MOM diodes at lower frequencies where the demand on the oxide layer is not as great, and will allow the test of concept to continue.

At millimeter wave frequencies, the contact area and oxide layer can be much larger than for the 10 μm wavelength case discussed above. We have fabricated nickel – nickel oxide – nickel and nickel-nickel oxide-bismuth diodes. The dimensions of the diodes are given in Figure 48 and a photograph of the device

SiO₂ OR Si SUBSTRATE

Ni ELECTRODE

DIODE # 2

Ni LAYER

2 μm

2000Å

500Å

5 μm

SiO₂

100Å

14 μm

1 μm

DIODE # 1

Ni ELECTRODE

1000Å

~10Å NiO
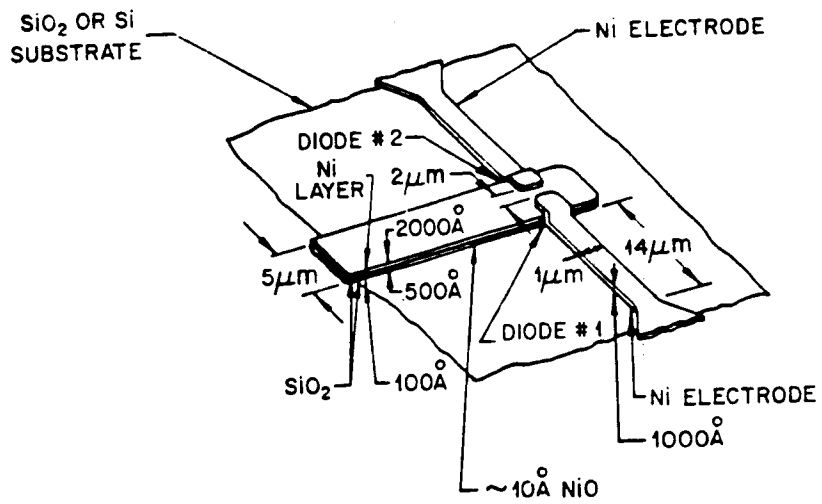
Figure 47.   Schematic diagram of Edge-MOM diode.
(After Heiblum et al.)
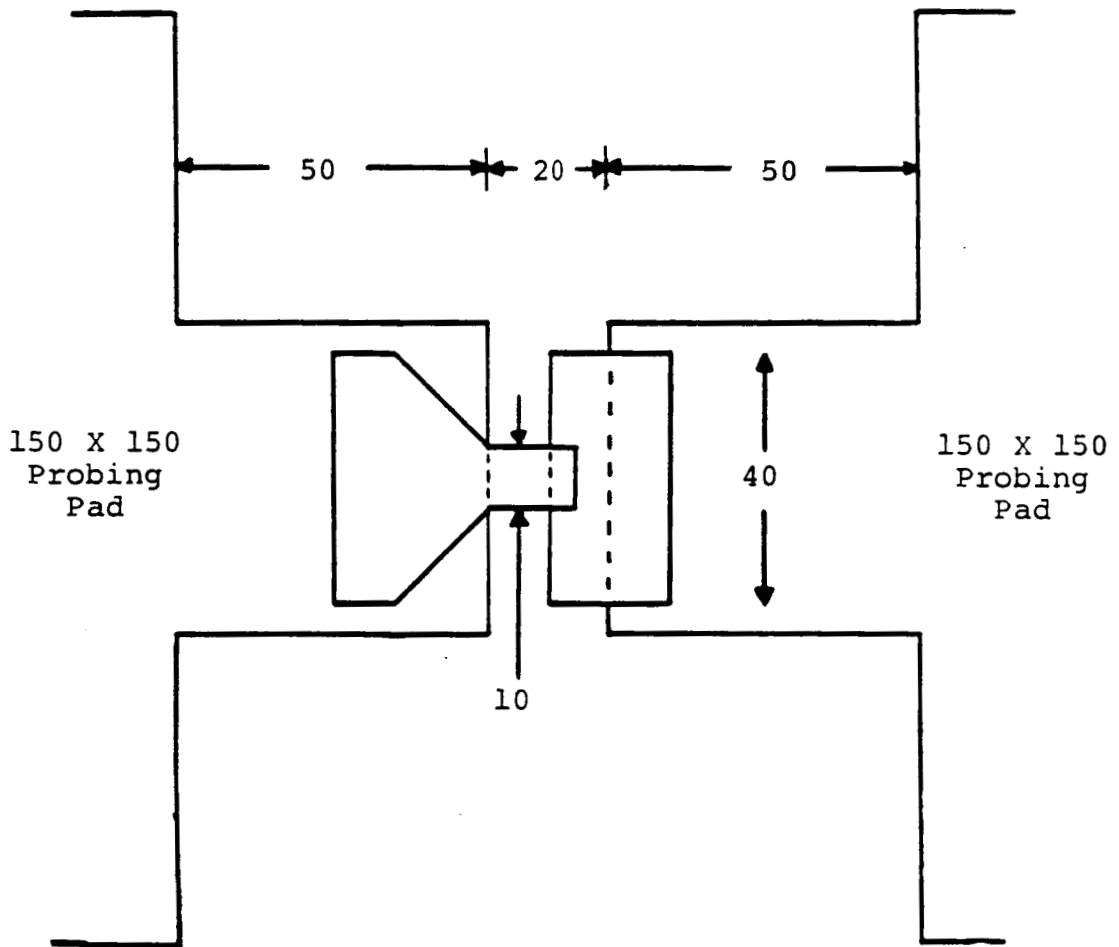
Figure 48. Three level MOM diode structure. All dimensions are in micrometers.

is shown in Figure 49. These devices were made by allowing the nickel to oxidize in atmosphere.

Typical I-V curves for the diodes are given in Figure 50. For the nickel - nickel oxide - bismuth diode curve, it is seen that there is little or no difference in the values of V_1 and V_2 as discussed earlier in this section (see Figure 46). This indicates that more work is needed on the MOM diodes if they are going to be used as efficient rectifying diodes.

5. CONCLUSIONS AND RECOMMENDATIONS

We have looked at the components that will be needed for high frequency rectenna devices. The majority of the effort has been spent on measuring the directivity and efficiency of the half-wave dipole antenna. It is felt that the antenna and diode should be roughly optimized before they are combined into a rectenna structure. An integrated low pass filter had to be added to the antenna structure in order to facilitate the field pattern measurements. We have also made a calculation of the power density of the earth's radiant energy as seen by satellites in earth orbit. Finally, we have assessed the feasibility of using a MOM diode for rectification of the received power.

Several conclusions can be made from this work. We have seen that stable, nonlinear MOM diodes can be made quite easily if the oxide layer is allowed to form in the atmosphere. The thickness of this oxide, however, is too great for these diodes to operate at 10 μm wavelengths. For the MOM diodes to operate at these frequencies, a technique to produce a uniform, reproducible oxide layer that is only 3 to 4 atoms thick over the entire wafer will have to be developed. Since this seems to be a difficult task, investigations on using some alternative insulating material, such as a Langmuir-Blogett layer,[23] should be considered. In addition, further theoretical work is needed to see if the MOM diode can be configured to give enough rectification efficiency to make the rectenna approach viable at the infrared frequencies.
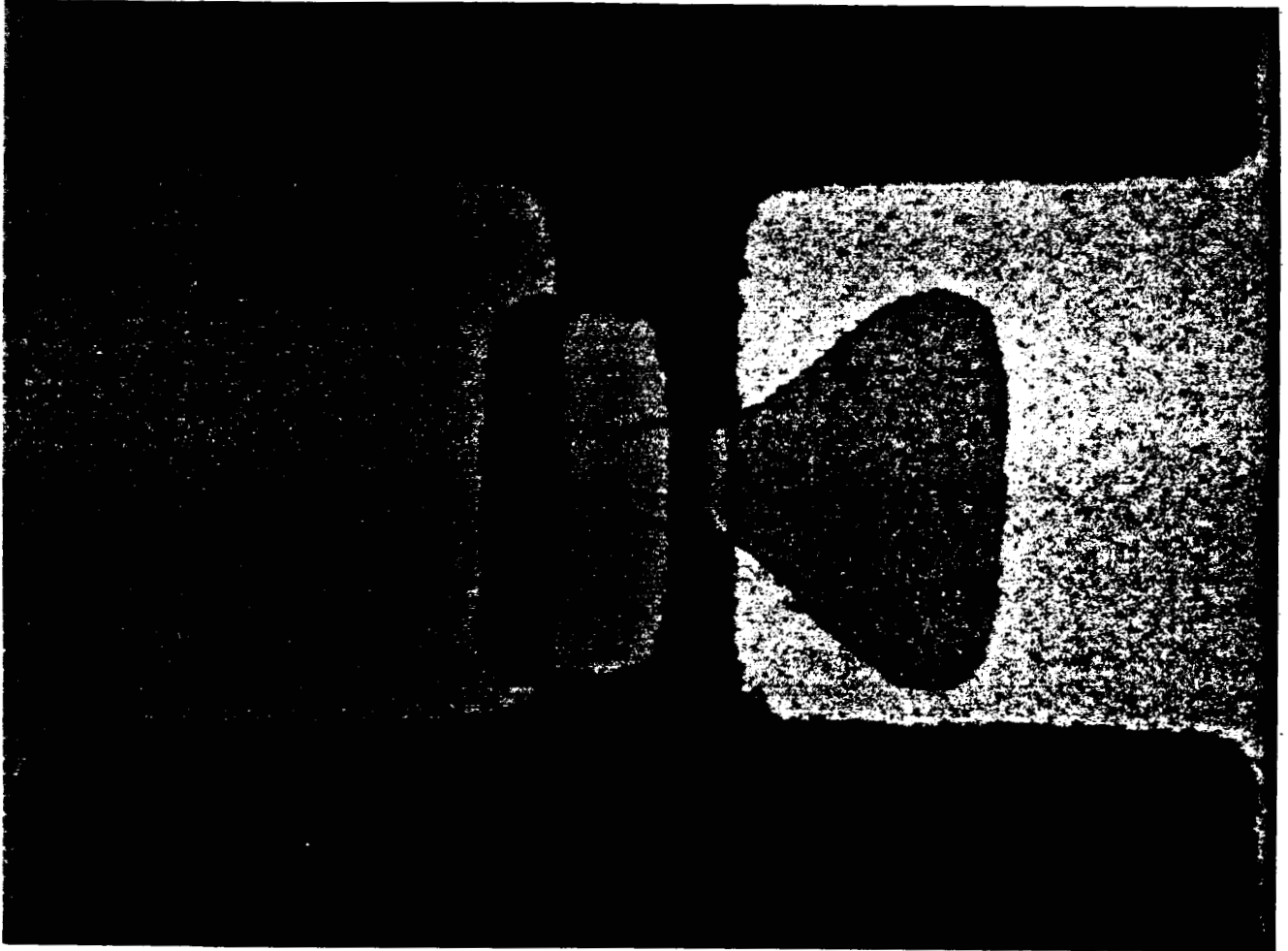
Figure 49. Close-up Photograph of three level MOM diode structure.
Dimensions for the diode are given in Figure 48.

a. Ni-NiO-Ni
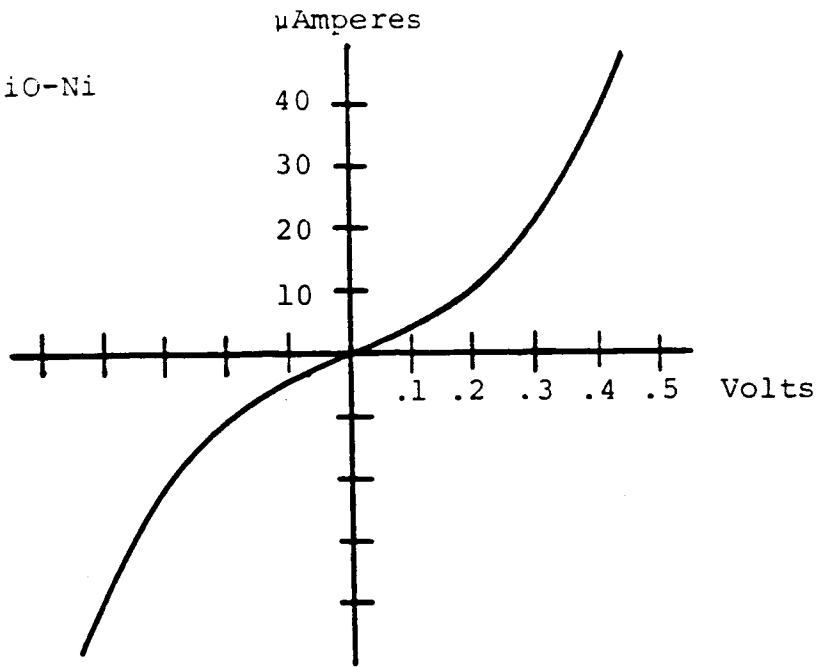
b. Ni-NiO-Bi
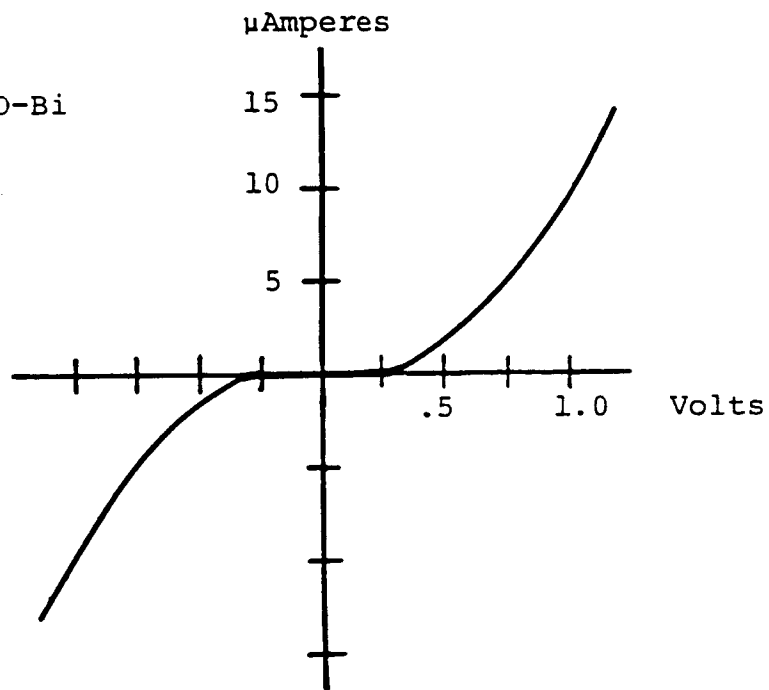
Figure 50. I-V curves for typical MOM diodes.

Investigating rectennas at millimeter wave frequencies is a more fundamental issue than producing a rectifying diode at 10 μm wavelengths. We believe this to be true for two reasons. First, the work at millimeter wave frequencies can serve as a proof of concept, scale model for higher frequency rectennas. Here, if the millimeter wave frequency is high enough, the issues of the collection efficiency of the substrate mounted antenna, the monolithic rectenna design, and the rectification efficiency of the diode will be addressed. Second, recent thoughts on using millimeter wave rectennas for narrow beam, point-to-point energy transfer present greater flexibility in the rectenna design and room for new innovations. If the operating frequency is in the millimeter wave region, more efficient semiconductor diodes can be used. Also, other antenna designs with collection efficiencies greater than the half-wave dipole may be possible. Any new developments in the millimeter wave rectennas could then be applied to the infrared rectennas.

One such semiconductor device takes advantage of the rapid advances occurring in the AlGaAs integrated circuits. A disadvantage of using these materials is that the higher refractive index of the substrate requires that the antenna geometries be smaller; however, other antenna structures besides the halfwave length dipole can be considered. This disadvantage is more than offset by the greater flexibility of the new semiconductor growth technologies, such as MBE and MOCVD, to grow very thin semiconductor and metal films. For example, MBE enables GaAs layers of one or two atomic layers thick to be deposited in a reproducible way. Also, ultra-thin crystalline Al films have been deposited on GaAs and, at present, work is directed toward obtaining the growth of thin crystalline GaAs layers on a crystalline Al surface. If this is successful it will become possible to grow a wide variety of devices.

It should be noted that this is already possible, to some extent, by the use of heavily doped n- and p-type GaAs layers which have metallic-like properties. Thus, one can envision fabricating the antenna and device arrays together in a series of

growth/processing procedures. A possible structure would consist of an antenna fabricated from heavily doped n+ GaAs (or Al), with the diode consisting of a thin layer of undoped GaAs sandwiched between the antenna arms at the base of the structure. This structure would be fabricated by first depositing a 1-2 μm thick layer of heavily doped GaAs onto a semi-insulating GaAs substrate, and then using photolithography and etching procedures to remove all of the GaAs layer apart from an array of individual elements shaped like one side of the antenna. The other side of the antenna would then be defined by a SiO_2 or Si_3N_4 mask, which is required to resist the high temperature experienced during the second growth step. This growth procedure would consist of the deposition of a thin 10-100 $\overset{\bullet}{A}$ epitaxial layer of undoped GaAs, followed by the deposition of a 1-2 μm thick layer of heavily doped n-type GaAs. Thus, the thin undoped GaAs layer would then be sandwiched between two heavily doped layers of GaAs, thereby forming a small area asymmetrically doped n++- n - n+ device. The I-V characteristics of this semiconductor-insulator-semiconductor device are similar to those of a MOM device and can be varied by changing the geometry of the device or by growing structures in series.

We recommend that, in addition to work on MOM diodes for 10 μm wavelength operation, work should continue at millimeter wave frequencies. We are maintaining a low level effort to study rectennas for operation below 100 GHz. The facilities in the Millimeter Wave Technology Division and Microelectronics Research Center at Georgia Tech are well suited for fabricating and testing devices in this frequency range. For the reasons listed above, further work on monolithic rectennas with semiconductor diodes will be useful for both point-to-point energy transfer and for aiding the development of rectennas to capture the earth's radiant energy.

REFERENCES

1. W. C. Brown, "Performance Characteristics of the Thin-Film, Etched-Circuit Rectenna," 1984 IEEE MTT-S Digest, pp. 365-367, 1984.

2. W. C. Brown, "Adapting Microwave Techniques to Help Solve Future Energy Problems," IEEE Trans., vol. MTT-21, pp. 753-763, 1973.

3. W. C. Brown, "The Technology and Application of Free-Space Power Transmission by a Microwave Beam," IEEE Proc., vol. 62, pp. 11-25, 1974.

4. W. C. Brown, "Solar Power Satellites: Microwaves Deliver the Power," IEEE Spectrum, pp. 36-42, June 1979.

5. W. L. Wolfe and G. J. Zissis, "The Infrared Handbook," ONR, 1978.

6. H. W. Yates, "Remote Sensing from Satellites," Chap. 26, in Remote Sensing of the Troposphere, ed. by V. E. Derr (Boulder: NOAA), 1972.

7. G. P. Boyankhchyan, V. A. Vanke and S. K. Lesota, "Problems in the Optimization of Parameters of a Schottky Barrier Diode in a Rectenna Element," Radio Engineering and Electronic Physics, English translation of Radiotekhnika-I Electronica, vol. 29, pp. 131-135, 1984.

8. S. Ashok, "Optimal Barrier Height for Schottky Diode Rectifiers," Int. J. Electronics, vol. 57, pp. 429-431, 1984.

9. C. Zah, et al., "Millimeter Wave Monolithic Schottky Diode Imaging Arrays," Int. J. of Infrared and MMW, vol. 6, pp. 981-997, 1985.

10. S. J. Nightingale, et al., "A 30 GHz Monolithic Single-Balanced Mixer Integrated Dipole Receiving Element," Microwave J., vol. 28, no. 8, pp. 103-116, 1985.

11. K. D. Stephan and T. Itoh, "A Planar Quasi-Optical Subharmonically Pumped Mixer Characterized by Isotropic Conversion Loss," IEEE Trans., vol. MTT-32, pp. 97-102, 1984.

12. C. M. Jackson and C. Sun, "Subharmonically and Fundamentally Pumped Slotline Quasioptical Mixer," IEEE MTT- International Microwave Symposium Digest, pp. 293-295, June 1986.

13. D. P. Neikirk and D. B. Rutledge, "Self-Heated Thermocouples for Far-Infrared Detection," Appl. Phys. Lett., vol. 41, no. 5, pp. 400-402, 1982.

14. D. P. Neikirk, W. W. Lann and D. B. Rutledge, "Far-Infrared Microbolometer Detectors," Int. J. of Infrared and MMW, vol. 5, pp. 245-278, 1984.

15. D. B. Rutledge and S. E. Schwarz, "Planar Multimode Detector Arrays for Infrared and Millimeter Wave Applications," IEEE Trans., vol. QE-17, pp. 407-414, 1981.

16. M. Kominami, D. M. Pozar and D. H. Schaubert, "Dipole and Slot Elements and Arrays on Semi-Infinite Substrates," IEEE Trans. Ant. and Prop.," vol. AP-33, pp. 600-607, June 1985.

17. G. D. Alley, "Interdigital Capacitors and Their Application to Lumped-Element Microwave Integrated Circuits," IEEE Trans. Microwave Theory and Tech., vol. MTT-19, pp. 1028-1033, December 1970.

18. S. M. Sze, Physics of Semiconductor Devices, (John Wiley & Sons, New York), p. 566, 1981.

19. D. B. Rutledge, S. E. Schwartz and A. T. Adams, "Infrared and Submillimeter Antennas," Infrared Physics, vol. 18, pp. 713-729, 1978.

20. M. Born and E. Wolf, Principles of Optics, (Pergamon Press, New York), pp. 60-61, 1956.

21. J. Simmons, J. Appl. Phys., 34, 2581, 1963.

22. M. Heiblum, S. Y. Wang, J. R. Whinnery and T. K. Gustafson, "Characteristics of Integrated MOM Junctions at DC and Optical Frequencies," IEEE J. Quantum Electron., vol. QE-14, p. 159, 1978.

23. G. G. Roberts, K. P. Pande and W. A. Barlow, "InP/Langmuir-film m.i.s.f.i.t.s," Sol. St. and Elec. Dev., vol. 2, pp. 169-175, 1978.

APPENDIX I

GEOMETRY FOR POWER RECEIVED AT SATELLITE FROM EARTH

For the case of low earth orbit satellites receiving earth radiation, the approximation that the earth is a flat disc emitter (which may be used for synchronous orbits or for solar radiation reception at earth satellites) does not hold for wide field of view, i.e. the case in which maximum earth radiation is collected. Since the earth is asumed to be a Lambertian emitter, the cosine function would omit radiation received from as far out as the horizon. It is, therefore, necessary to integrate over the earth surface observed within the satellite aperture FOV.

Consider Figure I-1 for the geometry of an elemental area dA_e of earth from which radiation can be received. Then,

$$dA_e = R_e d\phi \bullet R_e \sin \phi \, \gamma = 2 \, \pi R_e^2 \sin \phi d\phi$$

since the radiation will not be considered a function of γ. R_e is the earth's radius.

Figure I-2 shows the configuration for the satellite at a distance R_s from the center of the earth. $R_s = R_e + h$ where h is the satellite altitude. From Figure I-2,

$$R_{es}^2 = R_s^2 + R_e^2 - 2 \, R_e R_s \cos \phi$$

The solid angle from th earth is defined by the relations in Figure I-3.

$$d\Omega_{es} = \frac{dA_s \cos \theta_2}{R_{es}^2}$$
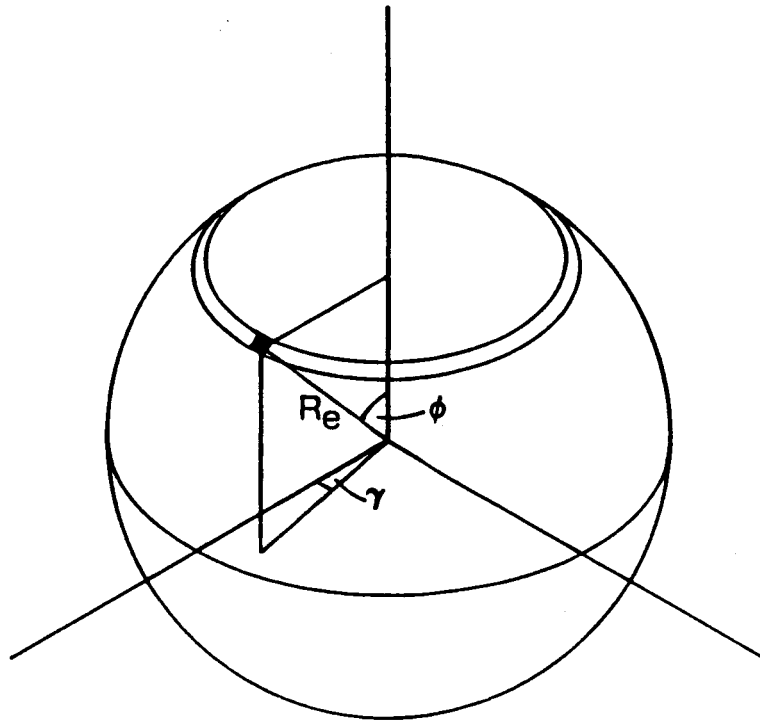
Figure I-1
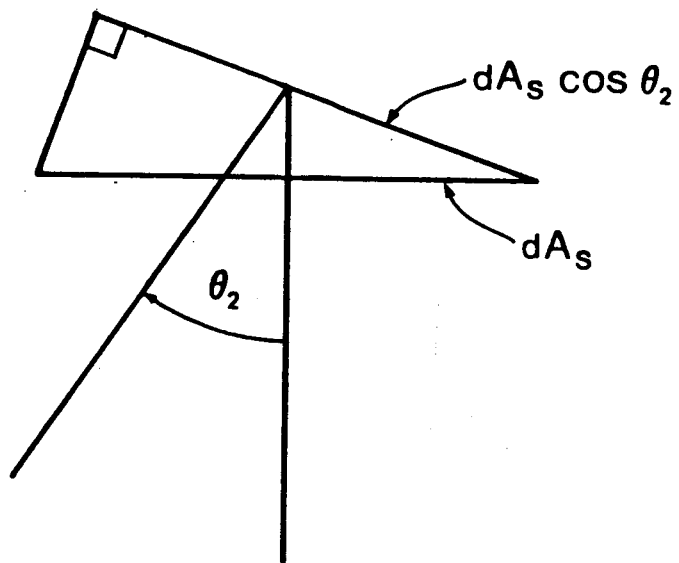
Figure I-3

Figure I-2

84
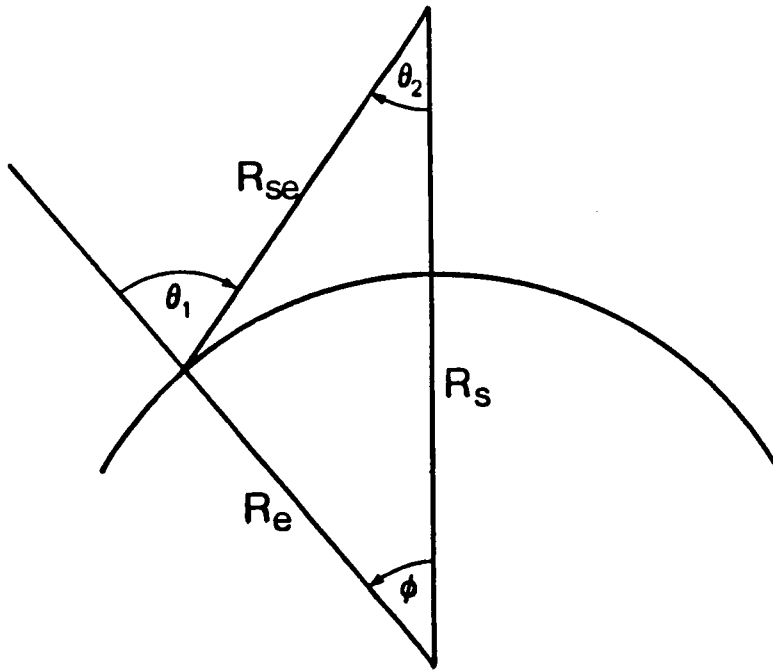
so

$$d\Omega_{es} = \frac{\cos \theta_2 \, dA_s}{R_s^2 + R_e^2 - 2 R_e R_s \cos \phi}$$

For a Lambertian source, the power at the satellite is given by

$$dP = B(\phi, \theta_1, \lambda) \cos \theta_1 \, (dA_e) \, (d\Omega_{es}) \, (d\lambda)$$

where $B(\phi, \theta, \lambda)$ is the spectral radiance in watts meter^{-2} ster^{-1} μm^{-1}.

$$dP = B(\phi, \theta_1, \lambda) \cos \theta_1 \, (2\pi R_e^2 \sin \phi \, d\phi) \bullet$$

$$\bullet \frac{(\cos \theta_2 \, dA_2) \, d\lambda}{R_s^2 + R_e^2 - 2 R_s R_e \cos \phi}$$

For the calculations, we assume $B(\phi, \theta, \lambda) = B(\lambda)$ and that the area of the satellite is a constant A_s, so that

$$P = A_s \int B(\lambda) d\lambda \int_0^{\phi_m} d\phi \left[\frac{2\pi R_e^2 \cos \theta_2 \cos \theta_1 \sin \phi}{R_s^2 + R_e^2 - 2R_s R_e \cos \phi} \right]$$

and $\theta_1 = \theta_2 + \phi$

We can set an upper bound on P by setting the integration independent of the angles θ_1 and θ_2 and consider the case of the satellite viewing to the horizon.

To obtain this limiting expression, we consider the

following

$$2\pi B_I A_s \int \frac{R_e^2 \sin \phi d\phi}{R_s^2 + R_e^2 - 2R_s R_e \cos \phi} \geq P \geq B_I A_s \cos \theta_{2m} \cos \theta_{1m} \bullet$$

$$\bullet \int \frac{2\pi R_e^2 \sin \phi d\phi}{R_s^2 + R_e^2 - 2R_s R_e \cos \phi}$$

so that

$$P \leq \frac{2\pi R_e}{2R_s} \int \frac{2R_s R_e \sin \phi d\phi}{R_s^2 + R_e^2 - 2R_s R_e \cos \phi} \bullet B_I A_s$$

but

$$\int_0^{\phi_{max}} \frac{b \sin \phi d\phi}{a - b \cos \phi} = \int \frac{du}{u} = \ln u \Big|_{u(o)}^{u(\phi_m)}$$

$$a = R_s^2 + R_e^2, \quad b = 2R_s R_e$$

$$u = a - b \cos \phi$$

$$du = b \sin \phi d\phi$$

87

So

$$P \leq \frac{2\pi B_I A_s R_e}{2 R_s} \left[\ln \frac{R_s + R_e - 2R_s R_e \cos\phi_m}{R_s + R_e - 2R_s R_e} \right]$$

For a satellite in a 200 mile orbit,

$R_s = 4167$ miles

$R_e = 3967$ miles

$\phi_m \approx 17.8°$ (to horizon)

so $P \leq 11.975 \, B_I A_s$

$B_I \approx 61.71$ W/m^2 for $\lambda = 6\text{-}16$ μm for 288°K Blackbody

$P \leq 683$ Watts for a square meter

This is considerably greater than the satellite will receive, since the limiting expression is equivalent to setting $\cos \theta_{2m}$ and $\cos \theta_{1m}$ equal to 1, which does not occur physically. In addition, the use of the 288°K blackbody does not account for the reduction of outward radiation by the atmosphere. The rectennas will probably not be operative over the entire band from 6-16 μm.

To integrate the rxpression for P, we can utilize the angular relations given in Figure I-4.

$$\theta_1 = \theta_2 + \phi$$

$$\cos(\theta_1 - \theta_2) = \cos\phi$$

$$= \cos \theta_1 \cos \theta_2 + \sin \theta_1 \sin \theta_2$$

88
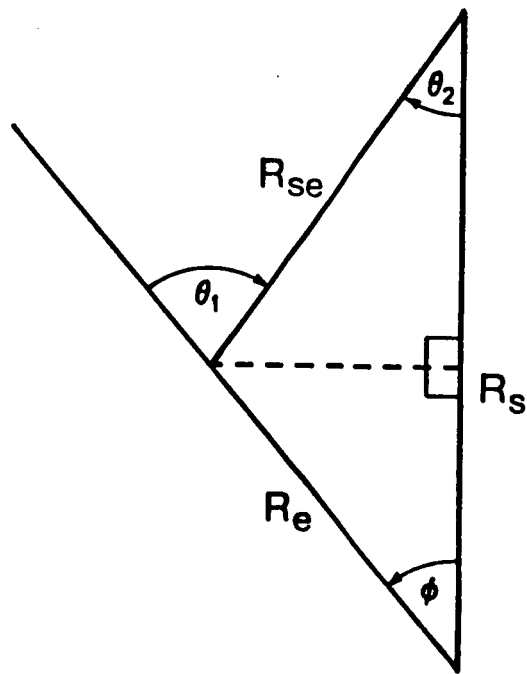
Figure I-4

and
$$R_e \sin\phi = R_{se} \sin\phi_2$$

where

$$R_{se} = (R_s^2 + R_e^2 - 2R_s R_e \cos\phi)^{\frac{1}{2}} \quad \text{so} \quad \cos\theta_1 = \cos\theta_2 \cos\phi - \sin\theta_2 \sin\phi$$

$$= \cos\phi \left(1 - \left(\frac{R_e \sin\phi}{R_{se}}\right)^2\right)^{\frac{1}{2}} - \frac{\sin\phi \, R_e \sin\phi}{R_{se}}$$

$$= \cos\phi \left[1 - \frac{R_e^2 \sin^2\phi}{R_s^2 + R_e^2 - 2R_s R_e \cos\phi}\right]^{\frac{1}{2}} - \frac{\sin^2\phi \, R_e}{\left[R_s^2 + R_e^2 - 2R_s R_e \cos\phi\right]^{1/2}}$$

and

$$\cos\theta_2 = \left(1 - \frac{R_e^2 \sin^2\phi}{R_s^2 + R_e^2 - 2R_s R_e \cos\phi}\right)^{\frac{1}{2}}$$

Thus, the full expression for the power is

$$P = B_I A_s \, 2\pi R_e^2 \int_0^{\phi_m} \left\{ \left[\cos\phi \left(1 - \frac{R_e^2 \sin^2\phi}{R_s^2 + R_e^2 - 2R_s R_e \cos\phi}\right)^{1/2} \right. \right.$$

$$\left. \left. - \frac{R_e \sin^2\phi}{(R_s^2 + R_e^2 - 2R_s R_e \cos\phi)^{\frac{1}{2}}} \right] \right\} \left[\frac{\left(1 - \frac{R_e^2 \sin^2\phi}{R_s^2 + R_e^2 - 2R_s R_e \cos\phi}\right)^{\frac{1}{2}}}{R_s^2 + R_e^2 - 2R_s R_e \cos\phi} \right] \sin\phi \, d\phi$$

90

Integration will result in a geometrical factor applicable at any position of the satellite relative to earth. The radiance will vary as a function of season, latitude, etc. The power density observable at the satellite is then given by

$$\frac{P}{A_S} = B_I \; 2 \; R_e^2 \pi \int_0^{\phi_m} (\ldots\ldots) d\phi$$

where the earth's radius is

$$R_e = 3967 \text{ miles}$$

and

$$2\pi R_e^2 - 9.8892 \times 10^7 (\text{miles})^2$$

For the calculation of received power, we'll consider the expression for power density to be B_I times a power collection factor. The integral in this factor is calculated for values of height (in miles) and angle ϕ_m to the horizon. The field of view angle θ is $\pi/2 - \phi$. The total power density is then

$$\frac{P}{A} = B_I \; F(h,\phi)$$

with $F(h,\phi)$, the power collection factor.

$$\int_0^{\phi_m} \left\{ \left[\cos\phi \left(1 - \frac{a^2 \sin^2 \phi}{b - c \cos\phi} \right)^{1/2} \right] - \frac{a \sin^2 \phi}{(b - c \cos\phi)^{1/2}} \right\} \quad X$$

$$\left[\frac{\left(1 - \frac{a^2 \sin^2\phi}{b - c \cos \phi} \right)^{1/2}}{b - c \cos\phi} \right] \sin\phi \; d\phi$$

$$a = Re = 3967; \quad b = R_s^2 + 1.5737 \times 10^7; \quad c = 2R_s R_e = 7.934 \times 10^3 R_s$$

C -2-   91

R_s	Height	ϕ_m(horizon)	Other ϕ_m			b	c
			1	2	3		
			$10°$	$5°$			
4167	200	$17.8°$	10°	5°		3.31009×10^7	3.306098×10^7
4267	300	21.6	15	10	5	3.3944289×10^7	3.385438×10^7
4534	567	29	20	12	8	3.6294156×10^7	3.5972756×10^7
4589	622	30.2	20	15	10	3.6795921×10^7	3.6409126×10^7
4899	932	35.9	25	20	10	3.9737201×10^7	3.8868666×10^7
5467	1500	43.5	30	20	10	4.5625089×10^7	4.3375178×10^7
5967	2000	48.3	35	25	15	5.1342089×10^7	4.7342178×10^7
26962	22996	81.5	50	30	20	7.4274036×10^8	2.1392444×10^8

APPENDIX II
Radiation Relations

The spectral distribution of the earth's radiation can be estimated from Planck's law for spectral radiant emittance (W cm^{-2} μm^{-1})

$$W_\lambda = \frac{2\pi hc^2}{\lambda 5} \frac{1}{e^{ch/\lambda kt} - 1}$$

written as

$$W = \frac{c_1}{\lambda 5} \frac{1}{e^{c_2/\lambda t} - 1}$$

where

λ = wavelength, μm

h = 6.6256 x 10^{-34} W(sec)^2

T = absolute temperature

c = 2.997925 x 10^{10} cm/sec

c_1 = 2 hc^2 = 3.7415 x 10^4 W cm^{-2} μm^4

c_2 = ch/k = 1.43879 x 10^4 μm $^\circ K$

k = 1.38054 x 10^{-23} Wsec$(^\circ K)^{-1}$

The peak of the blackbody, given by Wien's displacement law, occurs at λ_m

$$\lambda_m T = 2897.8 \ \mu m \ ^\circ K$$

$$\lambda_m = 1.35 \ \mu m \ \text{for} \ T = 280 \ ^\circ K$$

The spectral radiance is given by $L_\lambda = W\pi^{-1}$ (in W/m^2 μm^{-1} sr^{-1}). The following tabulation applies for T - 280 $^\circ K$.

$\lambda(\mu m)$	$W_\lambda (W/m^2 \mu m^{-1})$	$L_\lambda (W/m^2 \mu m^{-1} sr^{-1})$
6.0	9.183	2.930
6.5	11.895	3.786
7.0	14.447	4.597
7.5	16.743	5.329
8.0	18.567	5.910
8.5	20.023	6.334
9.0	21.071	6.707
9.5	21.741	6.920
10.0	22.331	7.108
10.5	22.132	.7.044
11.0	21.948	6.986
11.5	21.578	6.869
12.0	21.061	6.704
12.5	20.434	6.505
13.0	19.729	6.280
13.5	18.970	6.038
14.0	18.179	5.787
14.5	17.373	5.530
15.0	16.565	5.273
15.5	15.765	5.018
16.0	14.981	4.769

The integrated radiance $B_I = \Sigma L \Delta \lambda$ from 6-16 μm is approximately 61.18 watts/m^{2}st^{-1} and from 8-13 μm is approximately 36.68 watts/m^{2}sr^{-1}.

The spectral radiance estimated from Figures 3 through 10 in the main text is presented in the following table. Each figure represents a different seasonal state and latitude over North America.

Spectral Radiance (W/m^2 sr^{-1} μm^{-1})

Wavelength $\lambda(\mu m)$	Figure 3	Figure 4	Figure 5	Figure 6	Figure 7	Figure 8	Figure 9	Figure 10
6.00	2.20	1.00	0.70	0.70	1.72	1.90	1.50	1.15
6.25	2.75	1.10	0.75	0.80	2.00	2.10	1.75	1.30
6.50	3.75	1.50	1.05	1.00	3.50	3.90	2.40	2.00
6.75	2.75	1.50	1.25	1.10	3.35	2.50	2.10	1.55
7.00	4.15	1.97	1.50	1.30	4.00	4.30	3.00	2.35
7.25	4.65	2.10	1.60	1.40	4.30	4.80	3.40	2.75
7.50	4.80	2.05	1.70	1.35	4.50	6.30	3.55	3.05
7.75	4.00	2.20	1.40	0.90	5.10	5.50	3.90	3.10
8.00	5.00	2.90	1.80	1.75	5.60	7.30	5.20	3.75
8.25	7.70	3.50	2.35	2.10	8.25	9.60	6.90	4.90
8.50	8.10	3.70	2.70	2.60	9.30	10.15	7.20	5.40
8.75	8.40	4.00	2.90	2.80	9.50	10.50	7.35	5.55
9.00	8.65	4.20	3.15	3.00	10.00	10.70	7.50	5.90
9.25	8.70	4.30	3.25	3.05	9.60	10.00	7.60	6.00
9.50	6.70	3.00	2.10	2.10	5.60	6.00	5.60	4.20
9.75	4.45	3.10	2.40	2.20	5.00	6.50	4.60	4.20
10.00	7.00	4.20	2.80	2.50	5.10	9.50	6.50	4.90
10.25	8.50	4.30	3.10	3.00	8.50	10.30	7.70	5.50
10.50	8.55	4.40	3.50	3.45	9.50	10.20	7.85	6.25
10.75	8.50	4.50	3.60	3.50	9.50	10.00	7.80	6.20
11.00	8.40	4.60	3.65	3.60	9.30	9.80	7.60	6.15

95

Wavelength λ(μm)	Figure 3	Figure 4	Figure 5	Figure 6	Figure 7	Figure 8	Figure 9	Figure 10
11.25	8.30	4.60	3.65	3.60	9.00	9.50	7.55	6.10
11.50	8.15	4.60	3.65	3.60	8.90	9.35	7.50	6.05
11.75	8.00	4.55	3.65	3.60	8.75	9.15	7.40	6.03
12.00	7.90	4.50	3.65	3.60	8.60	8.95	7.20	6.00
12.25	7.70	4.40	3.60	3.50	8.20	8.50	7.00	5.80
12.50	7.40	4.35	3.57	3.45	7.80	8.00	6.60	5.40
12.75	7.05	4.30	3.53	3.40	7.50	7.80	6.50	5.25
13.00	6.80	4.25	3.50	3.35	7.10	7.55	6.00	4.95
13.25	6.00	3.90	3.25	3.00	6.00	6.50	5.00	4.10
13.50	5.40	3.25	2.50	2.60	4.00	4.70	4.00	3.50
13.75	3.95	2.85	2.30	2.30	3.70	4.30	3.80	3.30
14.00	3.15	2.50	2.20	1.85	3.25	3.40	3.20	3.05
14.25	2.10	2.20	2.00	1.70	2.95	3.00	2.80	3.00
14.50	2.05	2.25	2.15	1.90	2.40	2.35	2.75	3.20
14.75	2.40	2.50	2.25	2.05	2.55	2.70	3.00	3.25
15.00	2.50	2.60	2.80	2.10	2.95	2.75	3.45	3.30
15.25	2.40	2.50	2.15	2.05	2.50	2.50	2.95	3.10
15.50	2.30	2.25	1.90	2.00	2.50	2.50	2.85	3.00
15.75	1.80	2.00	1.90	1.90	2.00	2.20	2.55	2.75
16.00	2.05	2.10	1.90	1.70	2.40	2.40	2.50	2.65
B_I(8-13μm) (W/m²sr⁻¹)	37.99	21.56	17.44	15.94	42.65	47.23	36.29	28.62
B_I(6-16μm)	54.38	32.66	25.84	24.36	58.07	64.88	51.40	42.48

96

APPENDIX III

"Measurement Techniques for Millimeter Wave Substrate Mounted Antennas," presented at the Conference on Millimeter Wave/ Microwave Measurements and Standards for Miniaturized Systems, 6- 7 November 1986, Huntsville, Alabama.

Measurement Techniques for Millimeter Wave
Substrate Mounted MMW Antennas

November 7, 1986

M. A. Gouker, D. P. Campbell and J. J. Gallagher
Georgia Tech Research Institute
Georgia Institute of Technology
Atlanta, Georgia 30332

Abstract

An overview of measurement techniques for millimeter wave substrate
mounted antennas is presented. Scattering and pickup of the millimeter
wave radiation on the low frequency leads is a significant problem in these
measurements. Methods to reduce these effects are discussed, and
preliminary work on dipole antennas at 230 GHz is presented.

A substrate mounted antenna is a radiating or receiving structure
where the metal lies on only one side of a dielectric substrate. At
millimeter wave frequencies, these antennas are fabricated with integrated
circuit techniques. A dominant property of the substrate mounted antennas
is that they receive incoming radiation much better through the dielectric
substrate than directly from free space. This property can be used to
perform useful tasks, such as focusing, with the substrate. A
comprehensive review of the properties and experimental work (up to 1982)
with these antennas is given by Rutledge, et al.[1]

I. Measurement Technique

A table top range with appropriately placed absorber is used to

1. D.B. Rutledge, D.P. Neikirk and D.P. Kasilingam, "Integrated Circuit
   Antennas," Infrared and Millimeter Waves, vol. 10, pp. 1-90, Academic
   Press, 1983.

measure the antenna patterns at millimeter wave frequencies. The basic measurement scheme consists of a millimeter wave source with power meter and standard gain horn, a chopper to modulate the radiation, an antenna positioner, and an antenna with an integrated detector. Quasi optical components can be used to collimate the beam or adjust the polarization.

Three types of integrated detectors are used: these are Schottky barrier diodes, thermocouples and bolometers. Beam lead diodes bonded into the circuit and monolithic diodes fabricated with the antenna are known. The diode can be operated as a square law detector or with a local oscillator for heterodyne detection[2-5]. The local oscillator can be fed to the mixer diode via transmission lines on the substrate[3] or quasi optically by irradiating the antenna with both the RF and the LO[4,5]. A bismuth-antimony thermocouple has been reported[6]. This detector has the advantage of bias-free operation. The third detector type is the micro bolometer[7]. Typically, bismuth is used because of its high resistivity.

The thermocouple and bolometer function by thermal heating from the induced millimeter wave frequency currents in the antenna. It is possible to calibrate the responsivity and NEP of these detectors electronically[6-8]. A known RF signal, usually in the MHz range, is placed across the antenna to simulate the millimeter wave operation. From this, the responsivity and NEP are measured.

2. C. Zah, et al., "Millimeter Wave Monolithic Schottky Diode Imaging Arrays," Int. J. of Infrared and MMW, vol. 6, pp. 981-997, 1985.
3. S.J. Nightingale, et al., "A 30 GHz Monolithic Single-Balanced Mixer Integrated Dipole Receiving Element,"Microwave J., vol. 28, no. 8, pp. 103-116, 1985.
4. K.D. Stephan and T. Itoh, "A Planar Quasi-Optical Subharmonically Pumped Mixer Characterized by Isotropic Conversion Loss," IEEE Trans., vol. MTT-32, pp. 97-102, 1984.
5. C.M. Jackson and C. Sun, "Subharmonically and Fundamentally Pumped Slotline Quasioptical Mixer," IEEE MTT- International Microwave Symposium Digest, June 1986, pp. 293-295.
6. D.P. Neikirk and D.B. Rutledge, "Self-Heated Thermocouples for Far-Infrared Detection," Appl. Phys. Lett., vol. 41, no. 5, pp. 400-402, 1982.
7. D.P. Neikirk, W.W. Lann and D.B. Rutledge, "Far-Infrared Microbolometer Detectors," Int. J. of Infrared and MMW, vol. 5, pp. 245-278, 1984.
8. D.B. Rutledge and S.E. Schwarz, "Planar Multimode Detector Arrays for Infrared and Millimeter Wave Applications," IEEE Trans., vol. QE-17, pp. 407-414, 1981.

II. Low Frequency Leads

Scattering from and pickup on the low frequency leads are significant problems in antenna measurements. These leads bring the detected signal from the antenna to the external bias circuit and lock-in amplifier. The scattering is especially difficult with two-dimensional arrays, since the low frequency leads must pass close to other antenna elements. There are two ways to approach these problems: one is to use leads that have inherently reduced pickup and scattering, and the other is to integrate a low pass filter into the antenna structure.

Several techniques have been reported using the first approach. One uses low frequency leads much larger than the receiving element. For example, the bow tie antenna, first reported by Rutledge and Maha[9], is similar to two pencils placed tip to tip. This structure radiates only from the triangular sections provided the bow tie portion is larger than two dielectric wavelengths of the operating frequency[10]. The low frequency leads extend from the broad end of the bow tie to the edge of the substrate. No mention of the scattering from this type of low frequency lead is given. Another technique to minimize the adverse effects of the detector circuitry connections uses high resistance leads. It has been shown that leads with resistance in the megohm per meter range reduce pickup and scattering and behave like a distributed low pass filter[11].

Fabricating a discrete low pass filter with the antenna is another method to reduce pickup on the low frequency leads. In this method, the low pass filter shorts the currents induced in the leads before they flow to the detector while still allowing the low frequency detector signal to pass. This approach, however, does not address the scattering problem.

9. D.B. Rutledge and M.S. Muha, "Imagine Antenna Arrays," IEEE Trans., vol. AP-30,, pp. 535-540, 1982.
10. D.B. Rutledge, D.P. Neikirk and D.P. Kasilingam, "Integrated Circuit Antennas," Infrared and Millimeter Waves, vol. 10, pp. 1-90, Academic Press, pp. 26, 1983.
11. G.S. Smith, "Analysis of Miniature Electric Field Probes with Resistive Transmission Lines," IEEE Trans., vol. MTT-29, pp 1213-1224, 1981.

In our work at 230 GHz, a low pass filter incorporating a horseshoe shaped bolometer is used. As pictured in Figure 1, the current induced in the low frequency leads is shorted through the interdigitated capacitor disallowing flow through the bolometer. The current induced in the antenna flows through two parallel bolometers. One current path lies directly between the arms of the dipole, and the other includes the shorting capacitor. The resistance of the bolometer sections is set so that the parallel combination is equal to the radiation resistance of the antenna. This configuration simplifes fabrication because when only a single bolometer is placed between the antenna arms, blocking resistors are needed to prevent the flow of antenna current through the capacitor.

Preliminary results on a 3 x 3 array of dipoles shows that scattering from the low frequency leads severely distorts the antenna pattern of the individual elements. In this array, 0.7 mil gold bonding wire is used to connect the detector circuitry to the antenna structure. The bonding wires are kept a minimum of 10 wavelengths from the other antenna elements.

To measure the degree of scattering from and pick-up on the low frequency leads, it is necessary to measure a known antenna pattern. Figures 2 and 3 show antenna patterns of the dipole rotated parallel (θ = 0,180) and perpendicular (θ = 90,270) to the E field polarization in a plane perpendicular to the propagation direction. The well known theoretical result for this measurement is shown in Figure 3. The effect of scattering from the bonding wires is seen in Figure 2. The pattern shown in Figure 3 is measured by shielding all but the element under test with absorber. Note that θ = 0 and θ = 180 are both parallel alignment of the dipole and E field and should therefore have identical reception even with scattering. The nonsymmetric distortion here is most likely due to pickup on the low frequency leads. This indicates that the capacitor value needs to be larger. A revised antenna structure is currently being investigated.

III. Conclusions

Measurements on millimeter wave substrate mounted antennas can be performed on a table top range. The basic setup consists of a millimeter
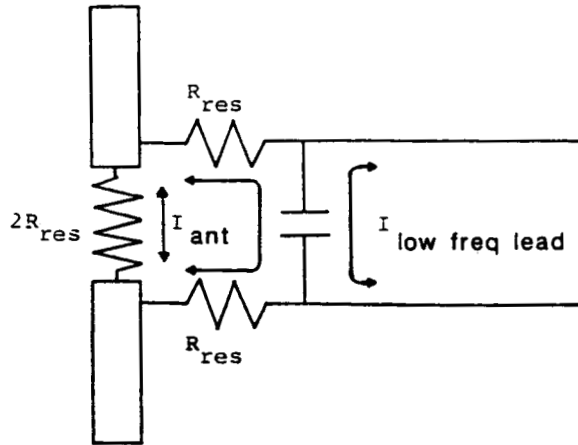
Figure 1. Schematic drawing of the horseshoe bolometer.
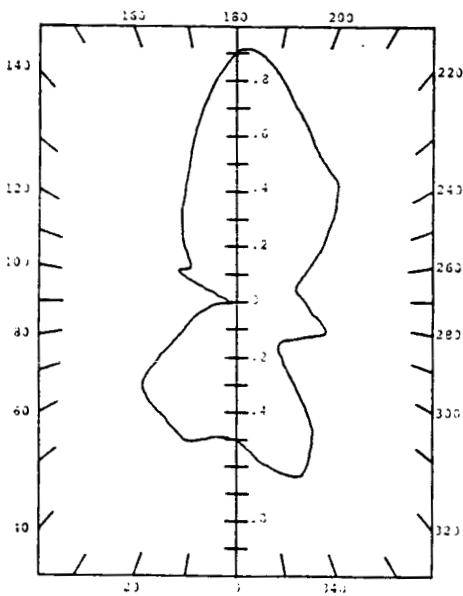

Fig. 2. The effect of scattering from adjacent low frequency leads on an array element.
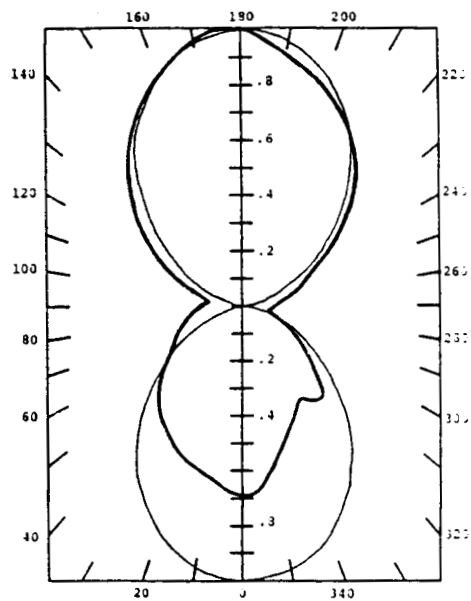
Fig. 3. Antenna pattern of a single isolated antenna. The thin line is the theoretical curve for this measurement.

wave source, chopper, antenna positioner and antenna with an integrated detector. Scattering and pickup from low frequency leads are significant problems in two-dimensional arrays. Two methods used to address these problems are 1) leads which have inherently reduced pickup and scattering and 2) integrating a low pass filter in the antenna structure. Of these, only the high resistance leads are effective against both pickup and scattering.